FORECASTING EXCESSIVE RAINFALL AND LOW-CLOUD BASES EAST OF THE NORTHERN ANDES AND MESOSCALE CONVECTIVE COMPLEX MOVEMENT IN CENTRAL SOUTH AMERICA

THESIS

Marc R. Gasbarro, Captain, USAF

AFIT/GM/ENP/03-03

DEPARTMENT OF THE AIR FORCE
AIR UNIVERSITY

AIR FORCE INSTITUTE OF TECHNOLOGY

Wright-Patterson Air Force Base, Ohio

AFIT/GM/ENP/03-03

FORECASTING EXCESSIVE RAINFALL AND LOW-CLOUD BASES EAST OF THE NORTHERN ANDES AND MESOSCALE CONVECTIVE COMPLEX MOVEMENT IN CENTRAL SOUTH AMERICA

THESIS

Presented to the Faculty

Department of Engineering Physics

Graduate School of Engineering and Management

Air Force Institute of Technology

Air University

Air Education and Training Command

In Partial Fulfillment of the Requirements for the

Degree of Master of Science in Meteorology

Marc R. Gasbarro, B.S.

Captain, USAF

March 2003

AFIT/GM/ENP/03-03

FORECASTING EXCESSIVE RAINFALL AND LOW-CLOUD BASES EAST OF THE NORTHERN ANDES AND MESOSCALE CONVECTIVE COMPLEX MOVEMENT IN CENTRAL SOUTH AMERICA

Marc R. Gasbarro, B.S.

Captain, USAF

Approved:

Lt Col Ronald P. Lowther (Chairperson)	18 Feb 03 Date
Lt Col Michael K. Walters (Member)	20 Feb 03 Date
Maj Robin N. Benton (Member)	19 Feb 03 Date

Preface

"Nothing in life is accomplished without passion."

- *Anonymous*

I would like to thank many people who made this thesis work possible. First, I would like to thank my thesis advisor, Lt Col Ron Lowther, for his advice and mentorship during this process. Second, I express my gratitude to all other members in my committee, Lt Col Michael Walters and Maj Robin Benton, for their terrific aid and expertise they provided. I am also indebted to Mr. Michel Davison of the International Desks section of NCEP, the DOC4 and DOC5 teams of AFCCC, the folks in the AFCCC technical library, Mr. Stephen Corfidi of the Storm Prediction Center, and my research sponsors, especially Maj Jonathan Kelly and MSgt Thomas Zipprich, from the SOUTHCOM weather cell at the 25th OWS at Davis-Monthan AFB, AZ. I would also like to extend my thanks to the circulation desk personnel at AFIT's library for their extensive aid in providing the resources and assistance necessary to conduct this research. I also praise my classmates for yielding precious time from their theses in providing technical assistance. On a more personal note, I praise my family and son for the inspiration. Finally, I'm most grateful for former AFIT Associate Dean, Col. Wayne Hallgren, for his invaluable personal guidance.

Last, and certainly not least, I thank my wonderful companion and girlfriend. After all these years, you are the only one who truly stands by me unconditionally. Words can't express my appreciation toward the continual sacrifices you make.

Marc R. Gasbarro

Table of Contents

List of Figures

List of Tables

Abstract

This research produces better forecast tools for SOUTHCOM's 25th Operational Weather Squadron (OWS) over multiple areas of operation in South America. Heavy rainfall and low-cloud base events along the northeastern Andes foothills are examined, as well as, mesoscale convective complexes (MCCs) in Central South America (CSA). Low clouds, fog, and flooding rains hamper daily Department of Defense (DoD) counter-drug operations in Northwestern South America (NWSA). In addition, fierce MCCs interfere with joint-military exercises in CSA.

Climatological relationships of heavy rain with low clouds and fog in NWSA, relationships of excessive rainfall with upper-level divergence, low-level convergence, and vertical velocity in NWSA, and verification of Corfidi's method (Corfidi et al. 1996) of MCC movement for CSA are investigated. Ceilings and visibilities associated with low clouds and fog lower much more frequently following heavy rainfall in NWSA. In addition, findings prove that specific ceiling heights and visibilities relate to certain precipitation intensities. Findings indicate certain synoptic and meso-alpha scale features and specific minimum thresholds of upper-level divergence, low-level convergence, and vertical velocities are shown necessary to produce excessive rainfall events. Finally, Corfidi's method of forecasting MCC movement for North America is verified for applicability over CSA. Both propagation and advective cloud component vectors are examined for forecast use.

FORECASTING EXCESSIVE RAINFALL AND LOW-CLOUD BASES EAST OF THE NORTHERN ANDES AND MESOSCALE CONVECTIVE COMPLEX MOVEMENT IN CENTRAL SOUTH AMERICA

I. Introduction

One of the greatest challenges in today's high-operations tempo Air Force is the challenge to forecast anywhere around the globe regardless of forecaster experience. One area of responsibility (AOR) for forecasters is the AOR for Southern Command (SOUTHCOM), which includes all of the Americas south of Mexico. The most volatile region of SOUTHCOM is Northwest South America (NWSA), where the military performs counter-drug and humanitarian aid operations. The military also participates in joint exercises in various parts of the AOR to include Central South America (CSA). Forecasting for such operations in data-sparse regions with limited weather knowledge can be difficult.

The Air Force Weather Agency (AFWA) and the 25th Operational Weather Squadron (OWS) at Davis-Monthan Air Force Base (AFB), Arizona (weather forecast center for the AOR) seek forecasting knowledge of these critical, data-sparse regions. Heavy precipitation events and low-cloud bases hamper both Air Force and Army operations along the eastern foothills of the northern Andes and adjacent highlands from 7˚ N to 7˚ S. In addition, powerful mesoscale convective complexes (MCCs) traversing Northern Argentina, Paraguay, Uruguay, and Southern Brazil disrupt important joint-military exercises in these regions. The goal of this research is three-fold: to develop

forecasting tools for fog and low-cloud base events in the Columbian Highlands and Western Amazon Basin, to develop forecasting guidance to predict excessive rainfall in the Columbian Highlands and Western Amazon Basin, and to predict MCC movement in CSA. Figures 1 and 2 display topographical and geographical/political locations referred to throughout this research.

Fig. 1. Topography and associated geographical features of South America.

Fig. 2. Political map of South America (modified from *Maps.com*, 2002).

1.1. Excessive Rainfall, Fog, and Low-Cloud Bases over Columbia, Ecuador, and Northern Peru east of the Andes.

1.1.1. Statement of the Problem. Excessive rainfalls (24 hour rainfall of 6" or more) commonly disrupt military operations in NWSA. Intense tropical squall lines, trade wind surges, and monsoon surges associated with the passage and oscillation of the near equatorial trough (NET), in concert with tropical air masses, orographic lift, and diurnal changes can create enormous amounts of precipitation in a short period of time over the region. Heavy rainfall events adversely affect electro-optical and infrared sensors for surveillance and weapon deployment operations, inhibit aircraft recovery processes, and interfere with communications. Such events can also flood runways and cause the military to switch its focus from military operations to humanitarian relief operations. A 4-6" 24-hour rainfall can create significant flooding and landslides in the region (Zipprich 2002). Unfortunately, numerous military locations lie within 150 nm of the windward (eastward) side of the Cordillera Oriental (Eastern Andes range), where orographic uplift further enhances unsettled weather systems.

In addition to heavy rain, low-cloud bases and fog can unfavorably affect military operational flights. Intense rainfall and radiational cooling create widespread low-cloud bases and fog events. Mission requirements in Columbia, Ecuador, and Northern Peru generally necessitate the need for low-flying aircraft and helicopters for surveillance and rescue operations. Fog or low clouds lowering to below aircraft landing minimum requirements over runways may force aircraft to land at unfavorable locations. In addition, surveillance flights usually require a cloud-free line-of-sight to the ground. Therefore, if clouds restrict viewing, operators are forced to lower their flight levels or

cancel missions. Very low flight levels could even prove hazardous in high-risk areas, especially if the level is within reach of weapon fire from unfriendly forces.

1.1.2. Research Objectives. The 25th OWS requires forecasting guidelines for accurate prediction of low-clouds, fog, and heavy rainfall events in NWSA. The goal of this particular topic is two-fold: to develop climatological tables from surface observations for fog and low cloud base events in the Columbian Highlands and Western Amazon Basin, and to develop forecasting guidance from surface observations and model reanalysis data to predict excessive rainfall in the Columbian Highlands and Western Amazon Basin. Due to data restrictions, the period of record (POR) only encompasses 1995-2002 for the fog and low cloud studies and 1995-1996 for the excessive rainfall study. All studies within this topic utilize extensive literature reviews, climatological studies, data analysis, and archived surface observations to achieve specific objectives. Although general seasonal characteristics are present with heavy rainfall and low clouds, this study focuses on daily (rather than seasonal) forecasting techniques. In addition, this study focuses on meso-alpha cloud scale and synoptic scale events.

Specific objectives necessary to achieve the fog and low-cloud studies are:

1. Gather and examine surface observations for NWSA east of the Andes from the Air Force Climatology Combat Center (AFCCC 1995-2001) and 25th OWS (2001-2002) for the POR 1995-2002;
2. Pick out observations with reports of 1" or more of 24-hour accumulated precipitation provided the observation site has a valid 12 UTC observation on the following morning;

3. Determine the probability of occurrence of falling below certain airfield minimum categories (3000/3; 1500/3; 1000/2; 300/1; 200/0.5) from surface observations;
4. Separate all precipitation observations by intensity (drizzle, light rain, moderate rain, and heavy rain);
5. Determine the probability of occurrence of falling below certain airfield minimum categories (using the same categories as objective 3) given that a certain precipitation intensity occurs;
6. Determine a range of ceilings and visibilities based on probabilities given a certain precipitation intensity occurs;
7. Incorporate all forecast guidelines into a forecast predictive tool.

The specific objectives necessary to achieve the excessive rainfall study are:

1. Gather and examine all surface observation data from AFCCC (1995-2001) for the POR 1995-1996;
2. Segregate all observations reporting 24-hour accumulated precipitation of 1-2" and 6" or greater;
3. Gather and analyze archived satellite imagery from the National Climatic Data Center (NCDC 2002) and National Geophysical Data Center (NGDC 2002), as well as, raw Global Data Assimilation System (GDAS) reanalysis data from the National Center for Atmospheric Research (NCAR 1995-1996);
4. Collect raw reanalysis data from the National Center for Atmospheric Research (NCAR 1995-1996) and interpolate the raw data onto a 45 km Mercator projection grid;

5. Analyze divergence values, vertical velocity values, and wind vector charts from the reanalysis data;
6. Compare upper-level divergence, low-level convergence, and vertical velocities of 1-2" events to 6" or greater rainfall events;
7. Create forecasting guidelines to include a summary of synoptic and meso-scale excessive rainfall precursors and generic divergence and vertical velocity thresholds for excessive rainfall events.

1.2. Forecasting Mesoscale Convective Complex Movement in Northern Argentina, Southern Brazil, Paraguay, and Uruguay.

1.2.1. Statement of the Problem. MCCs in CSA interfere with pertinent military exercises and disrupt military operations. Numerous meteorological ingredients work in concert to produce mammoth MCCs that yield extensive areas of heavy rainfall and low-cloud bases primarily at night. The military requires extensive lead-time with MCC forecasts to properly re-locate or postpone exercise missions. Failing to foresee MCC development or failing to forecast its movement with enough lead-time could cost the service lost training and resources, as well as, aborted missions.

1.2.2. Research Objectives. The 25th OWS requires forecasting guidelines to forecast MCCs in CSA. An extensive background review on MCCs and the differences between South American and North American MCCs are provided to aid in predicting the formation of MCCs one to two days in advance. However, the main objective of this research topic is to predict MCC and large mesoscale convective system (MCS) movement. This research exploits Corfidi et al.'s (1996) technique of MCC movement for North America (NA) MCCs and applies and verifies the technique to movement of

South America (SA) MCCs. Twenty-two cases (20 MCCs and 2 MCSs) from Jan 2001 and Sep - Dec 2002 are examined in full detail for MCC and MCS movement.

The specific objectives necessary to achieve this study are:

1. Gather and analyze archived satellite imagery from the Cooperative Institute for Research in the Atmosphere (CIRA 2002) and National Aeronautical and Space Administration (NASA 2002) to determine evolution, intensity, movement, and decay of MCCs and MCSs for the 22 case studies;
2. Gather and analyze upper-level reanalysis charts from the Fleet Numerical Meteorological and Oceanography Detachment (FNMOD 2001-2002);
3. Exploit Corfidi et al.'s (1996) NA method of tracking the movement of MCCs and MCSs to the 22 SA MCC and MCS cases by examining relationships between forecasted and observed speeds, as well as, directions of MCCs and MCSs;
4. Compare the findings to Corfidi's NA results;
5. Summarize the found forecasting technique guidelines into an appendix.

II. Literature Review and Background Information

2.1. Excessive Rainfall, Fog, and Low-Cloud Bases over Columbia, Ecuador, and Northern Peru east of the Andes.

2.1.1. Synoptic-Scale and Meso-Alpha Scale Features. Numerous larger scale features drive the tropical climate in NWSA. Perhaps the most important feature is the continental interaction with the inter-tropical convergence zone (ITCZ). The region of the ITCZ in NWSA is commonly referred to as the near equatorial trough (NET) or monsoon trough (Gilford et al. 1992; Walters et al. 1989). The *Glossary of Meteorology* (GOM) (2000) defines an equatorial trough as a "quasi-continuous belt of low pressure lying between the subtropical high pressure belts" of both hemispheres. The GOM (2000) defines a monsoon trough as a location of "relatively minimum sea level pressure in a monsoon region," which includes the NWSA since it experiences a seasonal shift in wind direction. Countless authors refer to the trough as the NET while the Air Force Technical Notes use both terms. While both terms are correct, this research uses NET.

The NET oscillates meridionally throughout the year. Figs. 3a-3d show the mean position of the NET broken in several locations due to land-ocean differential heating. It moves south during the austral summer (Fig. 3a), then migrates northward to the Columbian Highlands, an area east of the Andes ranging from 700 to 2000 ft in elevation, from Jun – Nov (Figs. 3c and d). The migration is closely linked to the seasonal movement of the solar declination. The NET fragments into multiple troughs over land chiefly due to terrain differences (the Andes and Venezuelan Highlands) breaking up the trades. Climatologically, most convection occurs 600 nautical miles (nm) north and 300

nm south of the NET placement. Stronger convection occasionally occurs as the NET surges north and south for the season. After NET passage, boundary level winds change direction as the trade winds flow from a different hemisphere (Gilford et al. 1992).

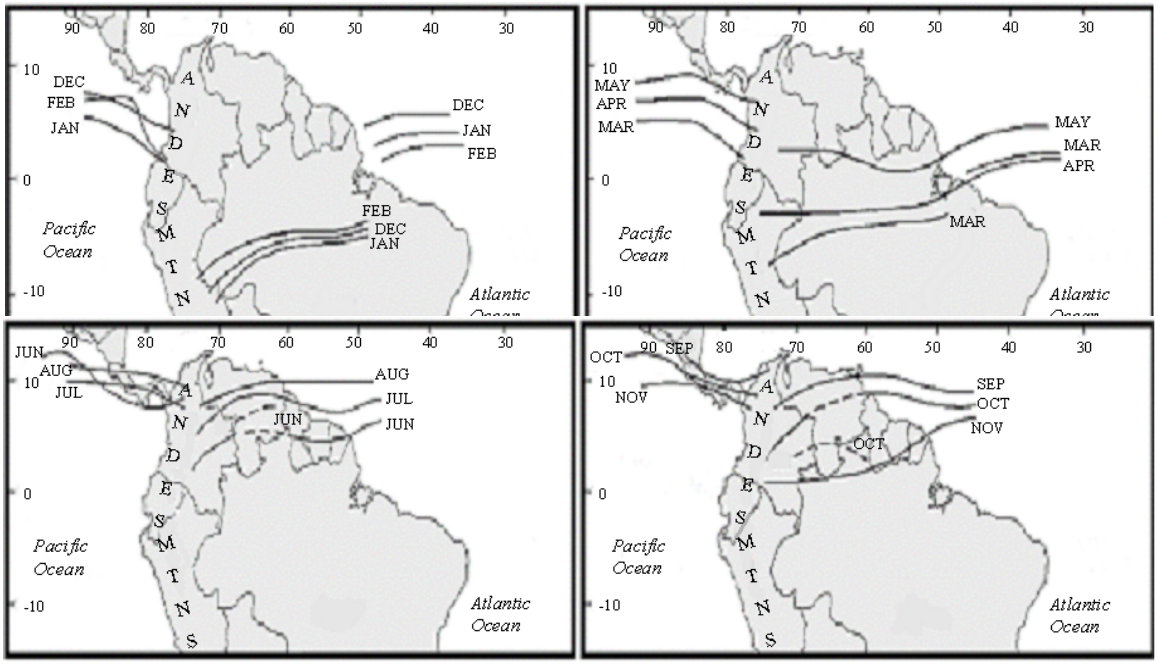

Fig. 3. Climatological NET placement (modified from Walters et al. 1989).

When exceptionally strong trades develop, intense squall lines form enhancing convection along the NET. Gamache and Houze (1982) define tropical squall lines as discrete propagating mesoscale disturbances. Gamache et al. (1994) adds that squall lines are "discontinuous lines or arcs of discrete clusters of cells." Fig. 4 shows a typical cross section of a squall line. Dryer mid-tropospheric flow entrains the squalls causing downdrafts and convergence with the trades. The outflow from the leading squall line element (LE) converges with surface trades triggering more storms ahead of the main LE. The older LE then decays coalescing with the trailing anvil sector. Constant regeneration along with translation with respect to easterly flow results in the squall line's westward progress (Gamache and Houze 1982; Gilford et al. 1992).

Gamache and Houze (1982) and Gilford (1992) discuss divergence and vertical velocity fields. The strongest convergence typically occurs from 900 to 700 mb. Divergence from 500 to 300 mb over the leading squall elements enhances upward motion while convergence at the same levels in the anvil sector enhances downward motion preventing development from eastward moving outflow converging with low-level easterly trades (Fig. 4). The divergence-convergence couplets produce areas of maximum upward and downward vertical velocities adjacent to each other (Gamache

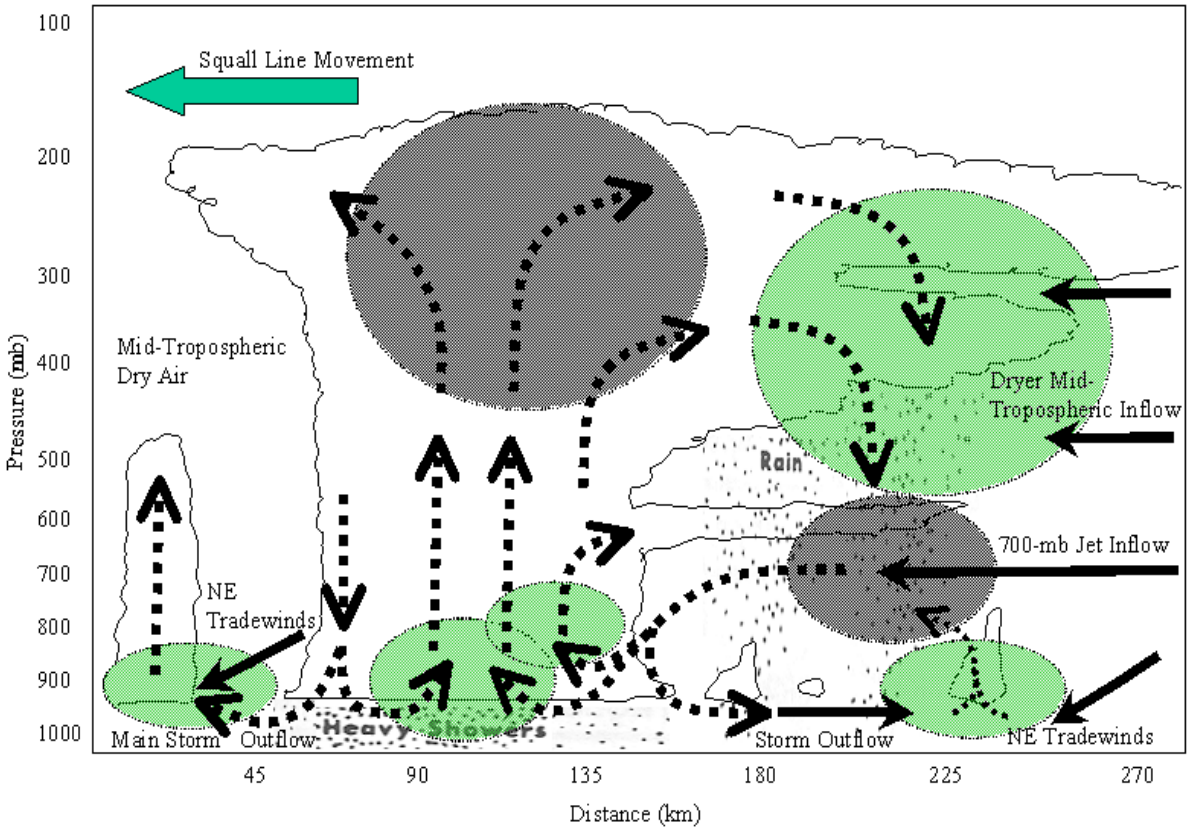

Fig. 4. Vertical cross section of a tropical squall line. Dashed lines denote updrafts and downdrafts while solid lines denote horizontal flow. Lighter circles are areas of convergence and darker circles are areas of divergence.

and Houze 1982). Upward vertical velocities in the leading element can exceed 20 – 30 cm s^{-1} while downward vertical velocities in the anvil sector approach 10 cm s^{-1}. In addition, surface to 700 mb convergence tilts eastward with height towards the direction of the 700 mb jet inflow.

Ramage (1995) theorized the possibility of nocturnal land breezes off the coast of Guyana, Suriname, French Guiana, and extreme Northeastern Brazil (from 8º N to 5º S) converging with easterly trades. However, the strongest squalls form from daytime sea breeze circulation convergence along the same coastline (Garstang et al. 1994). Garstang et al. (1994) discussed the stages for an Amazon tropical squall line. Onshore sea breeze winds converging with predominant southerly or southwesterly trades cause coastal genesis of the squalls. The strongest squalls form along and south of the NET and in areas of concave coastline structures such as just north and south of the Amazon River Delta. South of the NET, southeasterly trades cross the equator and turn southwesterly due to Coriolis changes. As the trades increase, surface convergence increases creating greater potential for stronger squall lines (Cohen et al. 1995). With enough initial convergence, the squalls regenerate line elements (20-40 km wide) within their own structure (as described previously) forming new LEs. Daytime heating also enhances convection. Eventually, the MCSs mature with a 100-500 km wide anvil section forming from decaying leading LEs. Numerous heavy rainfall events result from tropical squall lines. Cells then diminish with loss of daytime heating as they propagate through the Central Amazon Basin. Cluster size diminishes, clouds edges become more ragged, cloud tops warm, and LE width decreases. In addition, less vertical momentum transfer leads to less convergence ahead of the LE and, therefore, less discrete movement. Given

enough low-level convergence, cells may regenerate in the Western Amazon Basin with the following day's solar heating but dissipate again with nightfall (Garstang et al. 1994).

Figs. 5a-b show the distinct difference between two stages of squall line development along the coasts of Suriname, French Guiana, and extreme Northeastern Brazil. The recently formed squall line propagates inland (Fig. 5a) then intensifies six hours later (Fig. 5b). Trailing LEs are embedded in the developing anvil behind the leading LE with the trailing anvil increasing as the system materializes. Also, the squall line intensifies at night. Although squall line intensity typically follows the diurnal differences in sensible heating, local topography (highlands in Suriname and French Guiana), and synoptic scale changes also affect its intensity. Figs. 6a-f illustrate the changes in a squall line life cycle. Notice the discontinuous nature and longevity of the squall lines (Figs 6a-6f).

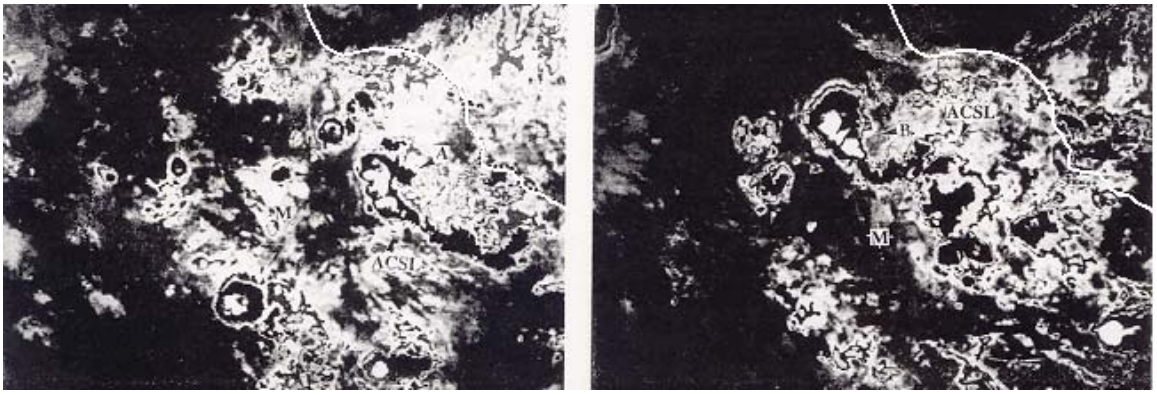

a. 0330 UTC 26 Apr 87 b. 1000 UTC 26 Apr 87

Fig. 5. IR satellite imagery of a developing Amazon coastal squall line (ACSL) for 26 Apr 87. Coldest tops are repeat white (< -81° C). Letters are non-applicable (modified from Garstang et al. 1994).

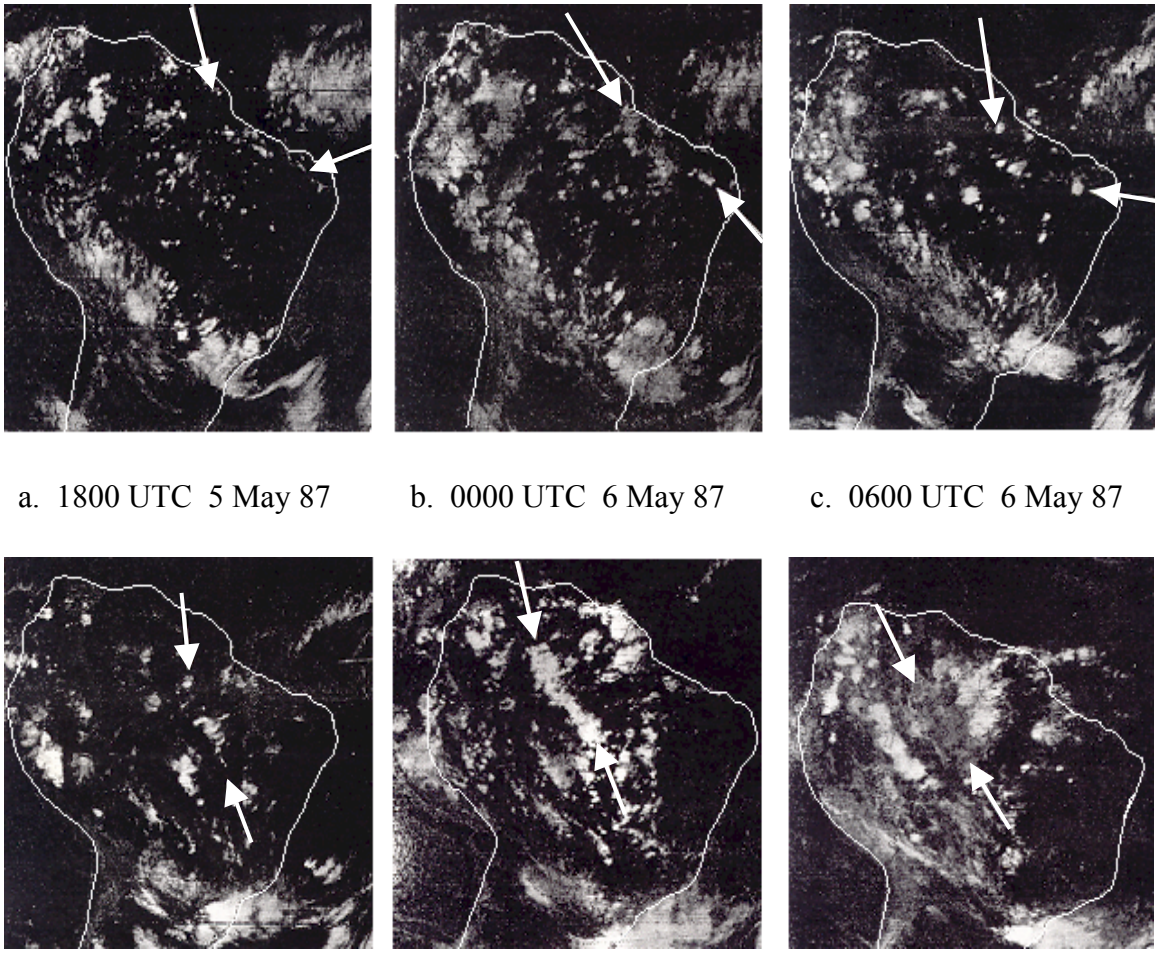

a. 1800 UTC 5 May 87 b. 0000 UTC 6 May 87 c. 0600 UTC 6 May 87

Fig. 6. IR satellite imagery of tropical squall lines for 5 to 7 May 87 (modified from Cohen et al. 1995). Arrows point to a specific squall line that was tracked across the continent. Notice the subtle differences with respect to sensible heating.

Gamache and Houze (1982), Garstang et al. (1994), Gilford et al. (1992), and Houze (1977) summarized the important characteristics of tropical squall lines over SA in Table 1.

Table 1. Characteristics of tropical squall lines.

- Entire squall line moves west at nearly 25-30 knots
- Squalls typically progress 10º of longitude per day
- More intense squall lines propagate faster than slower ones
- Highest tops reach over 50,000 ft
- Entire squall line lengths average 500-1500 statute miles (sm) long and 100-200 sm wide (although only about half of length contains active convection)
- Leading LE produces cloud bases and visibilities around 500 ft and ¼ sm
- Stratified anvil sector produces bases above 1000 ft and 2-4 sm visibilities
- Surface temperature drops 3º to 6º C for several hours following initial LE
- Absolute humidity decreases 2-3 g/kg for several hours following initial LE
- Relative humidity increases 5-15 % for several hours following initial LE
- Pressure decreases 1-2 mb for several hours following initial LE followed by a 1 mb increase
- Gusty outflow surface winds can reach or exceed 25 kts
- Surface wind shift common
- Leading LE lies along westward boundary of coldest infrared (IR) cloud tops
- IR cloud top temperatures usually $\leq$ -47º C
- Rainfall rates in leading LE average 110 mm/hr (~ 4.33”/hr) but can exceed 200 mm/hr (~ 8”/hr)
- Rainfall length varies from 2 to 8 hours depending on width, strength, and speed of entire system
- Radar reflectivity $\geq$ 38 dBZ in leading LEs but 28-38 dBZ in trailing anvil
- LE last 2-3 hours before decaying possibly yielding to newer LEs
- Organized squall lines usually last 24-48 hours
- Anvils produce 40-50 % of total squall line rainfall

Forecasting squall line occurrences can be a challenge in the data-sparse tropical regions. Previously mentioned, sea breeze convergences initiate convection; however, there are various other factors that distinguish a strong 48-hour lasting squall line from

one that forms for a few hours with the sea breezes then dissipates. Cohen et al. (1995) discuss the atmospheric dynamics necessary to sustain these systems.

The largest factor is mass convergence from mid-level winds. Cohen et al. (1995) found that intense squall lines develop from a maximum zonal easterly wind or low-level jet (LLJ) between 800–700 mb of at least 30 kts while weaker squall lines may develop from a LLJ of 15-20 knots. Intense squall lines usually hold together and re-intensify over the interior with the following day's diurnal heating. Marginal events (easterlies 20-25 kts) produce coastal squall lines; however, the line usually dissipates before traveling far inland. Easterlies less than 20 kts seldom have lasting effects on squall line development. Another factor is the wind direction of the easterly LLJ. Intense squalls will not form if the easterlies parallel the coast. Winds must cross the land at an angle to converge with the predominant southwesterly trades (Cohen et al. 1995).

Figs. 7a-c illustrate classical examples for squall line formation. Easterlies strengthen and become more onshore during the three days. The feature most influencing the strength of the easterlies is the southern migration of an anticyclone just east of Puerto Rico and the Lesser Antilles. The stronger easterlies link to a stronger pressure gradient and stronger high pushing south. Consequently, Fig. 7c relates to the time frame of Fig. 6f. In this instance, squalls greatly intensified and lasted longer than squalls that developed two days earlier (Fig. 7a) (Cohen et al. 1995).

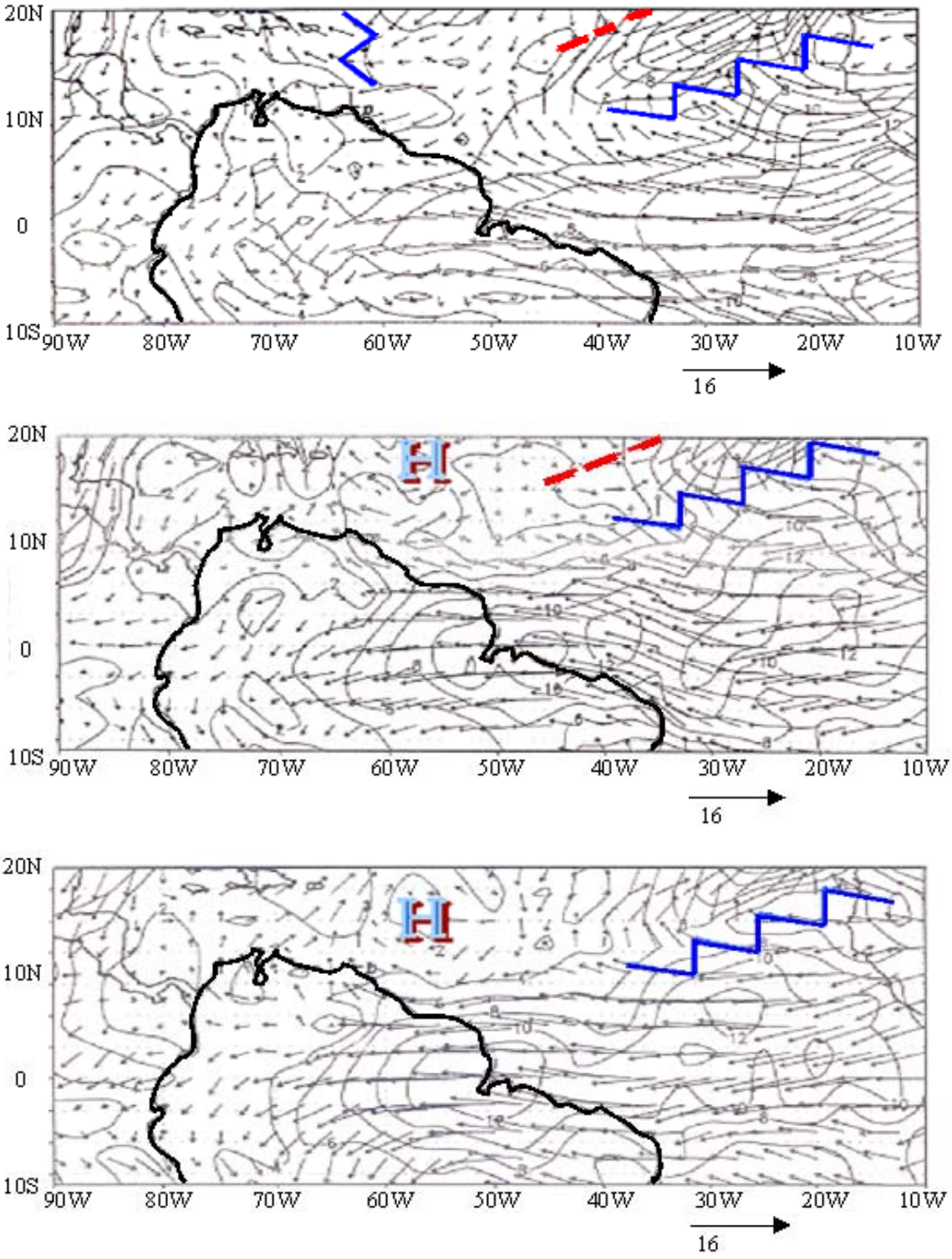

Fig. 7. 700 mb wind and isotach (m s^{-1}) analysis for 4 to 6 May 87 (modified from Cohen et al. 1995).

In addition to increasing easterlies, one must look at other factors such as divergence aloft and upward vertical motion fields advecting onto the coast with the increase in mass convergence. Cohen et al. (1995) found a tilt in the convergence-divergence pattern with divergence tilting westward to 200 mb. Low-level convergence from the easterlies relates to strong upward vertical motion. Frictional differences between sea and land also aid in the speed convergence of easterly winds. In addition, sea breezes help advect moisture inland raising the equivalent potential temperature thus creating instability and upward motion along the convergence zone (Cohen et al. 1995).

Finally, one must examine the vertical profile and movement of the squall lines. Squall lines intensify from vertical shear. Garstang et al. (1994) found surface winds around 5 kts increasing to 15-30 kts around 800 mb as the most ideal for development. Stronger vertical wind differences (wind shear) may result in LEs failing to re-initiate convection ahead of the parent LE. Winds typically back from 700-500 mb in response to evaporative cooling of the mid-tropospheric air while winds veer above this layer to 300 mb in response to latent heat warming. The mid-level cooling further destabilizes the atmosphere (Cohen et al. 1995; Garstang et al. 1994).

Garstang et al. (1994) found that storms within the LEs typically move almost due west at about 40º-60º to the right of the mean normal vector of the squall line. The translation speed of the individual storms is about 12-20 kts. Including both translation and propagation speeds, storms move rapidly at 25-35 kts to occasionally 40 kts (Cohen et al. 2000).

Squall lines are very important features, for they provide almost half of the rainfall to the Amazon Basin from April to August (Garstang et al. 1994). Squall lines

are especially frequent during April and May when the NET migrates or surges northward. Because squall lines last up to 48 hours, they can retain their structure as far west as the Andes. Squall lines can still produce large amounts of rainfall in Eastern Columbia and Eastern Peru during their wet season. Satellite imagery is pertinent for the detection of squall lines.

Trade wind surges can also enhance convection along the NET. They result from decaying polar fronts and shear lines often originating from pressure differences within the semi-permanent hemispheric sub-tropical highs (Fig. 8). The surge appears with slightly higher pressures behind the line. Satellite imagery becomes crucial for detection over the data-sparse jungle. Trade wind surge features are similar to tropical squall lines except trade wide surges only stretch in width 100-200 sm (Walters et al. 1989).

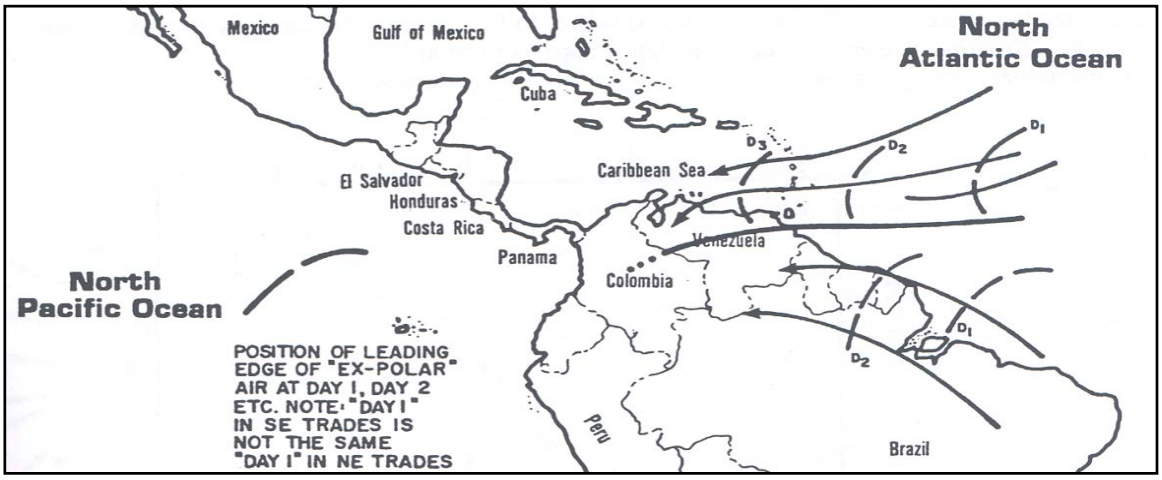

Fig. 8. Trade wind surges in northeast and southeast Atlantic trades (modified from Walters et al. 1989).

Another major synoptic scale feature is the Bolivian High. The upper-level high forms, as the name suggests, over the Bolivian Altiplano (the high plateau between the Cordillera Occidental and Cordillera Oriental). The Bolivian High dominates much of

South America (SA) during the austral summer. Figs. 9a-d illustrate the change in intensity and movement throughout the year. During the austral summer, the high builds due to intense release of sensible and latent heat (Davison 1999a). Due to the high altitude of the Altiplano (roughly 12000 ft), more sensible heat can reach the 300-200 mb levels than sensible heat originating near sea level. This is possible since the source of sensible heat is roughly 12000 ft closer to the 200-300 mb levels than heat released from a location near sea level. Also, large amounts of latent heat released principally from the NET also contribute to the high's formation. As the NET migrates northward, the high loses its source of latent heat, weakens, and migrates north with the NET. The high also weakens because of solar insulation decreasing over the Altiplano during the austral winter. The upper-level high aids in convective development by providing exhaust to squall lines or other thunderstorm clusters (Davison 1999a).

The sub-equatorial ridge and Amazon Low also enhance convection, upper-level divergence, and outflow. The east-west oriented upper-level ridge lies just north of the equator and aids in thunderstorm outflow (Figs. 9b-d). The sub-equatorial ridge strengthens during the austral winter as the Bolivian High weakens. The Amazon Low, a thermal low in the West Amazon Basin, aids in drawing the northeast trades towards and converging with the southeast trades. The low is a focus for convection and moisture and strengthens during the high sun-angle season (Davison 1999a). Figs. 10a and b depict the relationship between the low and the NET. The position of the low causes a maximum of rain in its vicinity (Walters et al. 1989).

Trade wind inversions are another major feature in the tropics. They change with the passing of the NET. As the dry season approaches, the inversion lowers and

strengthens with the southward migration of the North Atlantic sub-tropical high making updraft penetration into the inversion harder. Winds tend to back with height during the dry season vs. veering winds in the wet season. A weaker and higher inversion from the retreating North Atlantic sub-tropical high during the wet season allows for updraft penetration as more moist air rises mixing with dryer air aloft. Upper-level subsidence from sub-tropical mid to upper-level high pressure causes the inversions (Gilford et al. 1992; Ramage 1995). Inversion heights in NWSA typically range from 10,000 to 11,000 ft in Jul (wet season) to 8000 to 9000 ft in Jan (dry season) (Walters et al. 1989).

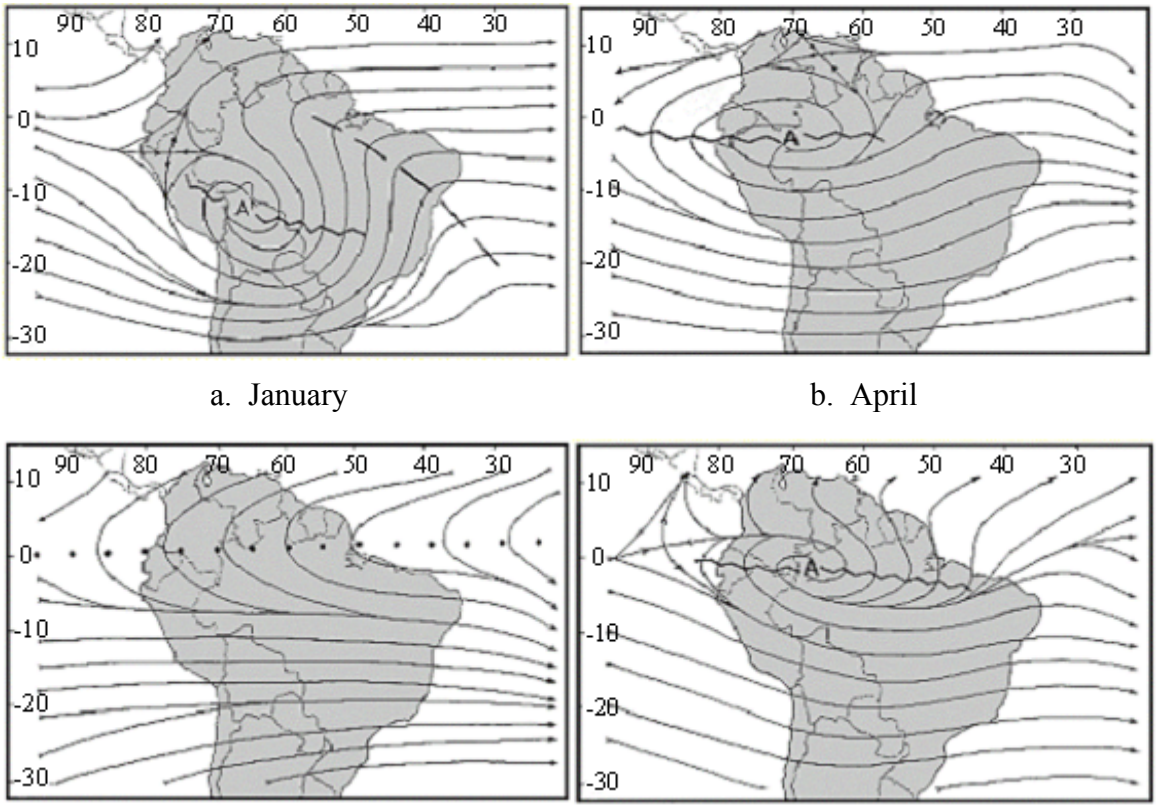

a. January b. April

c. July d. October

Fig. 9. Mean 200 mb positions of the Bolivian High, sub-equatorial ridge, and Brazilian tropical upper tropospheric trough (modified from Davison 1999a).

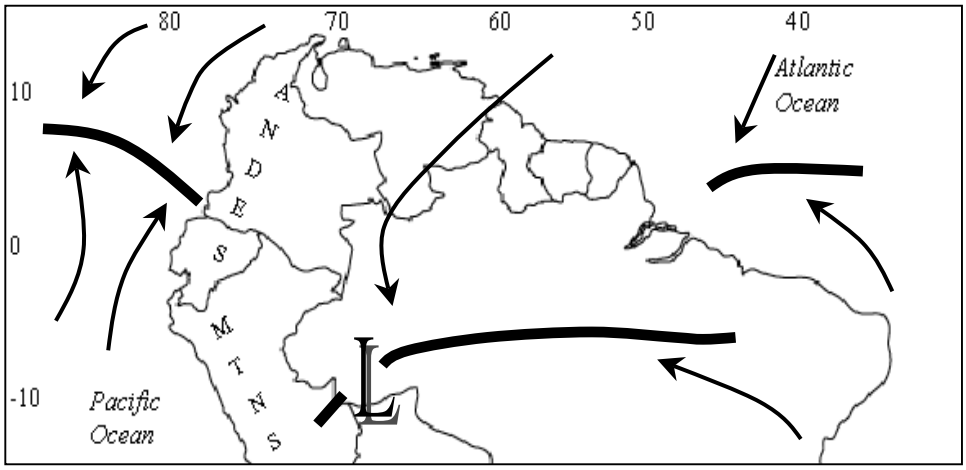

a. January

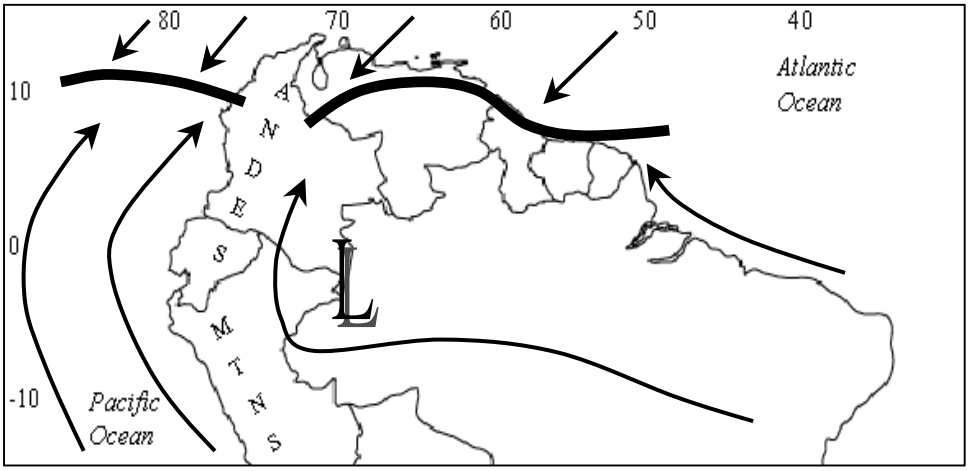

b. July

Fig. 10. Mean Amazon Low, NET (bold lines), and surface streamline (thin arrows) positions (modified from Davison 1999a).

Other features affecting the region include upper-level closed vortices, polar outbreaks, and the El Niño Southern Oscillation (ENSO). Virgi (1981) found occasional vortices propagating westward at the rate of 4˚ to 6˚ longitude per day. These vortices, seen well in satellite imagery, suppress outflow for convection. Strong Antarctic polar fronts occasionally push as far north as the Amazon Basin, especially in northern Peru and Ecuador, and less frequently crossing the equator into Columbia. Modified polar

outbreaks north of the Tropic of Capricorn, called friagens (friagem for singular), only occur with the strongest of cold surges during the austral winter. Unusually cool, dry, stable air and low stratus accompany the outbreak, which can occur once to several times per austral winter. Northern Peru and Ecuador experience severe weather with frontal passage on rare occasions (Walters et al. 1989). Finally, there is ENSO. A decrease in the NET intensity over the landmass from increased subsidence occurs with the negative phase of ENSO, El Niño, as the ITCZ strengthens on the other side of the Andes in the Pacific. Consequently, convection increases with the positive phase, La Niña (Schwerdtfeger 1976).

2.1.2. Local Effects. Local effects also control weather in different parts of the region. For example, the Columbian Highlands experience different cloud cover and rainfall distributions than the Western Amazon Basin in extreme Eastern Columbia and Eastern Peru. One very important factor, which influences weather in different locations along the Andes foothills, is the terrain.

The sharp, sudden rise in terrain in Columbia directly affects the easterly trades. The easternmost Andes range, the Cordillera Oriental, stretches the length of Columbia and Peru with heights ranging from 8000 to 14,000 ft. The direction of the terrain alters the low-level winds by channeling the Northern Hemisphere (NH) trades from the east-northeast and northeast and Southern Hemisphere (SH) trades from the south (Fig. 10b) (Kendrew 1942). The terrain also affects the Amazon Low. Although the Amazon Low is a thermal low, the convexity of the Andes Mountains plays a factor in the low's formation. The altered flow aids trade-wind convergence associated with the Amazon Low (Davison 1999a). Sometimes, the easterlies rise with topographic lift helping to

wring out more moisture over the foothills. If the direction of the low-level trades changes to southeasterly, then the flow becomes more perpendicular to the terrain in Columbia creating more uplift, producing larger rain amounts (Lenters and Cook 1999).

Katabatic flow, cooler air surging down the mountain at night and early morning, converges with easterlies producing localized convection along and just east of the foothills (Schwerdtfeger 1976). Edson and Condray (1989) found a double diurnal maximum in precipitation over the foothills region with one maxima occurring with daytime heating and another with katabatic flow convergence in early morning. Anabatic flow, warm air flowing up a mountain, usually develops around mid-morning terminating the down slope flow. Consequently, cumulus clouds start building over the mountains earlier in the day than over the foothills while storms disintegrate in the highlands east of the mountains. Local canyon and gap winds also aid in convergence.

Perhaps the most important driving factor in this region is the moisture availability. The vast Amazon Basin is a wealthy source of moisture. It is no surprise that roughly half the atmospheric water vapor content over this region results from a great deal of evapo-transpiration (Walters et al. 1989). The Western Amazon Basin comprises of endless mangrove trees, extensive rain forest, and tall swamp grass all of which are abundant in quantity and hold tremendous moisture. The Columbian and Ecuadorian Highlands, which contains less aerial coverage of jungle than the basin, still support the adjacent environment with moisture from tropical savanna (Walters et al. 1989). Absolute humidities over the entire region quite often exceed 20 g/m^3 (Edson and Condray 1989).

Localized differential heating also causes disparities in storm locations. Regions with less vegetative moisture may yield more conduction causing diurnal storm flare-ups earlier in the day than locations still shrouded in morning fog and stratus (in areas of higher vegetative moisture). This is due to dryer land heating faster than moister areas of land. Local heating of the foothills can also contribute to conduction and steeper lapse rates due to differential heating of the mountainsides (Schwerdtfeger 1976).

2.1.3. Climatology of Columbia, Ecuador, and Northern Peru east of the Andes.

The region of interest receives annual rainfall amounts from 120" to 150" per year. Table 2 shows the distribution of rainfall per region throughout the year (AFCCC 2002; Gilford et al. 1992; Walters et al. 1989). One can relate the migration of the NET to rainfall amounts. Note how the West Amazon Basin in Columbia never experiences a true dry season while the highlands have a marked dry season. This is due to the fragmentation of the NET and presence of the Amazon Low. Also, moisture surges during the initial onset of the rainy season occur with the initial northward passing of the NET causing even higher rainfall amounts than shown in Table 2. On average, rainfall occurs almost every day during the wet season and once in about four days during the dry season (Walters et al. 1989).

Table 2. Average monthly and seasonal rainfall distributions for NWSA.

Eastern Andes Foothills and Western Columbian Highlands (0º-7º N / 73º-77º W including Columbian locations: Apiay Air Base, Florencia, Larandia, Puerto Asis, and Villavicencio)		
Month	**Season**	**Rain per month (inches)**
Apr-Nov	Wet	14-20
Dec	Transition	6-8
Jan-Feb	Dry	2-5 (0º-3º N for Feb: 6”-8”)
Mar	Transition	6-8 (0º-3º N: 10”-15”)
Eastern Columbian Highlands (0º-7º N / 70º-75º W including Iauarete, Brazil and San José del Guaviare and Tres Equinas, Columbia)		
Month	**Season**	**Rain per month (inches)**
Apr-Oct	Wet	9-15
Nov-Dec	Transition	4-6
Jan-Feb	Dry	1-3
Mar	Transition	4-6
West Amazon Basin (0º-5º S / 70º-75º W including Benjamin Constant, Brazil; Iquitos, Peru; and Leticia, Columbia)		
Month	**Season**	**Rain per month (inches)**
Oct-May	Wet	10-15
Jun	Transition	8-10
Jul-Aug	Dry	5-8
Sep	Transition	8-10

Surface and tropospheric winds generally remain easterly throughout the year with some exceptions. For the Columbian Highlands and the foothills, surface winds are southerly and southeasterly during the wet season and northeasterly during the dry season with a magnitude of 5-10 knots. Direction changes with the passage of the NET. The West Amazon Basin, however, experiences only subtle meridional fluctuations and weaker wind magnitudes. Surface winds can become westerly very close to mountain gaps with katabatic flows and just north of the Amazon Low (Fig. 10b). Winds generally

remain easterly throughout the lower and middle troposphere (up to 500 mb). Above this level, winds turn with the passage of the Bolivian High and sub-equatorial ridge. Westerly winds are prevalent in Northern Peru as the high migrates north (Figs. 9b-d). Also, NH mid to upper-level westerlies penetrate into Columbia during boreal winter with the onset of the dry season (Figs. 9a). Upper-level easterlies are strongest just north of the Bolivian High. The added momentum can aid in tropical development. Winds speeds are generally around 20-30 knots except stronger winds of 35-45 knots are possible in areas just north of the Bolivian High (AFCCC 2002; Gilford et al. 1992; Walters et al. 1989).

Cloud bases and stratus are major hindrances for military operations. Typically low stratus is a problem in the early to mid-morning hours (03-09 local time (L)) with bases lowering to 300-1000 ft. These ceilings occur, on average, 15-25% of the time in the early to mid-morning in all locations, except 5-15% from Dec-Feb in the Columbian Highlands and foothills. Lower moisture content likely causes the seasonal minimum. Bases also lower to 500-1000 ft with thunderstorms. On average, cloud bases of 500-1000 ft during the afternoon occur 10-20% of the time during the wet season and about 5-10% of time during the dry season in the highlands and foothills but 5-10% year-round in the basin. Bases lower than 1000 ft occur only 3-5% during all other times in all locations. Although katabatic rains do occur, they seldom produce rain intensities and cloud bases as low as afternoon rains. On a side note, Villavicencio experiences percentages slightly less than those mentioned (AFCCC 2002; Edson and Condray 1989; Gilford et al. 1992; Walters et al. 1989).

Cloud bases lower than 3000 ft occur frequently. On average, they occur 20-30% of the time during the dry season in the highlands and foothills, 33-50% during the dry season in the basin, and 33-50% during the wet season everywhere from early morning to sunset except with slightly less probability during late morning (09-12 L) and after sunset. Low ceilings occur at night because of fog and katabatic rains and during the day because of convection. One major exception is Villavicencio, which experiences occurrences roughly half of other locations. Villavicencio's close proximity to the Andes (approximately 20 nm) likely adds localized affects to the averages. Over the Amazon Basin, katabatic winds aren't the problem; fog and low stratus becomes an increased factor due to higher moisture content. Dry season fog can occur from increased radiational cooling and SH polar outbreaks in Northern Peru, Ecuador, and, less frequently, in Southern Columbia. Night-time drizzle and low stratus decks with bases about 1000 ft accompany the friagens that last from 24 to as much as 96 hours on extreme occasions (AFCCC 2002; Edson and Condray 1989; Gilford et al. 1992; Walters et al. 1989).

As discussed, fog is a problem in the region of study. Edson and Condray (1989) found fog (with visibility less than one mile) occurring about 1-2% of the time, but mainly during the early to mid morning hours. Naturally, fog thickens as nighttime hours increase. Bases less than 300 ft, although rare, do occur mainly in the more moisture rich West Amazon Basin. Occurrences with bases less than 300 ft are about 3-5% in the basin during the wet season and 5-10% in the basin during the dry season to less than 1% in the highlands for all seasons. The higher frequency (5-10%) is likely due to more radiational

cooling during the dry season. Fog (with visibility greater than one mile) occurs an additional 1-2% of the time in both the basin and highlands.

Another deterrent to operations is visibility and heavy rains. Low visibilities, previously mentioned, occur during the early-mid AM hours with fog and low stratus. Low visibilities also occur with daily rainfall. When heavy rains occur, visibility can quickly become ¼ to ½ sm or less; however, the intense rains are short lived. Visibilities of 2-5 sm are much more common with stratified moderate rains following the intense rains and with weaker convection. Edson and Condray (1989) found the maximum of intense rainfall to occur around sunset (near maximum heating) about 2% of the time. The maximum probability of total rainfall is actually in the early to mid-morning hours in the highlands and foothills (about 15-20% for wet season AM vs. 10-15% for the wet season late afternoon). The basin experiences a uniform 10-15% for all times during the wet season. Probabilities decrease by half for the dry season for all locations (AFCCC 2002; Edson and Conroy 1989). As discussed above, katabatic wind convergence initiates the less intense nocturnal rains. Occurrences of nocturnal rains are less in the West Amazon Basin.

2.2. Forecasting Mesoscale Convective Complexes in Northern Argentina, Southern Brazil, Paraguay, and Uruguay.

2.2.1. Structure and Behavior of Mesoscale Convective Complexes. Maddox (1980) and the *Glossary of Meteorology* (2000) define an MCC as an MCS exhibiting a large, circular, cold, long-lived cloud shield meeting the following requirements: Size: Cloud shield continuously having an infrared (IR) temp $\leq$ -32º C and size $\geq$ 100,000

km^2 (roughly the size of Iowa) with interior region having IR temp $\leq$ -52º C and size $\geq$ 50,000 km^2 and eccentricity (minor axis/major axis) of ≥ 0.7 during time of maximum extent. Duration: The above criteria must remain for at least 6 hours. The maximum extent occurs when the $\leq$ -32º C cloud shield reaches its maximum size. Initiation and termination of the MCC occurs with respect to the above size criteria.

MCCs are elliptical, warm core systems exhibiting a low surface pressure and strong anticyclonic flow aloft. The longer an MCC persists, the more elliptical it becomes. Like tropical storms, they are not baroclinic in the sense that they don't transport sensible heat poleward. MCCs can also alter their surrounding environment (Maddox et al. 1986).

MCCs develop from initial convection during the maximum heating hours and blossom into their elliptic structure during the night. MCCs must develop in a region with weak to moderate shear and moist, strong, warm low-level inflow or jet (LLJ) converging with a predominately east-west oriented boundary (e.g. squall line, quasi-stationary front, outflow boundary). There is usually a weak to moderate upper-level short wave accompanied by weak positive vorticity advection (PVA) and diffluence aloft. Anticyclonic flow aloft prevails from 200-100 mb. The lack of surface radiational cooling and high albedoes from cloud top cooling both aid in destabilizing the system. MCCs terminate once they move into a more stable environment (Maddox et al. 1986).

MCCs usually develop a mesocyclonic rotation within their structure. If convection occurs long enough, a meso-scale warm-core vortex forms. This vorticity can remain after the MCC dies and can spawn new development the following day (Velasco and Fritsch 1987).

MCCs, like supercells, generally move equatorward toward the inflow and toward the equivalent potential temperature ridge, which lies just east and equatorward of the system. Like tropical storms, latent heat drives the MCC. MCCs move, with some exceptions, equatorward of the 700-500 mb mean flow and equatorward of the mean 850-300 mb thickness lines (or 850-300 mb thermal wind) at about 10-20 m/s. Although individual cells move with the mean flow, new cells developing along the equatorward and western flank cause the system to propagate equatorward of the mean flow. An MCC, which has ceased to produce new convection, is more likely not to turn equatorward of the mean flow (Maddox et al. 1986).

Although severe downbursts, large hail, and tornadoes are common during the initial stages of MCC development, flooding is the main concern. Severe weather probabilities diminish significantly once the MCC fully organizes. The strongest precipitation typically occurs in the eastern and equatorward sectors (within the coldest IR temps) with an expansive stratified rain region extending beyond the initial flank (Maddox et al. 1986).

2.2.2. Comparison between North and South American MCCs. MCCs in SA exhibit many similarities and differences to their NA counterpart. Tables 3 and 4 are adapted from Velasco and Fritsch (1987).

Table 3. Similarities between NA and SA MCCs.

-	Nocturnal maxima in intensity
-	Moist low level flow advecting poleward
-	Mountain chain to west helps initiate convection and channel LLJ (20-30% of systems originate over mountains)
-	MCCs form in sub-tropics and mid-latitudes
-	Documented nocturnal maxima in rainfall
-	Rainfall accounts for a large portion of the region's total rainfall
-	Most MCCs occur in late spring to early summer
-	Comparable surface temperatures
-	Exhibit same dynamic structure and basic causes of formation
-	Favored region of initiation shifts west in summer
-	Speed of the LLJ is comparable among NA and SA MCCs

Table 4. Differences between NA and SA MCCs.

-	SA MCCs are about 60% larger then NA MCCs
-	MCCs develop later and last longer in SA
-	Surface dewpoint values average 18º to 20º in NA but 20º to 24º in SA
-	MCCs initiate and migrate seasonally from 30º to 50º in NA but 25º to 35º in SA
-	Higher surface dewpoints and similar surface temperatures imply greater thermodynamic potential for instability in SA
-	MCCs form around the 20º C isodrosotherm in SA compared to 15º C in NA
-	Average 500 mb temperature is -10º C in NA but -8º C in SA
-	Tropopause is around 100 mb in SA MCCs vs. 150 to 200 mb in NA MCCs
-	LLJ develops earlier in the day and is longer lived in SA
-	Terrain is much steeper in SA (Andes rise to over 20,000 ft)
-	Unlike NA, SA MCCs can occur well into late summer and autumn
-	Source of moisture is Amazon Basin (land) in SA vs. Gulf of Mexico in NA

To explain the differences, one must first understand the governing large-scale features.

2.2.3. Synoptic-Scale Features. The placement and strength of the Bolivian High and the sub-tropical jet (STJ) work in concert to aid MCC development. The high interacting with the STJ and the Eastern Brazilian tropical upper tropospheric trough (also called the Nordeste Low) work in concert to provide upper-level shortwaves and outflow for MCCs (Fig. 9a). The high shifting southward adds to the upper-level geopotential gradient, which, in turn, strengthens the STJ. The region south and east of the high is favorable for diffluence aloft from STJ divergence. A stronger, nearly zonal STJ results in more kinetic energy crossing the very high Andes at a perpendicular angle resulting in shortwave perturbations and increased potential vorticity (Davison 1999b). Consequently, the favored region for MCC development and movement (discussed later) lie in the same area.

The South Atlantic High also affects CSA. Fig. 11 shows the location of the ridge associated with the high (located just east of the map). The high strengthens in summer and migrates south. The northerly flow around the high, through Bolivia and the Gran Chaco region (N. Argentina and Paraguay), is critical for LLJ formation (discussed later). When the high shifts westward, the northerly flow increases as it interacts with the North Argentine depression (NAD), therefore, increasing the strength of the LLJ (Nogues-Paegle at al. 2002).

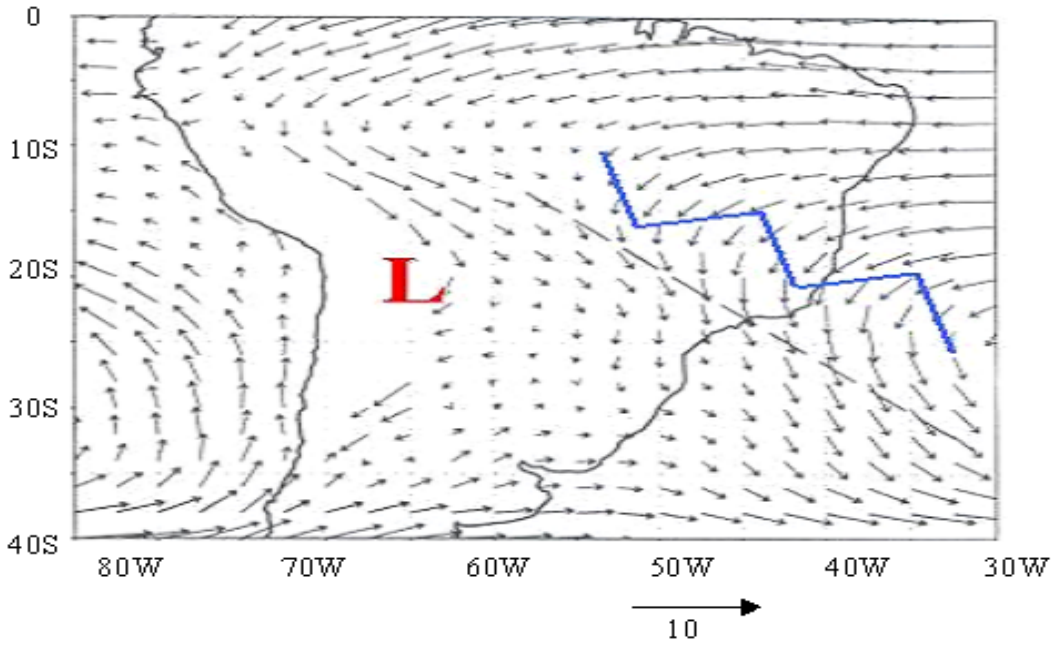

Fig. 11. Mean positions of the NAD, SACZ (dashed line), South Atlantic ridge, and 850 mb vectors (m s^{-1}) during Dec to Feb (modified from Lenters and Cook 1999).

The NAD forms into a lee-side, thermal trough that remains nearly stationary throughout the summer. Westerlies crossing the Andes create the lee-trough and strong adiabatic compression. The very hot, dry westerly foehn winds in CSA are called Zondas. Temperatures quite often reach 110º-115º F nearly every summer in Gran Chaco partly because of the winds. The localized maximum in sensible heat strengthens the shallow low. Sea-level pressures often drop to 980 mb (much lower than the Southwest US thermal low). The low lies nearly underneath the powerful Bolivian High making this an amazingly strong warm-core system. The NAD strengthens during the day reaching a maximum around sunset and weakens during the night reaching a minimum by dawn. Consequently, the LLJ intensifies late in the afternoon into the night as the thermal low reaches its maxima (Kendrew 1942; Schwerdtfeger 1976). Wind speed intensity lags the NAD intensity by several hours. The low, in concert with the South

Atlantic High (Fig. 11), creates a strong low-level pressure gradient, which favors a stronger LLJ (Saulo et al. 2000).

A unique feature of SA weather is the presence of the South Atlantic or South American convergence zone (SACZ). The SACZ is a zone of mass convergence climatologically stretching from the Atlantic Ocean northwestward into Southern Brazil and eventually reaching Northern Bolivia (Fig. 11). The SACZ forms from convergence from the South Atlantic High and flow channeling east of the NAD and Andes. Large amounts of precipitation are generated from this primarily summer feature. Fig. 11 also shows a surface ridge parallel and north of the SACZ. The strength and placement of this ridge influences the SACZ placement. When the ridge and high build west, the SACZ moves west increasing the low-level northerly flow east of the Andes (Lenters and Cook 1999).

Cold-core upper level troughs over Uruguay and Eastern Argentina displace the Bolivian High southwestward helping to intensify the SACZ (Nogues-Paegle et al. 2002). However, cool southerly winds accompany the cold-core low. These winds stabilize the air mass aiding in an eastward placement of the SACZ, which weakens the low-level pressure gradient and LLJ (Lenters and Cook 1999).

South American MCCs owe their existence, like their NA counterpart, to a LLJ. Saulo et al. (2000) found the average velocity of the South American low-level jet (SALLJ) to be around 20 m s^{-1} with its maximum located around 5000 to 5500 ft (approximately 850 mb). This is comparable in strength and level of placement to that found in the United States (US) (Bonner 1968). The SALLJ, perhaps one of the most studied features in the continent, is more persistent and lasts longer into the season than

the LLJ found in the US. The SALLJ transports tremendous amounts of moisture from the Amazon Basin southward into the region, which is unique in that the moisture source is over land versus the Gulf of Mexico. Since the source region experiences more direct radiation than the Gulf of Mexico, the moisture is much warmer, which increases thermal instability. Dewpoints often exceed 24º C and equivalent temperatures reach or exceed 340º K in the Gran Chaco region (Baetghen et al. 2001; Davison 1999b).

The SALLJ actually maintains a presence year round, although it strengthens considerably during the summer (Fig. 12). Saulo et al. (2000) defined the SALLJ as a maximum of northerly winds at least 12 m s^{-1} near 850 mb with at least a 6 m s^{-1} shear between 850 or 900 mb and 700 mb. Fig. 13 illustrates the nocturnal behavior of the SALLJ. The SALLJ increases towards sunset (00 UTC) as the intensifying thermal low (NAD) approaches its maxima. The SALLJ reaches its maximum between 00 and 06 UTC when the NAD begins weakening. Loss of sensible heating weakens the NAD then weakens the SALLJ, which eventually reaches a minimum speed around 18 UTC. The process differs from the US, for the US LLJ doesn't strengthen at sunset and doesn't exist primarily from a thermal low presence.

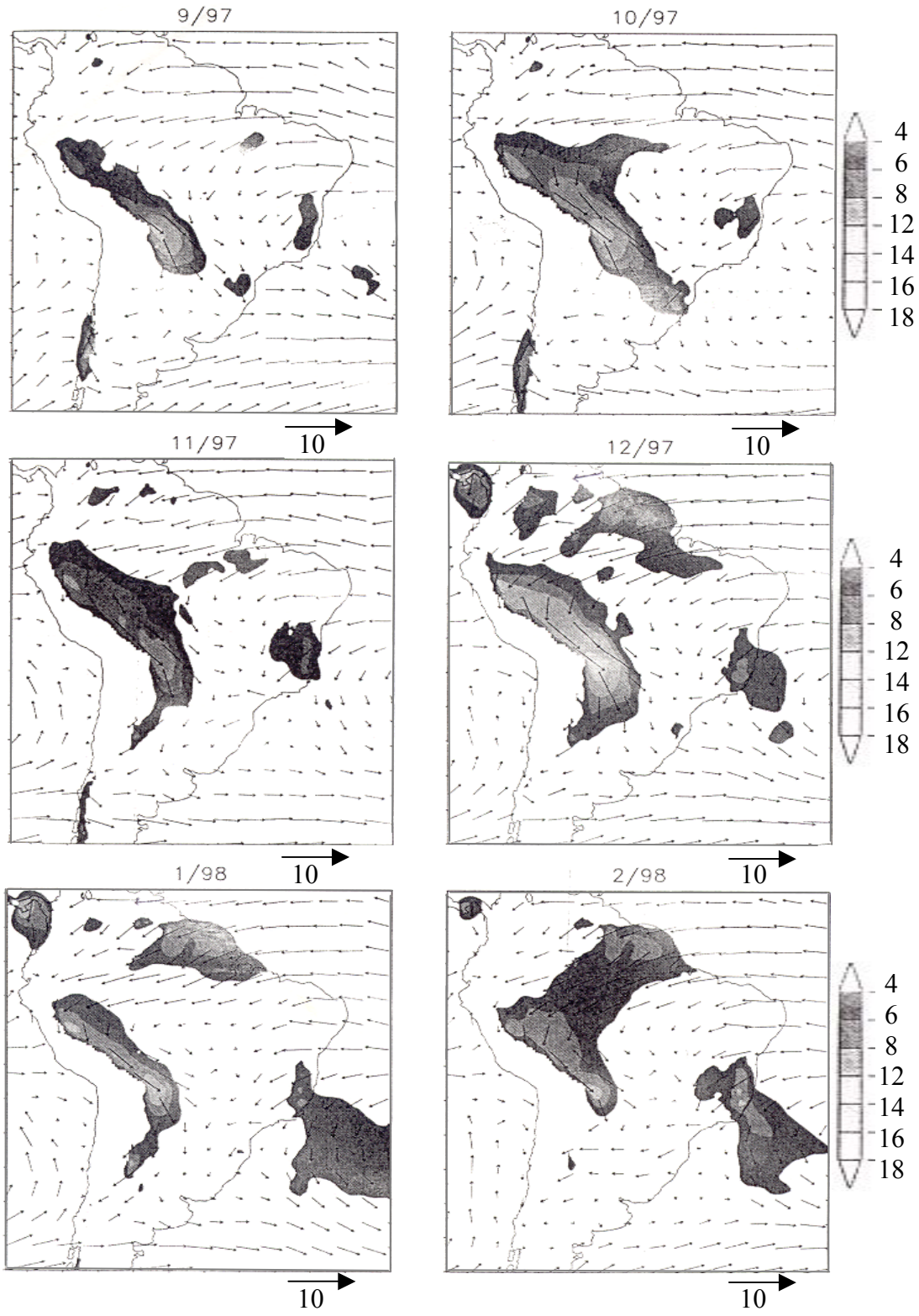

Fig. 12. Mean monthly northerly wind components (m s^{-1}) at 850 mb at 00 UTC from Sep 1997 to Feb 1998. Shading represents isotachs (modified from Saulo et al. 2000).

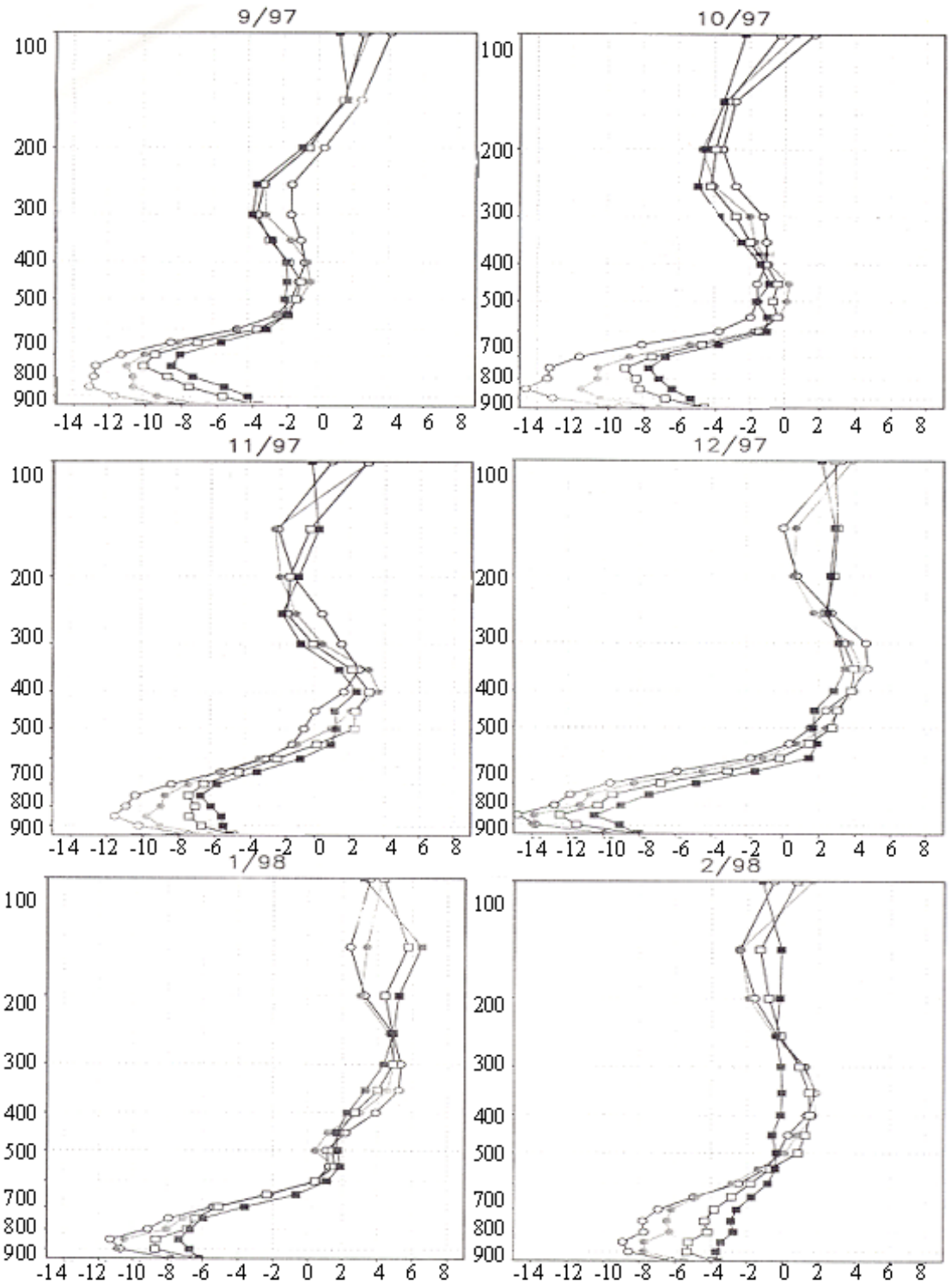

Fig. 13. Mean monthly vertical meridional (v-component) wind profile (m s^{-1}) for Santa Cruz, Bolivia from Sep 1997 to Feb 1998. Vertical axis represents pressure (mb). Each profile corresponds to a different time (00 UTC-open circles; 06 UTC-filled circles; 12 UTC-open squares; 18 UTC-filled squares) (modified from Saulo et al. 2000).

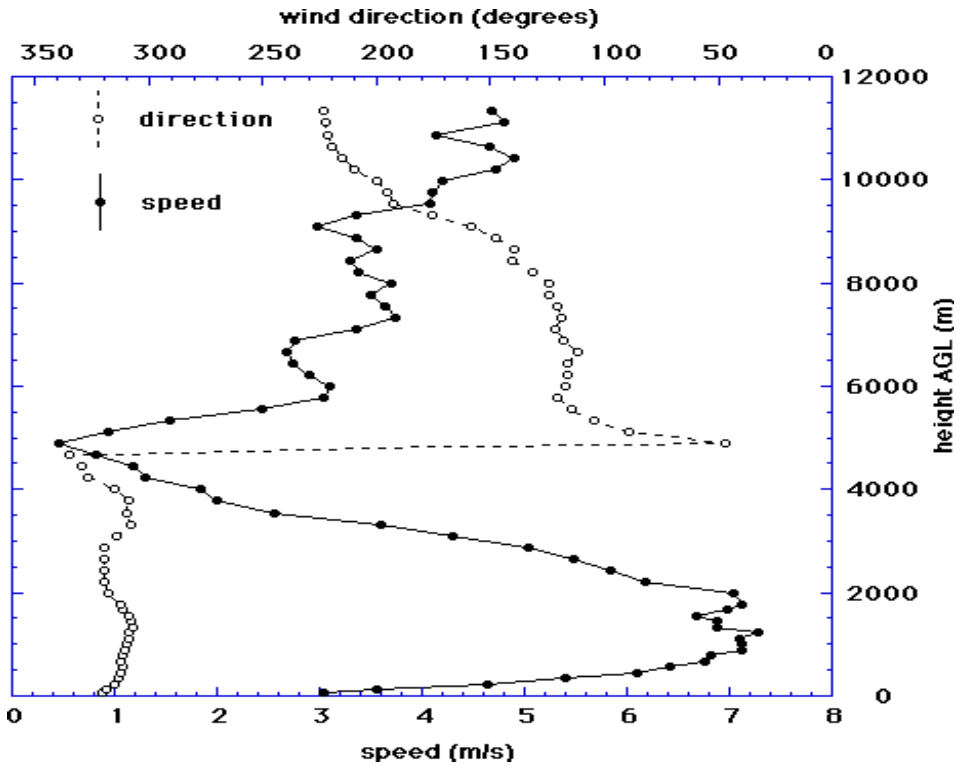

Fig. 14. Profile of meridional wind speed and zonal wind direction of the mean Santa Cruz, Bolivia sounding from Jan to Mar 1998 (modified from Douglas et al. 1998).

Fig. 14 illustrates the sharp switch around 4 km from northerly winds to southwesterly winds, which are caused by flow around the Bolivian High. Figs. 13 and 14 both show the maximum in wind speeds around 1.5 km to 2 km, which compares well to the US LLJ. The SALLJ reaches its maximum intensity near Santa Cruz, Bolivia (Figs. 13 and 14) and remains there year round. During austral summer, the SALLJ strengthens and extends southward to the Gran Chaco region. The SALLJ typically turns southeastward in response to the Coriolis force and placement of the SACZ. Fig. 12 depicts winds drastically weakening just south of the SALLJ maximum (exit region) (Douglas et al. 1998; Saulo et al. 2000). The exit region creates speed convergence thus becoming the area of severe weather formation (Schwerdtfeger 1976).

As was previously mentioned, the SALLJ placement and intensity is related to the NAD, South Atlantic High, and SACZ. Decreases in frictional drag from air sliding above a nocturnal inversion versus land classically increase speeds of LLJs (Bonner 1968). In addition, migratory mid-latitude systems crossing the Andes help channel flow southward ahead of trough passage. The SALLJ advects warmer, moister air underneath a shortwave further destabilizing the atmosphere. The opposite effect occurs once the shortwave moves east. Fig. 15 illustrates how the area of maximum upward vertical motion migrates east and northward as the surface low and associated shortwave passes. The SALLJ converges with the flow around the surface low. Garreaud and Wallace (1998) found that migratory low interaction with the SALLJ lowers the level of free convection (LFC) to 780 mb versus the climatological average of 600 mb.

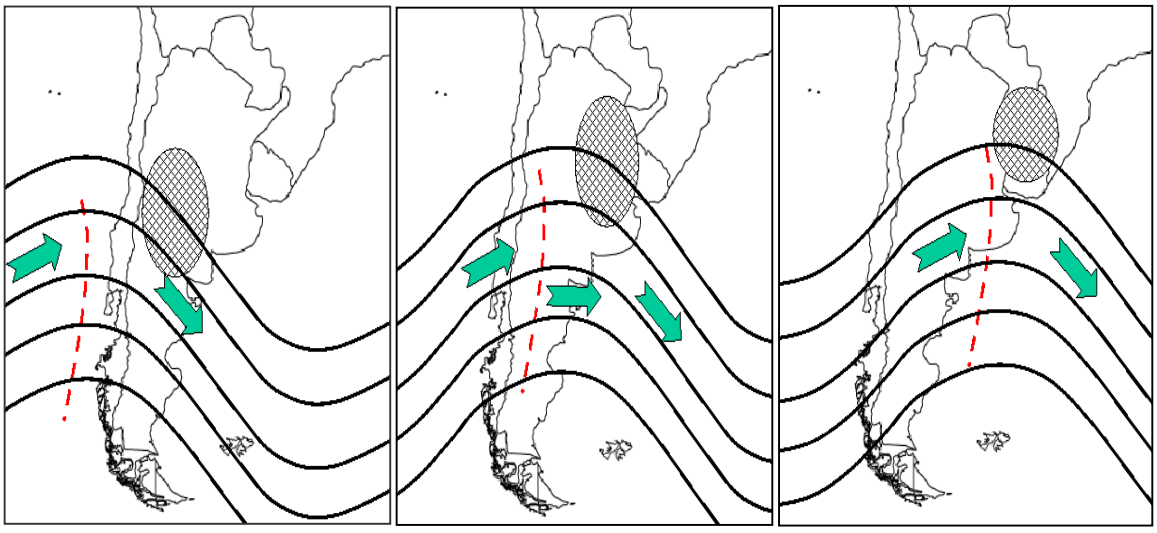

Fig. 15. 500 mb geopotential height (contours) and areas of maximum upward vertical motion (hatched circles) for a migratory shortwave passage over three days. Contour interval is 100 m with maximum value of 5800 m. Arrows represent 500 mb wind flow.

Polar fronts interacting with the SALLJ help create upward vertical motions producing the most dangerous thunderstorms in the continent (winds 50-80 kts, large hail and tornadoes). Squall lines and other MCSs occur more often than MCCs with strong northward polar pushes, for the shear is too great to sustain MCC development. Pamperoes, cold southerly winds, along with the Argentine continental polar high stabilize the atmosphere behind polar fronts preventing convection. However, when polar fronts stall or weaken into shear lines, mid to upper-level shear may weaken enough for MCC development. The strength of the associated upper-level shortwave should either lead to a squall line severe weather outbreak, MCC development, or an MCS not quite attaining MCC status (Gilford et al. 1992).

Finally, the ENSO has a documented significant impact on MCC frequency. El Niño generates a tremendous domino effect. The Bolivian High strengthens creating a tighter geopotential gradient in the STJ leading to more shortwave perturbations sliding off the Andes. The stronger high also aids in more diffluence. At the surface, the South Atlantic High strengthens building further west and creating stronger pressure gradients with the NAD, which is also stronger. The NAD increases due to higher condensational and sensible heating of CSA. Latent and sensible heat increases generate greater geopotential heights and, therefore, more adiabatic compression. Increases in convection over Chili and Peru provide latent heat into the Bolivian High. MCCs generate more latent heat thus creating a positive feedback. MCCs can more than double in frequency during a very strong El Niño. Alternately, MCC frequency declines with strong La Niña events (Lenters and Cook 1999; Velasco and Fritsch 1987).

2.2.4. South American MCC Climatology and Features. As listed in section 2.2.2., MCCs differ from NA MCCs for various reasons. The increased size and longer duration both relate to higher surface dewpoints, a longer lasting LLJ, and MCCs forming more equatorward than in NA. MCCs exist well into the austral summer and autumn from the yearly presence of the SALLJ. The US LLJ forms much further from the Rockies and with the absence of a thermal low. The SALLJ forms only within 300 sm of the much steeper Andes and with the aid of a thermal low (the NAD), which both greatly aid in channeling more mass poleward. Finally, the nearly constant placement of the STJ limits the meridional extent of SA MCC formation; therefore, many MCCs occur in the same areas year round (Velasco and Fritsch 1987).

The vast majority of MCCs initiate along or just east of the Andes foothills. Fig. 16 depicts the areas of initiation and movement for storms over two seasons. Initiation favors the Parana River Basin (NE Argentina) and Paraguay in Nov with initiation areas shifting westward into Gran Chaco with the season. MCCs almost always track eastward and turn left (toward the low level inflow) with respect to the mean mid-upper level flow as the system matures. Most systems track into the Parana Basin, Uruguay, and Southeastern Brazil before termination (Fig. 16). The MCC's maximum extent (Fig. 17) and, consequently, the lion's share of rainfall occurs here. Occasionally, MCCs do track into the Rio de la Plata (Montevideo and Buenos Aires region). Very few MCCs, however, survive the trip to the Atlantic Ocean. Although Fig. 16 illustrates a maximum in Nov from a two season study, Jan climatologically receives the most MCC occurrences with Dec and Feb following second and third respectively in monthly frequency (Velasco and Fritsch 1987).

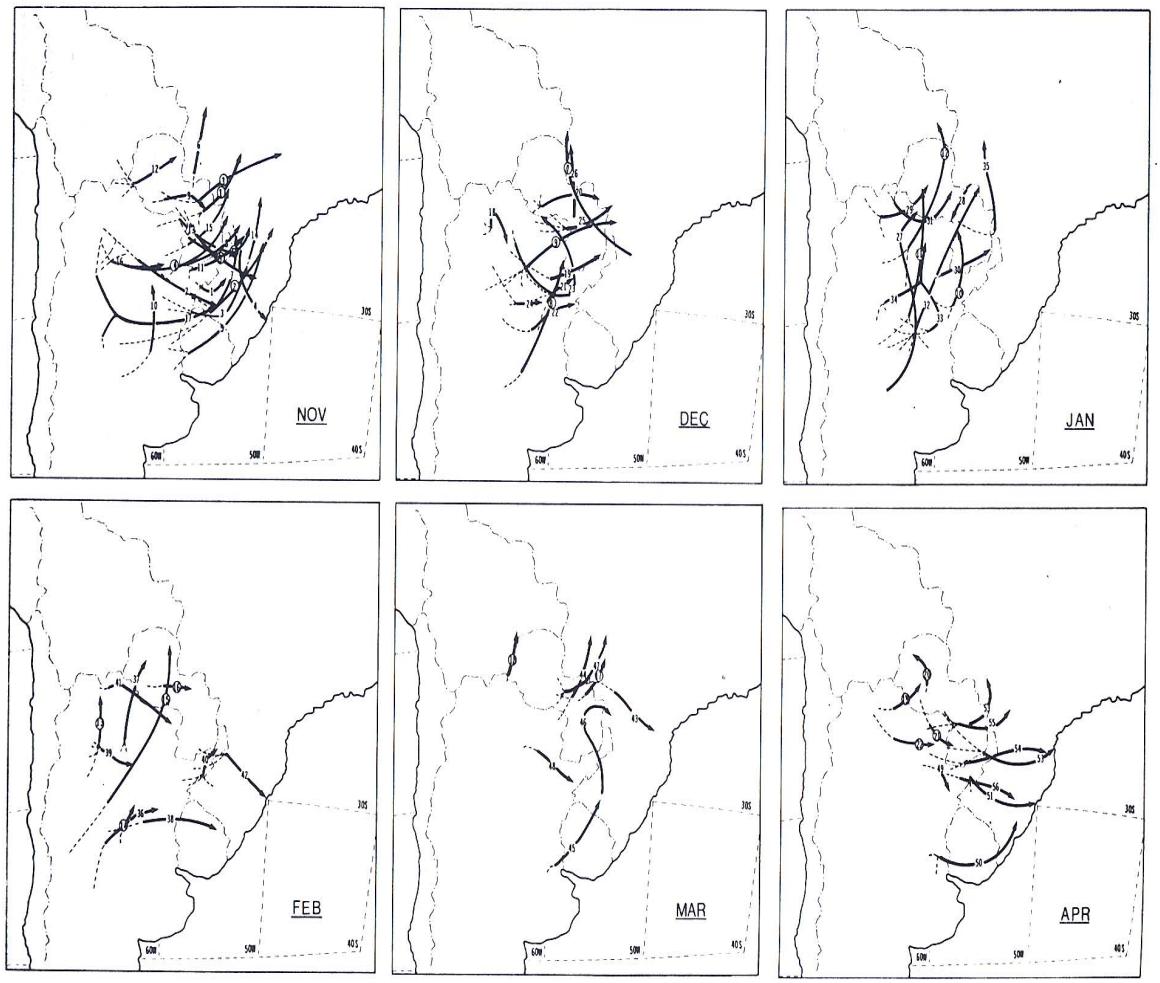

Fig. 16. Tracks of mid-latitude South American MCCs from the 1981-82 and 1982-83 austral summers. Dashed lines indicate tracks of first thunderstorms. Numbers labeled on the tracks are non-applicable (modified from Velasco and Fritsch 1987).

Velasco and Fritsch (1987) note an interesting occurrence: the time of first convection actually has a double maxima (Fig. 18) with the second maxima probably caused by katabatic winds from the Andes colliding with synoptic low level flow. MCCs reach their maximum intensity around 04 L, about four hours later than NA MCCs. Termination also occurs later, around 10 L versus 06 L in NA. SA MCCs average 11.5 hours in life span versus about 9 to 9.5 hours for NA MCCs (Maddox et al. 1986; Velasco and Fritsch 1987).

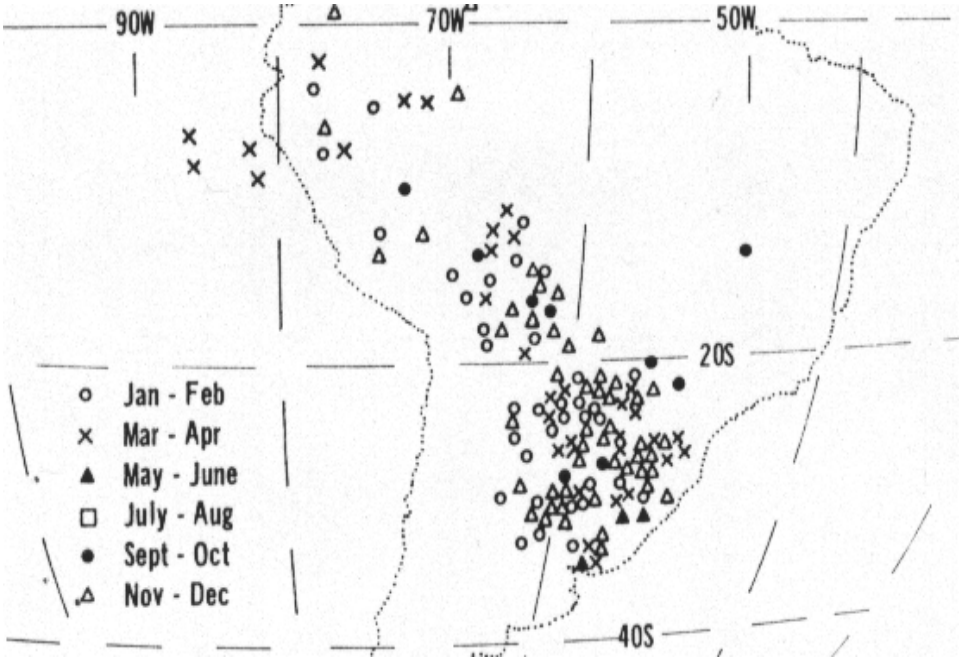

Fig. 17. Locations of South American MCC maximum extent from the 1981-82 and 1982-83 austral summers (modified from Velasco and Fritsch 1987).

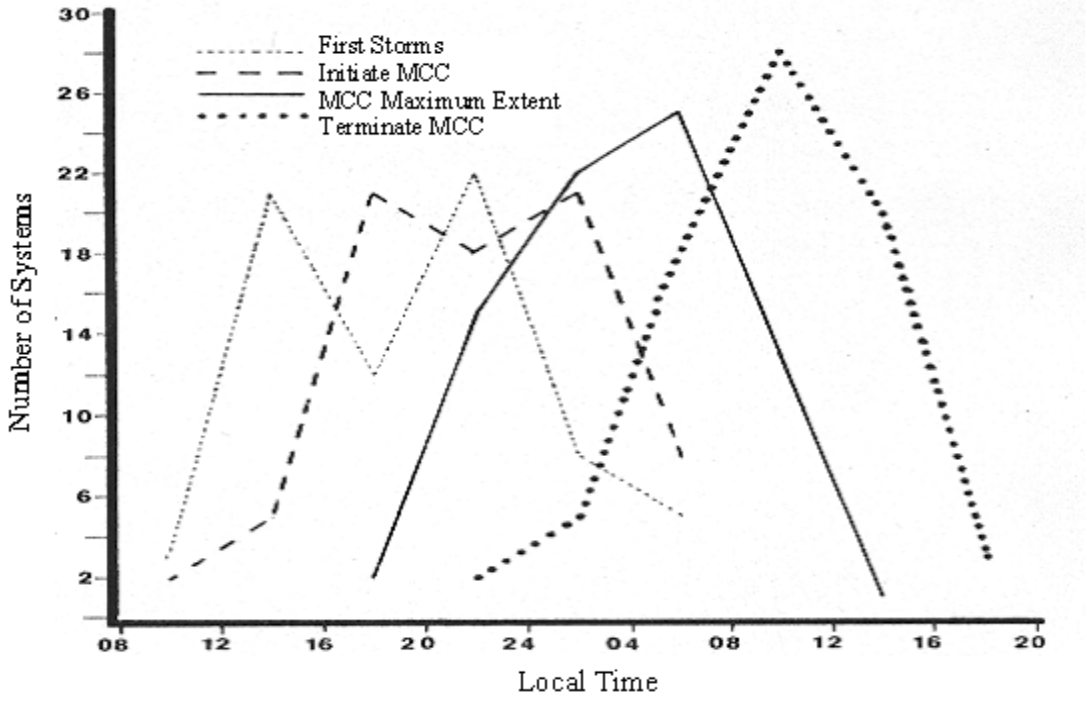

Fig. 18. Average life cycle of mid-latitude South American MCCs from the 1981-82 and 1982-83 austral summers (modified from Velasco and Fritsch 1987).

The average size of SA MCCs is much larger than NA MCCs. The main difference is the enormous extent of the -32º C cloud shield. Velasco and Fritsch (1987) found this shield to average around 400,000 km^2 but around 500,000 km^2 during an El Niño year while NA MCCs average only 300,000 km^2. The inner core shield (-52º C) average, however, matched the NA average of 190,000 km^2. Higher moisture fluxes and energy availability likely caused the larger shields during the intense '82-'83 negative ENSO year. In addition, higher tropopauses with SA MCCs are likely linked to colder cloud tops (Velasco and Fritsch 1987).

MCCs provide most of the rainfall from late spring to autumn in Northern Argentina, Paraguay, and Uruguay. Climatologically, 4"-6" per month fall in Gran Chaco and the Parana Basin during the summer with about 2"-4" in Uruguay. Spring and autumn yield opposite rainfall distributions. Enormous 6"-12" 24-hour rainfall amounts have occurred in the Parana Basin, Uruguay, and the Rio de la Plata from intense MCSs and MCCs (Gilford et al. 1992). Low cloud bases just less than 1000 ft, cloud tops exceeding 50,000 ft, and visibility much less than one statute mile often accompany MCCs and intense MCSs (Gilford et al. 1992).

III. Data

3.1. Excessive Rainfall, Fog, and Low-Cloud Bases over Columbia, Ecuador, and Northern Peru east of the Andes.

3.1.1. Satellite and Reanalysis Data. This research utilized satellite imagery and reanalysis charts to find common precursors to heavy rainfall events. Satellite imagery used is from both geostationary and polar-orbiting satellites. Due to data and cost restrictions, limited archived visible and infrared Geostationary Operational Environmental Satellite (GOES) imagery from GOES-7 and GOES-8 were available from 1995 and 1996 from NCDC (NCDC 2002). However, the Space Physics Interactive Data Resource (SPIDR) supplied an ample amount of polar-orbiting visible and infrared imagery through the NGDC (NGDC 2002). Imagery was available for the length of the POR using DMSP F10-F15 satellites. Despite the irregular schedule of polar-orbiting images, there were enough DMSP images available through the SPIDR from multiple passes and all available satellites to view and analyze a weather system's evolution, intensity, movement, and decay.

NCAR supplied a binary format of reanalysis data that's taken from the Global Data Assimilation System (GDAS) model at the former National Meteorological Center (now called the National Center for Environmental Prediction (NCEP)). NCAR received the data from the NMC and stored the data in a binary format, Office Note 84 (ON84). ON84 is simply formatted NMC grid point data derived from the global reanalysis (NCAR 1995-1996). Grid points of the ON84 data are distributed evenly by latitude and longitude with a 2.5° spacing. This research analyzed the reanalysis data for periods of

1995 and 1996 after the ON84 data was ingested and interpolated to a 45 km Mercator projection grid.

3.2.1. Observation Data. Observation data was obtained from AFCCC throughout the POR for several locations within the region of study (Table 5) to create conditional climatology tables for forecasting low clouds and fog (AFCCC 1995-2001). Observations, both synoptic and METAR, include winds, visibility, present and/or past weather, sky condition, temperature, dewpoint, lowest ceiling, altimeter setting, and accumulated precipitation (3, 6, 12 and 24 hour). However, there were many pitfalls: available stations report a mix of both synoptic and METAR through the POR, synoptic observations usually don't include altimeter setting, accumulated precipitation was not reported in all observations and not for all available days, some observations were missing one or more reportable fields, observations are taken by developing nations in potentially hostile territory, and frequency of the observations were inconsistent with observation times with hours, days, and, occasionally, weeks or months missing. Most stations only reported from 12 to 00 UTC in three-hour increments. The only stations to report on a 24-hour basis and report almost every hour are the most reliable: Leticia, Columbia and Iquitos, Peru. However, both stations are in the Western Amazon Basin. Unfortunately, no station reported hourly in the Columbian Highlands. The most reliable station in the highlands was Villavicencio. All other stations listed in Table 5 reported too sporadically to draw any conclusive results. The only stations that reported accumulated precipitation were Benjamin Constant and Iauarete, Brazil; Iquitos, Peru; Leticia and Villavicencio, Columbia. A station that reports more consistently with fewer time gaps in between observations and with fewer missing reportable data fields is a more

reliable station than one that reports with more gaps in between observations and with more reporting fields missing.

Table 5. Observation stations in region of study (NWSA). Stations are not co-located with actual military installations except Apiay Air Base.

Number in Fig. 19	Station	Country	Latitude (°)	Longitude (°)	Elevation (ft)	Location
1	Apiay Air Base	Columbia	4.15 N	73.50 W	1200	Highlands
2	Benjamin Constant	Brazil	4.38 S	70.03 W	213	Basin
3	Gaviotas	Columbia	4.55 N	70.92 W	548	Highlands
4	Iauarete	Brazil	0.62 N	69.20 W	394	Basin
5	Iquitos	Peru	3.75 S	73.25 W	413	Basin
6	Leticia	Columbia	4.17 S	69.95 W	275	Basin
7	Mitu	Columbia	1.13 N	70.05 W	679	Basin
8	Puerto Asis	Columbia	0.50 N	76.50 W	833	Highlands
9	San José Guaviare	Columbia	2.57 N	72.63 W	509	Highlands
10	Tabatinga Int'l	Brazil	3.67 S	69.67 W	280	Basin
11	Villavicencio	Columbia	4.17 N	73.62 W	1414	Highlands

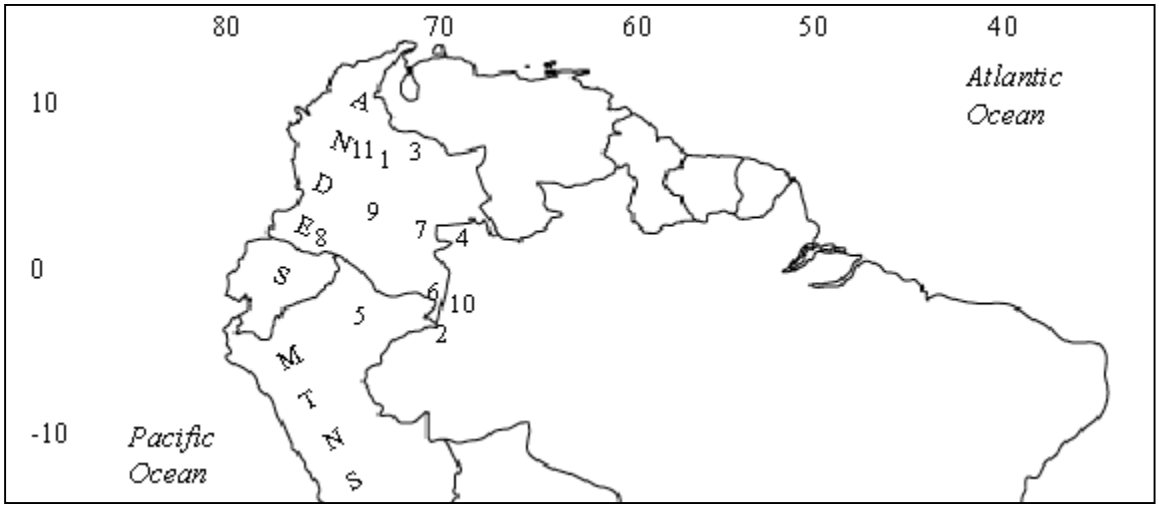

Fig. 19. Geography of observation locations. Numbers correspond to locations in Table 5.

The 25th OWS also provided observations for Apiay Air Base (AB) (17 nm east of Villavicencio) whenever a team deployed there (25th OWS 2001-2002). Observations are full METAR observations complete with accumulated precipitation, remarks and extensive additive data. Because the US military provided the observations, they are assumed to be much more reliable than in-country observations. In addition, the observations were reported hourly whenever the airfield was open (usually daylight hours only). Obviously, since the observation data only encompass 2001 and 2002, this research relied heavily on AFCCC observation data.

The largest pitfall to using any observation data is that the station's localized features can impact observations. This pitfall was impossible to avoid given the region of study encompasses a large flat basin and hilly terrain adjacent to the Andes. Naturally, various localized phenomena such as low clouds, fog, and localized rainfall are very tough to study and predict especially in a data-starved region. Therefore, this research focused on non-localized occurrences of low cloud bases, fog, and heavy rainfall.

3.2. Forecasting Mesoscale Convective Complex Movement in Northern Argentina, Southern Brazil, Paraguay, and Uruguay.

Twenty-two MCC and MCS cases were analyzed to verify Corfidi et al.'s (1996) method of MCC movement for SA. Two of the cases are in Jan 2001 with the remaining from Sep to Dec 2002. Twenty of the 22 cases are MCCs. The other two cases are MCSs that almost obtained MCC status. They were included in this study. The International Desks section of the Hydrometeorological Prediction Center (HPC) at NCEP provided GOES-8 satellite imagery for the 2001 case studies courtesy of Davison (2002) while the Cooperative Institute for Research in the Atmosphere (CIRA) provided GOES-8 satellite imagery for the 2002 cases (CIRA 2002). Additional higher-resolution data from NOAA GOES (NASA 2002) supplemented the full-disk imagery from the HPC and CIRA. This study only utilized three-hourly, channel four IR imagery for the detection of cold cloud tops.

Due to very sporadic and inconsistent upper-air sounding data in the region of study, this research utilized upper-air reanalysis data from FNMOD (FNMOD 2001-2002) for verification of Corfidi's method. The U.S. Navy runs the Navy Operational Global Atmospheric Prediction System (NOGAPS) model to produce reanalysis data twice per day (00 and 12 UTC). The FNMOD stores the archived reanalysis data for access via the Fleet Historical Fields Display System.

IV. Methodology and Results

4.1. Excessive Rainfall, Fog, and Low-Cloud Bases over Columbia, Ecuador, and Northern Peru east of the Andes.

4.1.1. Relationship between Fog and Low-Cloud Bases to Precipitation Occurrences.

4.1.1.1. Methodology. This objective focuses on producing conditional climatology to aid forecasters in predicting low ceilings and visibilities associated with fog and low-cloud bases on the mornings following heavy precipitation events by categorizing each event according to ceilings and visibilities. The standard categories break into the same airfield minimum categories used in the Operational Climatic Data Summary (OCDS) provided by AFCCC (2002). According to the OCDS, the highest probability of dropping below category is during the early to mid morning hours for all locations due to temperatures approaching the dewpoint level. Probabilities of dropping below category should increase following a heavy rainfall event with an increased availability of ground moisture.

After sorting through AFCCC (1995-2001) observation data sets from 1995 to 2001 for four locations: Iquitos, Peru; Benjamin Constant, Brazil; Leticia and Villavicencio, Columbia, accumulated precipitation events greater than 1" in 24 hours were selected. Apiay Air Base (AB), Columbia wasn't selected due to its very limited database. The 24-hour period begins and ends at 06 UTC (approximately midnight local time). Observations without a 12 UTC observation following the precipitation event or 12 UTC observations missing ceiling or visibility fields were excluded. For 24-hour reporting stations, Iquitos and Leticia, randomly selected 11 UTC or 13 UTC

observations replaced all missing or incomplete 12 UTC observations. Furthermore, each heavy precipitation event was subdivided into two events, accumulated rainfall equal or greater than 1" but less than 2" in 24 hours and accumulated rainfall equal or greater than 2" in 24 hours. Finally, summing the amount of occurrences in each category and dividing by the number of occurrences categorizes the data.

4.1.1.2. Results. Appendix A outlines the frequency of ceilings or visibilities falling within an airfield minimum category at and around 12 UTC given one inch or greater precipitation fell within the previous 24-hour period ending at 06 UTC. Data are broken into three tables, one for each location except Villavicencio. The data set includes 141 observations (AFCCC 1995-2001) for Benjamin Constant, 168 observations for Iquitos, 204 observations for Leticia, and 175 observations for Villavicencio. This study includes Benjamin Constant for representation of locations in the Amazon Basin. This was important because of the small population size for nearby Leticia, Columbia. For the locations in the West Amazon Basin, the frequencies generally exceeded the annual climatological mean by 110% to 300%. This makes sense since more available moisture adds to the probability of occurrence of receiving morning fog or low clouds. However, frequencies were lower than the climatological means for Villavicencio as illustrated in Table 6.

Table 6. Climatology of airfield minimum categories for 12 UTC following 1" or greater 24-hour accumulated precipitation for Villavicencio, Columbia.

Ceilings (ft) / Visibility (sm) Categories	Frequency of Occurrence (%)	Annual Climatology for 12 UTC (%)
Less than 3000 / 3	5.7	14.0
Less than 1500 / 3	3.4	7.0
Less than 1000 / 2	1.1	5.0
Less than 300 / 1	< 1.0	1.0
Less than 200 / 0.5	< 1.0	1.0

As previously mentioned, the only hourly reporting stations were Iquitos and Leticia. All other stations reported every three to six hours only from 12 to 00 UTC. The results in Table 6 and the fact that Villavicencio reported every three to six hours raises concerns about the validity of Villavicencio observations. The 25th OWS (2001-2002) deployed observers to disseminate hourly observations sporadically throughout the period for Apiay AB. Although the observational database for Apiay AB is limited, there were enough observations to compare to Villavicencio. Apiay AB is located 17 sm east of Villavicencio and differs only 200 ft in elevation. Although it's reasonable to assume certain localized conditions occur with two stations separated by 17 sm, many similarities should arise with observations from both locations. Differences among 189 observations reported at the same date and time were compiled for available periods during 2001 by calculating the mean error of temperature, visibility, precipitation intensity, and accumulated precipitation. These periods include only times of deployment by the 25th OWS: Jan-Feb, May-Jun, and Aug-Sep 2001.

Mean error calculations showed a reasonable difference between the two stations for most data fields except the ceilings and precipitation intensity. Temperatures and dewpoints differed only by an average of 0.5º to 0.75º C and visibilities merely differed by about 0.25 sm, which are very reasonable for a 17 sm difference. Values were assigned to each value of precipitation intensity (0: no reporting precipitation; 1: drizzle; 2: light rain; 3: moderate rain; 4: heavy rain). Apiay AB registered almost a value of precipitation intensity higher than Villavicencio while ceilings measured almost 3000 feet lower than Villavicencio. This disparity seemed high for the 17 sm difference in a tropical regime. Furthermore, Apiay AB observations reported other height levels of

clouds in its observations while its neighbor station provided little additional information on few and scattered cloud decks. The difference in reporting standards between two sites from different countries (US Air Base vs. Columbian civilian airport) with subjective reporting categories (i.e. ceilings and precipitation intensity) is a likely cause for the difference. Ceilings and precipitation intensities are not completely objective reporting fields like temperature and precipitation accumulation. When a station (e.g. Villavicencio) frequently reports heavy rain with ceilings of 15000 ft, one must certainly question the validity of the observation. Winds and altimeter settings weren't evaluated due to various missing data fields in Villavicencio's observations. To conclude, Villavicencio was excluded from this study and Appendix A.

4.1.2. Determining Ceilings and Visibilities from Precipitation Events.

4.1.2.1. Methodology. The objective of developing climatology to determine ceilings and visibilities given a certain intensity of precipitation occurred is broken into two parts. The first part develops climatology of airfield minimum categories for drizzle, light rain, moderate rain, and heavy rain for three locations where the military operate aircraft: Iquitos, Peru and Leticia and Apiay AB, Columbia. Given Leticia's large database and its close proximity to Benjamin Constant, Benjamin Constant data were excluded from this particular study. In addition, the U.S. military uses Leticia, not Benjamin Constant for landing purposes. This study also excluded Villavicencio because of its questionable ceilings.

After sorting through AFCCC (1995-2001) observation data sets from 1995 to 2001 for Iquitos and Leticia and sporadic deployed data sets from the 25th OWS (2001-2002) for 2001 and 2002, all observations reporting precipitation were selected.

Whenever observations reported multiple precipitation intensities within the same observation, only the dominant precipitation intensity was used for this study. Precipitation was divided into four categories: drizzle, light rain, moderate rain, and heavy rain. Any observation not reporting ceilings and visibilities was excluded. Observations were then categorized into airfield minimum categories using the same process as in section 4.1.1. to determine frequency of occurrences given a certain intensity of precipitation. Table 7 illustrates the number of occurrences for each precipitation intensity and location.

Table 7. Sample sizes for precipitation intensities from 1995-2002.

Location	Total Precip. Obs.	Drizzle Occurrences	Light Rain Occurrences	Moderate Rain Occurrences	Heavy Rain Occurrences
Iquitos, Peru	2417	950	935	434	98
Leticia, Columbia	2630	1118	805	587	120
Apiay Air Base, Columbia	260	26	175	34	25

Part two of this objective develops climatological ranges of ceilings and visibilities for the same locations and observational database as the first part of the objective (Table 7) given a certain intensity of precipitation occurred. The range consists of the middle 80% probability based on percentile plots of each data set. The 10% and 90% percentiles and additional "forecaster tidbits" in section 2 of Appendix B provide the forecaster ranges to forecast ceilings and visibilities in a specific location given a certain precipitation intensity. After separating observations by precipitation intensity

using the same process as the first objective in this section, a histogram and distribution fitted all data within each intensity category for both ceilings and visibilities.

All data sets for ceilings were not evenly distributed. Fig. 20 illustrates the possibility that two or three samples (subsets of populations) could exist within a population. Ceiling data were split into two sets, one for ceilings below 6000 ft (low clouds) and the other for ceilings 6000 to 20,000 ft (mid-level clouds). As seen in Fig. 20, a lack of occurrences falls between 4000 and 7000 ft. Other data sets showed the same distinct differences at and around 6000 ft. Although some data sets show a third sample around 13,000 – 15,000 ft (Fig. 20), the difference from mid to high ceilings are not operationally significant for most military missions.

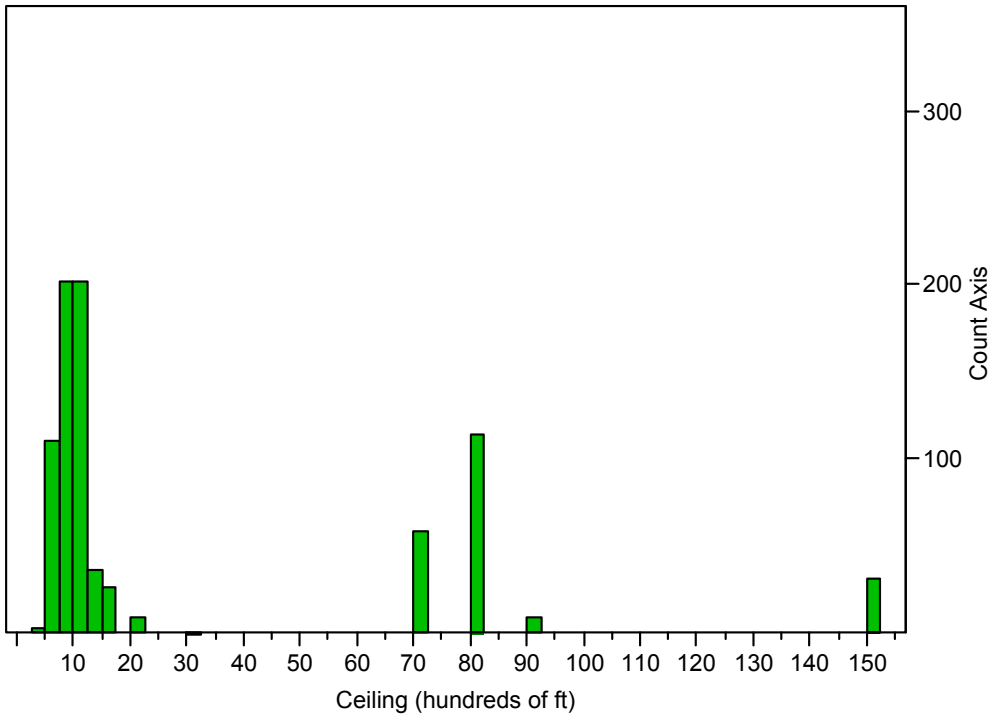

Fig. 20. Illustration of multiple samples within a population of ceilings associated with light rain at Leticia, Columbia (interval 250 ft.).

Administering a t-test verified the two sample sets within the population were indeed different. This research chose the t-test over the z-test because the population variance was unknown. Instead, the t-test uses the variance as an approximation of the population variance to assume normality. The p-level, calculated from the t-test, determines whether the null hypothesis is rejected or not. If the p-value is less than an acceptable level of significance (LOS) ($\alpha = 0.05$ or $0.05/2$ for a two-tailed t-test), then the t-test leads the researcher in rejecting the null hypothesis that the mean of both samples are approximately equal (Devore 2000). This research followed traditional scientific researchers in using 0.05 for an acceptable LOS (Devore 2000). P-values for all ceiling data sets for all three locations were 0.0001, which fails to exceed the LOS of 0.05/2. The null hypothesis was easily rejected; therefore, this study treated all ceiling data sets as two separate populations.

Normal quantile plots tested for normality for each data set. Figs. 21 through 24 illustrate a couple of examples for normality tests. For normality, the data should fit within the 95% confidence intervals. Fig. 22 shows an example of a population not meeting normality. The lognormal distribution, a distribution that computes the natural log of the data to best fit a normal distribution, best represents the population in Figure 21 over similar distributions like the gamma and beta distributions. Although the normality distribution in Fig. 23 is far from a perfect fit, the quantile plot in Fig. 24 is sufficient to use to assume normality for this particular distribution. Fig. 25 depicts an example where no distribution appropriately fits the data. In many cases, including Fig. 25, empirical methods were developed to best fit the data. Tables 8 through 10 lists the distributions used for each population. As seen, the empirical technique was the only

suitable choice in most data sets, especially smaller populations such as Apiay AB and populations that were too far spread for any non-empirical distribution.

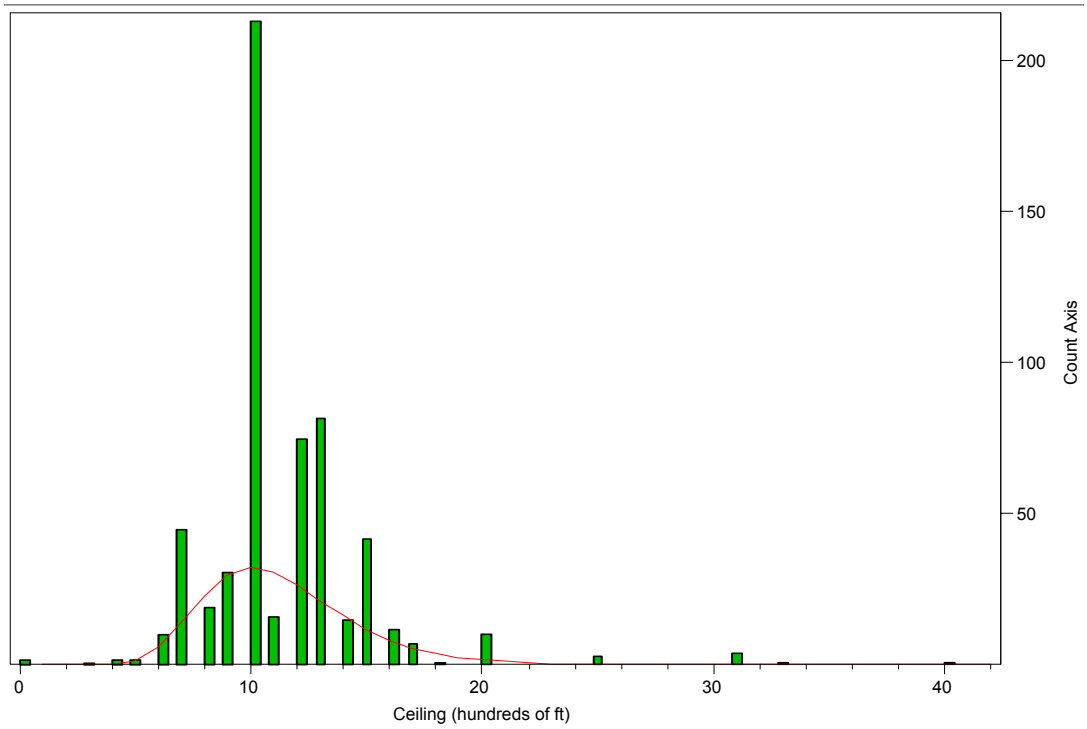

Fig. 21. Lower range of ceilings associated with drizzle for Iquitos, Peru (interval 100 ft.). Curve represents the fitted lognormal distribution.

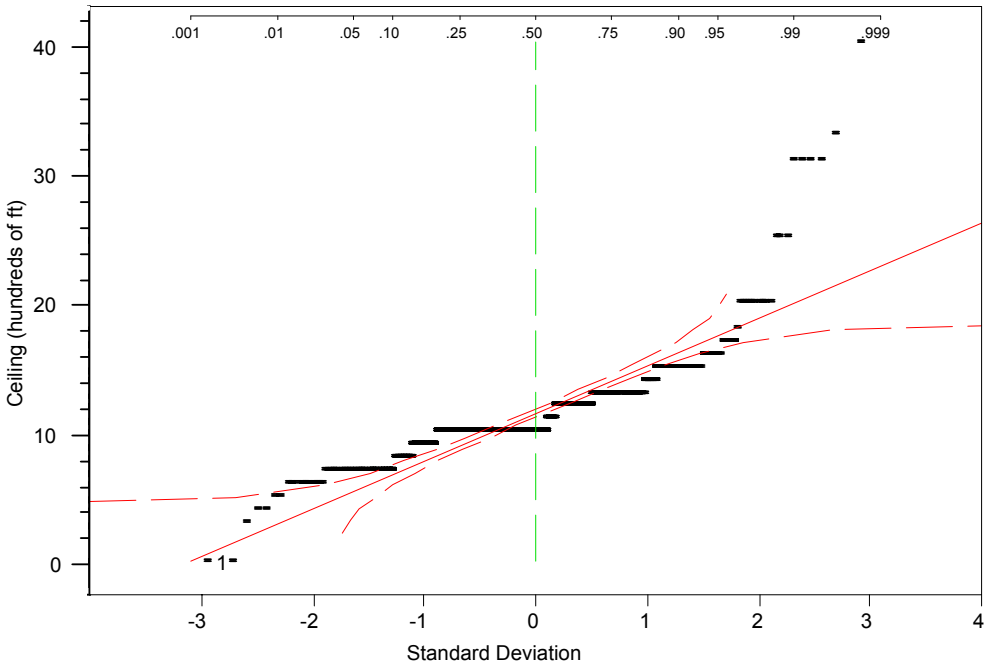

Fig. 22. Normal quantile plot for lower range of ceilings associated with drizzle for Iquitos, Peru. Straight line and curved lines represent the normal line and 95% confidence intervals respectively. Vertical dashed line represents the median while the top axis represents the cumulative distribution function.

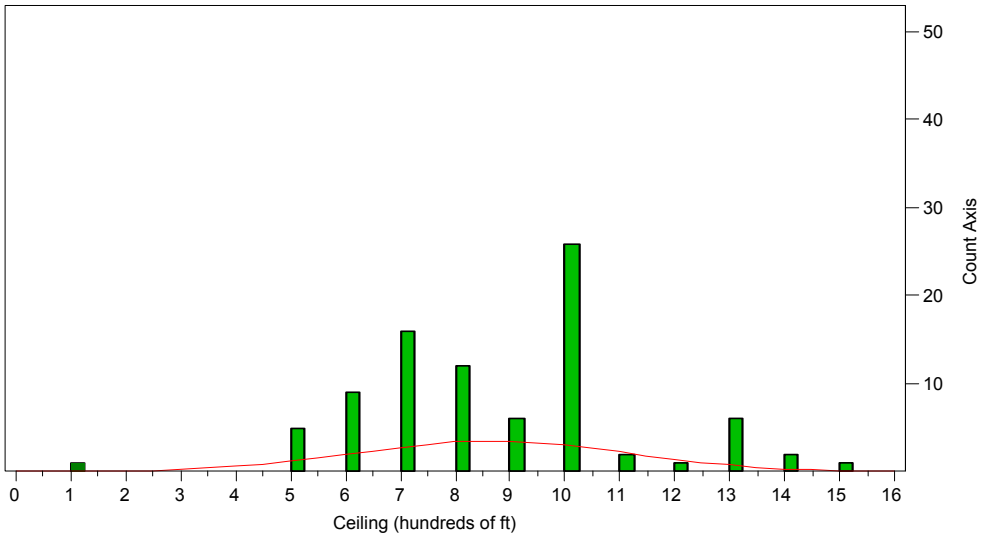

Fig. 23. Lower range of ceilings associated with heavy rain for Iquitos, Peru (interval 50 ft.) Curved line represents the fitted normal distribution.

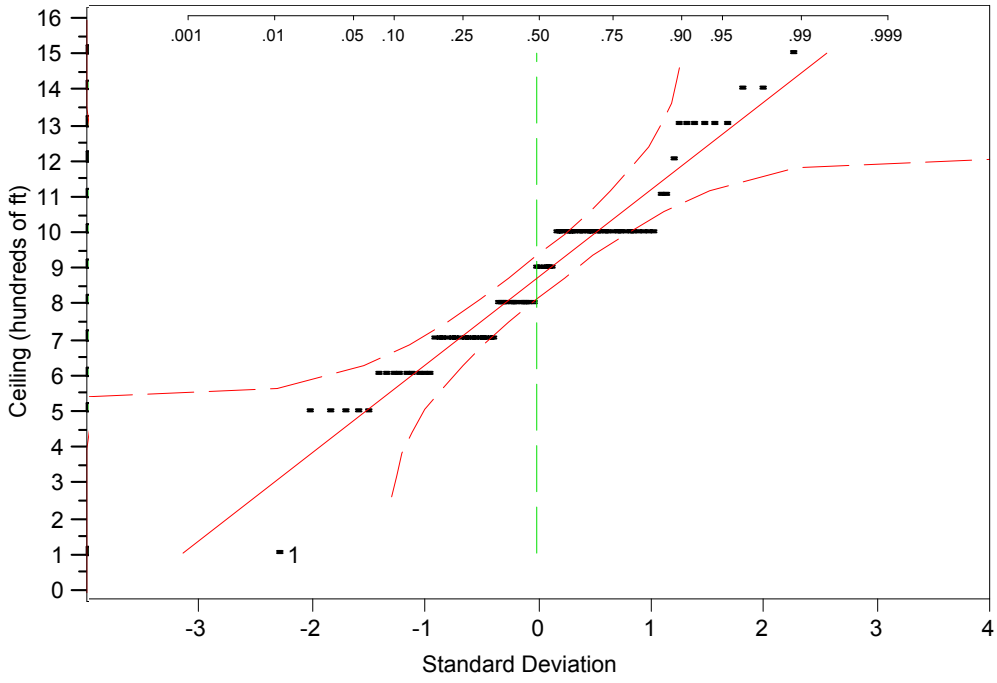

Fig. 24. Normal quantile plot for lower range of ceilings associated with heavy rain for Iquitos, Peru. Straight line and curved lines represent the normal line and 95% confidence intervals respectively. Vertical dashed line represents the median while the top axis represents the cumulative distribution function.

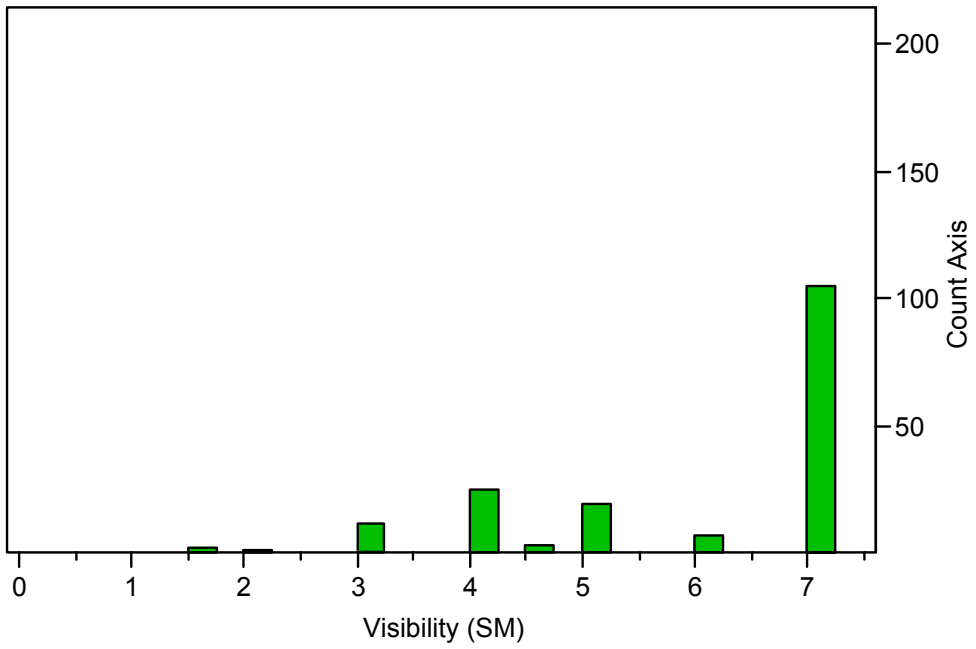

Fig. 25. Visibilities associated with light rain for Apiay AB, Columbia (interval ½ sm).

Table 8. Sample Sizes and Distribution Methods for Iquitos, Peru.

Precipitation Intensity	Ceiling (CIG) Range or Visibility (VIS)	Sample Size	Range of Values CIG (ft) or VIS (sm)	*Distribution or Method Applied*
Drizzle	Lower Range CIG	594	0 – 4000	Lognormal
Drizzle	Upper Range CIG	356	5000 – 15,000	Empirical
Drizzle	VIS	950	1/2 – 7	Empirical
Light Rain	Lower Range CIG	692	0 – 3100	Normal
Light Rain	Upper Range CIG	243	7000 – 15,000	Empirical
Light Rain	VIS	935	5/8 – 7	Empirical
Moderate Rain	Lower Range CIG	370	300 – 2000	Normal
Moderate Rain	Upper Range CIG	64	7000 – 10,000	Empirical
Moderate Rain	VIS	434	1/16 – 7	Empirical
Heavy Rain	Lower Range CIG	87	100 – 1500	Normal
Heavy Rain	Upper Range CIG	11	7000 – 8000	Empirical
Heavy Rain	VIS	98	0 – 7	Empirical

Table 9. Sample sizes and distribution methods for Leticia, Columbia.

Precipitation Intensity	Ceiling (CIG) Range or Visibility (VIS)	Sample Size	Range of Values CIG (ft) or VIS (sm)	*Distribution or Method Applied*
Drizzle	Lower Range CIG	772	500 – 4000	Lognormal
Drizzle	Upper Range CIG	346	6000 – 20,000	Empirical
Drizzle	VIS	1118	3/8 – 7	Empirical
Light Rain	Lower Range CIG	592	400 – 3100	Normal
Light Rain	Upper Range CIG	213	7000 – 15,000	Empirical
Light Rain	VIS	805	1/4 – 7	Empirical
Moderate Rain	Lower Range CIG	510	100 – 5000	Lognormal
Moderate Rain	Upper Range CIG	77	6000 – 15,000	Empirical
Moderate Rain	VIS	587	1/4 – 7	Empirical
Heavy Rain	Lower Range CIG	115	400 – 1700	Normal
Heavy Rain	Upper Range CIG	5	8000 – 8000	Empirical
Heavy Rain	VIS	120	1/16 – 7	Empirical

Table 10. Sample sizes and distribution methods for Apiay AB, Columbia.

Precipitation Intensity	Ceiling (CIG) Range or Visibility (VIS)	Sample Size	Range of Values CIG (ft) or VIS (sm)	*Distribution or Method Applied*
Drizzle	Lower Range CIG	10	2000 – 5500	Empirical
Drizzle	Upper Range CIG	16	6500 – 13,000	Empirical
Drizzle	VIS	26	3 – 7	Empirical
Light Rain	Lower Range CIG	123	500 – 5500	Normal
Light Rain	Upper Range CIG	52	6000 – 14,000	Empirical
Light Rain	VIS	175	1 1/2 – 7	Empirical
Moderate Rain	CIG	34	400 – 5500	Normal
Moderate Rain	VIS	34	3/4 – 7	Empirical
Heavy Rain	CIG	25	200 – 4900	Normal
Heavy Rain	VIS	25	1/2 – 7	Empirical

The basic empirical technique provides a distribution-free method to determine the probability of occurrence, $F(t_i)$, by dividing the number of observations observed at a certain point, i, by the total number of data points within the population, n (Ebeling 1997):

$$F(t_i) = i/(n+1) \qquad (1)$$

Given the probability of occurrence (e.g. $F(t_i)$ = 10% and 90%) and the n-value, this method determines i, the rank of a value with respect to the total number of observations. After sorting and ranking data, the i value directly relates to an actual ceiling or visibility value. This ceiling or visibility value then represents the percentile used, $F(t_i)$ (Ebeling 1997).

4.1.2.2. Results. The results for the first part of this objective are presented in section 1 of Appendix B. Section 1 of Appendix B outlines the frequency of occurrences of ceilings or visibilities falling within an airfield minimum category given a certain precipitation intensity is forecast to occur. Data for the first part of this objective are

broken into three tables with each table corresponding to Iquitos, Leticia, and Apiay AB. Frequencies of occurrences within a category naturally increased with the intensity of precipitation as ceilings and visibilities lower. Probabilities increased more for the basin locations than for Apiay AB. Localized differences, especially differences in ground moisture, between the basin locations and the highlands where Apiay AB sits likely cause the differences. Although Apiay AB lacks a significant database, its results should steer the forecaster in the proper direction.

The results for the second part of this objective are presented in section 2 of Appendix B. Section 2 of Appendix B summarizes the frequency of ceilings and visibilities falling below a certain ceiling or visibility for three locations: Iquitos, Leticia, and Apiay AB. The results are broken into 24 tables, one for each population. As expected, all percentiles generally yielded lower ceilings and visibilities with more intense precipitation.

All percentages derived from a non-empirical technique were verified using empirical methods. Empirical method verification values matched all normal distribution values and were within 60 ft of lognormal distribution values. Since observers report ceilings in hundreds of feet, 60 ft is within one reporting interval (100 ft). Therefore, the empirical verification validates the usefulness of lognormal percentile results.

The percentiles used correspond to the specific distribution used in each population. The 10% and 90% percentiles for the lower range of ceilings generate a tight fit for Iquitos and Leticia but a much wider range for Apiay AB due to its smaller population sizes. Due to enormous percentile spreads and operational insignificance, 10% and 90% percentiles were not generated for the upper range of ceilings. The 10%

and 90% percentile spread for visibilities is quite large due to large variability in the visibility. No relationship can explain the large spread in visibilities. Due to the extremely weak correlations (not shown) found between low visibilities and low ceilings and between high visibilities and high ceilings, both variables were treated independently in this research.

Despite visibilities and ceilings lowering with more intense rainfall, there were a few exceptions. Moderate and heavy rain populations produced outlier visibilities around 7 sm and ceilings around 8000 ft. However, these outliers generally lie above the 97.5% percentile; therefore, they do not significantly impact the 10% to 90% percentile groups.

Forecasters must first determine which range, lower or upper, ceilings will occur in before predicting the ceiling. The lower range of ceilings represent ceilings less than 6000 ft and the upper range of ceilings represent ceilings 6000 – 20,000 ft. Section 2 of Appendix B also outlines the frequency of occurrence in both categories. Probabilities of falling into the lower range of ceilings increased with increased precipitation intensity. Apiay AB registered no upper ceiling range occurrences for moderate to heavy rain. The problem now arises of what range to forecast ceilings in.

25th OWS (2001-2002) observers deployed to Apiay AB disseminated Apiay AB observations with copious information. The additional data yielded invaluable information about the placement of storms with respect to the point of observation. Mid-level ceilings typically occur on the stratified edges and trailing sectors of convective storms instead of the center or main updraft region of the convective cloud elements as illustrated in Fig. 4 (Section 2.1.1.). Observations reporting vicinity showers (VCSH), vicinity thunderstorms (VCTS), cumulonimbus (CB), and towering cumulus (TCU)

within one hour of occurrence of light rain or drizzle were investigated. CB and TCU were included since observers typically report these clouds only when they can see the vertical extent of CB or TCU clouds. To accurately view and report CB or TCU, the clouds should not typically lie overhead; therefore, the possibility exists that their associated mid-level decks could produce light precipitation. Moderate and heavy rain reports weren't examined due to lack of any reports in the upper range of ceilings. This makes sense since the main convective element should lie overhead with almost all reports of moderate and heavy rain. This study also included any report of CB or distant TS in the remark section of the observation. Finally, this study used reports of very light precipitation (PCPN VRY LGT) in the remark section whenever observers witness light rain or drizzle.

The vast majority of mid-level cloud observances did occur simultaneously or within one hour of the conditions described above (i.e. VCTS, VCSH, CB, TCU, PCPN VRY LGT, and distant TS). Ten out of 16 of the upper ceiling range of drizzle reports and 24 out of 52 of the upper ceiling range of light rain reports occurred simultaneously with or within one hour of the same conditions described above. However, within these data, all 8 ceiling reports of 8500 ft or higher with drizzle and 17 out of 20 ceiling reports of 10,000 ft or higher with light rain were associated with the conditions described above. Hardly any reports of these conditions were associated with ceilings less than 6000 ft. Although the study was limited in data and requires more research, these findings depict a strong indication that mid-level ceilings are associated with edges of convective storms and very light precipitation.

Unfortunately, civilian observation stations in NWSA don't report additive observation data or complete observations on a consistent basis; therefore, no concrete relationship arises. However, all locations in Northern SA lie within the tropics and experience similar climate conditions: moist, unstable, convective tropical systems; therefore, this study safely assumed that the same reasoning for separating the lower and upper ranges of ceilings for Apiay AB also applies to other locations within the AOR.

In addition, the subjectiveness of reporting precipitation intensity arises even among USAF observers, let alone foreign country observers. For example, Air Force Manual 15-111 specifies light rain as several drops only partially wetting the ground to a light steady-falling rainfall wetting the ground (DAF 1998). The disparity in precipitation intensity reporting might also explain differences among ceiling heights, for ceilings will typically lower more for a steady fall versus sprinkles.

This study utilized percentiles instead of standard deviations due to high variability and lack of normal distributions in the samples. This study also used percentiles instead of confidence intervals because the confidence intervals (not shown) produced unrealistic results for many samples. In addition, percentiles produce an easy to interpret understanding of the conditional climatology for the layman forecaster versus confidence intervals. Forecasters must apply caution with Appendix B. Length of precipitation event, different meteorological patterns, and localized terrain differences likely account for some of the variability among the populations.

4.1.3. Forecasting Excessive Rainfall Events.

4.1.3.1. Methodology. This objective develops guidelines for forecasting excessive rainfall of approximately 6" or greater within 24 hours over NWSA east of the Andes. Although various meteorological factors such as moisture availability, thermal instability, and triggering mechanisms are necessary to produce copious quantities of rain, this research only focused on two necessary triggering mechanisms: divergence and vertical velocities. In addition to analyzing divergence and vertical velocities, specific precursory features seen on isobaric wind vector analysis charts could warn forecasters of impeding heavy rainfall. The guidelines include precursors seen on wind vector analyses, divergence, and vertical velocity value charts associated with excessive rainfall. Due to data availability, this study only utilized 24-hour accumulated precipitation data from AFCCC (1995-2001) surface observation data from the 1995 and 1996 PORs for three locations: Benjamin Constant and Iauarete, Brazil and Villavicencio, Columbia. Fortunately, all three stations are spread throughout the AOR covering both the Western Amazon Basin and Columbian Highlands.

Questions about Villavicencio's observational validity arose again with precipitation amounts. Precipitation values were compared between 189 observations in 2001 between Villavicencio and Apiay AB to determine the validity of Villavicencio precipitation data. Only three events registered 1" or greater in both locations. With each event, Apiay AB preceded its neighbor station with heavy rainfall reports by three hours. This makes sense given both stations only report rainfall amounts every three hours and easterly flow drives storms westward. Although there isn't enough data to accurately correlate the amounts between the two stations, both stations reporting

amounts of at least 1" within three hours of each other and the fact that precipitation accumulation is an objective reporting field (unlike ceilings and precipitation intensity), yielded enough confidence to utilize Villavicencio accumulated precipitation reports for this study.

After isolating 24-hour precipitation amounts for days with approximately 6" or greater (smallest value used was 5.76") for the desired locations, values of divergence and vertical velocities were found from interpolating the reanalysis data (ON84 data from the GDAS model) onto a 45 km Mercator projection and analyzing it. The reanalysis data from NCAR (1995-1996), originating from the former National Meteorological Center (NMC) (now called NCEP), was developed from the GDAS model. The GDAS is the same system that NMC ran for the Aviation model and Medium Range Forecast model. In 1995 and 1996, GDAS produced a T62 resolution model with 28 vertical layers (Shih 2002). This resolution corresponds to the model resolving waves no smaller than roughly 350 nm; therefore, features smaller than the model resolution (i.e. meso-beta and small meso-alpha scale features) may yield erroneous values. Given the great lack of upper-air network over SA, greater resolution may not necessarily resolve smaller features anyway.

Verification of storm size from DMSP satellite imagery (NGDC 2002) was necessary before ingesting the ON84 data onto a 45 km Mercator projection for specific dates. Due to the GDAS model's resolution restraints, any system not at least 350 nm in width or length was subjectively excluded from the study. This reduced the number of available events with 6" or more in 24-hours by roughly 40%. In other words,

approximately 40% of the 6" events were too small in size and were excluded from this study.

TERRAIN and REGRID, vital programs of the Fifth Generation Pennsylvania State University/NCAR Mesoscale Model (MM5), ingests and interpolates reanalysis data. The TERRAIN program interpolates latitude, longitude, and terrain onto an operator specified mesoscale map. In this research, TERRAIN mapped a Mercator projection encompassing all of SA north of 12º S and west of 55º W with a spatial resolution of 45 km (different from the GDAS 350 nm resolution). The REGRID program consists of two parts, pregrid and regridder. Pregrid inputted the NMC ON84 reanalysis data while regridder interpolated the data onto the specified MM5 TERRAIN grid. Regridder only ran data for the parameters, levels, and times specified in a file. Both REGRID and TERRAIN programs were run using a UNIX Operating System on Solaris 8.

Various charts were displayed at several isobaric levels at both 00 UTC and 12 UTC for days reporting excessive 24-hour accumulated precipitation. They include: divergence value charts at 850, 700, 600, 500, 400, and 300 mb; vertical velocity charts at 700, 500, and 300 mb; wind vector analysis charts at 1000, 850, 700, 500, 400, and 300 mb; and cross sections of isotach analysis from the surface to 300 mb from 10º N to 10º S at 70º W and 55º W. The divergence charts displayed values with intervals of 0.25×10^{-5} s^{-1} while vertical velocity charts displayed values with intervals of 0.5 cm s^{-1}.

Maximum values of divergence and vertical velocities corresponding to the tropical mesoscale convective system (MCS) were collected from the reanalysis data charts and recorded for both 00 UTC and 12 UTC. To partially account for errors from

low spatial resolution and analysis, a range of maximum values were documented. The maximum ranges recorded were a range of 0.25 x 10^{-5} s^{-1} for divergence and 1 cm s^{-1} for vertical velocities. The recording process required careful analysis of satellite imagery of the system to ensure the MCS corresponded to the areas of maximum divergence and vertical velocity values. In addition, the MCS and maximum range of values crossed the station prior to the 12 UTC observation of 24-hour accumulated precipitation to ensure the values recorded pertain to the same MCS. Occasionally, this process required further subjective analysis of both the reanalysis and satellite imagery if the maximum range of values crossed the surface observation location prior to or following the time of reanalysis (00 UTC and 12 UTC). The time (either 00 UTC or 12 UTC) that displayed the highest values was also noted.

In addition to divergence and vertical velocities, wind vector analysis charts and cross sections portrayed various precursory mesoscale and synoptic scale features associated with tropical systems in Northern SA. The charts yielded important information about common features (i.e. convergence zones, mesoscale circulations, waves in upper-level easterly flow, etc.) that lead to significant convergence and divergence values. Since forecasters can detect certain features on analyses and model charts, a summary of the precursory features would prove invaluable to the forecaster predicting heavy rainfall events.

To validate any results, a comparison to non-heavy rainfall events was necessary. A non-heavy rainfall event in the tropics is defined here as an event less than 2" in 24-hours. For comparison purposes, only wet-season 24-hour precipitation events of 1-2"

from the same locations and POR were utilized. The process of obtaining values was similar to the process for 6" events with one notable exception.

The problem of low spatial resolution arose again with 1-2" events. As with the 6" events, only systems that were at least 350 nm wide or long were studied. Since smaller-scale systems can easily produce lighter amounts, a criterion for comparison needed to be established. Many large-scale systems greater than 350 nm can indeed produce only 1-2" events, especially if they possess weaker atmospheric dynamics or are accompanied by a much stronger system that does not directly progress over the surface observational location but around the station. In this scenario, divergence and vertical velocity values were only gathered from the sector of the storm affecting the location of observation. In all cases, the maximum values associated with the storms missed the surface observation site. This provided evidence those 1-2" rainfall events either occurred with small-scale systems or on the periphery of larger-scale systems.

Finally, t-tests were administered to both 1-2" event populations and 6" or greater event populations to verify any significant differences between the two. The process and level of significance used was the same as the process described in Section 4.1.2.2. Before performing the t-tests, a test for normality was necessary to determine if the populations fit a normal distribution. This was necessary to establish a usable mean and standard deviation for all populations of divergence and vertical velocities for both 1-2" events and 6" or greater events.

4.1.3.2. Results. Results for this section are presented in Tables 11 and 12 and are summarized in Table C4 in Appendix C. Appendix C provides forecaster guidance on predicting the dynamical precursors to excessive rainfall events. Results are broken

into two areas: north of the Equator and south of the Equator. Villavicencio and Iauarete represent locations north of the Equator while Benjamin Constant represents locations south of the Equator. Both locations were treated separately from each other mainly due to different wet seasons and the slight difference in dynamics between storms forming in the two locations (discussed later in this section).

A t-test to determine a significant difference between the 6" events and 1-2" events resulted in rejecting the null hypothesis of treating the two populations as the same. P-values for all divergence and vertical velocity categories were 0.0001 or less, less than this study's LOS for a two-tailed t-test, 0.05/2 (α=0.05).

Tables 11 and 12 outline the results for 6" events and 1-2" events respectively. Since normal quantile plots for all populations resulted in treating the populations as having a relatively normal distribution, averages and standard deviations were computed for all divergence and vertical velocity populations. Fig. 26 illustrates an example of one population noticeably meeting normality. As demonstrated in both tables, separating the two locations helped to lower the standard deviations for each location. Table 12 depicts the difference between 6" and 1-2" rainfall events. Since 1-2" events produced divergence and vertical velocity values only about 30-50% of those for 6" events, it's clearly evident that stronger divergence and vertical velocities significantly contribute to the dynamics of excessive rainfall events.

Table 11. Mean ranges and standard deviations (std. dev.) of divergence (DIV) and upward vertical velocities (UVV) for excessive rainfall events (approximately 6" or greater in 24 hrs). Upper-level DIV represents the level of strongest divergence.

Locations north of the Equator (based on 22 occurrences)				
	Lower range mean	**Lower range std. dev.**	**Upper range mean**	**Upper range std. dev.**
850 mb DIV (10^{-5} s^{-1})	-1.67	0.49	-1.94	0.52
700 mb DIV (10^{-5} s^{-1})	-1.43	0.47	-1.68	0.47
Upper-level DIV (10^{-5} s^{-1})	1.63	0.39	1.88	0.39
700 mb UVV (cm s^{-1})	2.86	0.77	3.86	0.77
500 mb UVV (cm s^{-1})	3.09	1.23	4.09	1.23
Locations south of the Equator (based on 5 occurrences)				
	Lower range mean	**Lower range std. dev.**	**Upper range mean**	**Upper range std. dev.**
850 mb DIV (10^{-5} s^{-1})	-1.25	0.43	-1.50	0.43
700 mb DIV (10^{-5} s^{-1})	-2.00	0.59	-2.25	0.59
Upper-level DIV (10^{-5} s^{-1})	1.90	0.65	2.15	0.65
700 mb UVV (cm s^{-1})	3.40	1.67	4.40	1.67
500 mb UVV (cm s^{-1})	2.60	1.14	3.60	1.14
All locations (based on 27 occurrences)				
	Lower range mean	**Lower range std. dev.**	**Upper range mean**	**Upper range std. dev.**
850 mb DIV (10^{-5} s^{-1})	-1.59	0.50	-1.86	0.53
700 mb DIV (10^{-5} s^{-1})	-1.54	0.53	-1.79	0.53
Upper-level DIV (10^{-5} s^{-1})	1.68	0.45	1.93	0.45
700 mb UVV (cm s^{-1})	2.96	0.98	3.96	0.98
500 mb UVV (cm s^{-1})	3.00	1.21	4.00	1.21

Table 12. Mean ranges and standard deviations (std. dev.) of divergence (DIV) and upward vertical velocities (UVV) for 1-2" in 24-hours rainfall events. Upper-level DIV represents the level of strongest divergence. Percent of lower and upper range means are the percent of 6" or greater event lower and upper range means.

Locations north of the Equator (based on 31 occurrences)						
	Lower range mean	**Lower range std. dev.**	**% of lower range mean of ≥ 6" events**	**Upper range mean**	**Upper range std. dev.**	**% of upper range mean of ≥ 6"events**
850 mb DIV (10^{-5} s^{-1})	-0.76	0.31	45%	-1.01	0.31	52%
700 mb DIV (10^{-5} s^{-1})	-0.71	0.33	49%	-0.95	0.33	56%
Upper-level DIV (10^{-5} s^{-1})	0.94	0.30	57%	1.19	0.30	63%
700 mb UVV (cm s^{-1})	1.03	0.60	36%	2.03	0.60	52%
500 mb UVV (cm s^{-1})	1.54	0.92	50%	2.55	0.92	62%
Locations south of the Equator (based on 13 occurrences)						
	Lower range mean	**Lower range std. dev.**	**% of lower range mean of ≥ 6" events**	**Upper range mean**	**Upper range std. dev.**	**% of upper range mean of ≥ 6"events**
850 mb DIV (10^{-5} s^{-1})	-0.46	0.22	37%	-0.71	0.22	47%
700 mb DIV (10^{-5} s^{-1})	-0.63	0.53	32%	-0.85	0.65	38%
Upper-level DIV (10^{-5} s^{-1})	0.73	0.30	38%	0.98	0.30	46%
700 mb UVV (cm s^{-1})	0.85	0.37	25%	1.85	0.37	42%
500 mb UVV (cm s^{-1})	0.69	0.63	27%	1.69	0.63	47%
All locations (based on 44 occurrences)						
	Lower range mean	**Lower range std. dev.**	**% of lower range mean of ≥ 6" events**	**Upper range mean**	**Upper range std. dev.**	**% of upper range mean of ≥ 6"events**
850 mb DIV (10^{-5} s^{-1})	-0.67	0.32	42%	-0.92	0.32	49%
700 mb DIV (10^{-5} s^{-1})	-0.68	0.39	44%	-0.92	0.44	52%
Upper-level DIV (10^{-5} s^{-1})	0.88	0.31	52%	1.13	0.31	58%
700 mb UVV (cm s^{-1})	0.98	0.55	33%	1.98	0.55	50%
500 mb UVV (cm s^{-1})	1.30	0.93	43%	2.30	0.93	57%

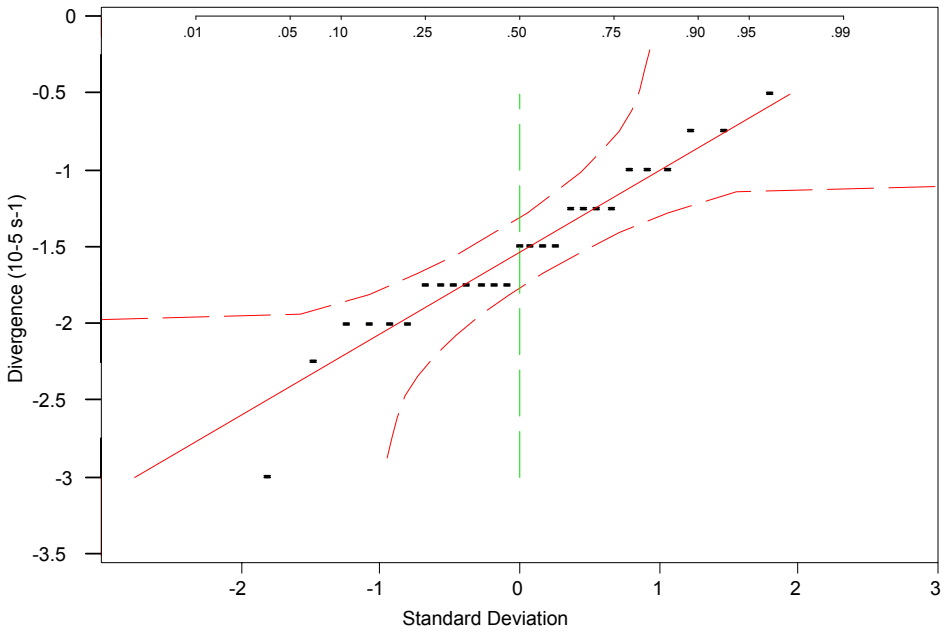

Fig. 26. Example of a divergence population meeting normality. Population is for the lower range values for 700 mb divergence for 6" or greater rainfall events for all locations. Straight line and curved lines represent the normal line and 95% confidence intervals respectively. Vertical dashed line represents the median while the top axis represents the cumulative distribution function.

In addition to divergence values produced, the magnitude of differences from the strongest level of divergence and convergence can aid the forecaster in determining to forecast excessive rainfall or not. Divergence differences, as explained in Appendix C, between the two levels produced an average value of approximately 4 x 10^{-5} s^{-1} for both locations for 6" events with a standard deviation of 0.54 x 10^{-5} s^{-1} for the north and 0.94 x 10^{-5} s^{-1} for the south. One outlier from the southern location was primarily responsible for the higher standard deviation. As expected, the 1-2" events produced a divergence difference value that was half that of the 6" events with a standard deviation of 0.40 to 0.45 x 10^{-5} s^{-1} for both locations. This, however, raised concern about what level to use for maximum convergence and divergence values.

The level of strongest divergence and convergence varies among tropical systems and locations. In both locations, both low-levels displayed very similar convergence values. As shown in Tables 11 and 12, locations south of the Equator slightly favor 700 mb over 850 mb while the opposite is true for the northern locations. Gamache and Houze (1982) and Garstang et al. (1994) also found convergence values strongest from 850 to 700 mb. Slight differences between the 700 and 850 mb levels are difficult to explain; however, the influences of low-level subtropical high placement, time of year, and trade wind inversion heights may account for the differences. The upper-level differences are, however, more defined.

The 400 mb level is a common level to produce the strongest outflow or divergence values. 400 mb was the level of strongest divergence values for almost two-thirds of the 6" events. 300 and 500 mb proved the level of strongest divergence in roughly 20% and 15% of the total 6" events respectively. The 1-2" events exemplified a different result. Only half the 1-2" events had strongest divergence values at 400 mb while 500 mb contained the strongest divergence values for over 40% of the events and 300 mb for less than 10% of the events. The difference is likely related to the extent of upward growth. Since weaker storms usually exhibit less vertical extent, the level of divergence is naturally lower while the level of outflow is higher with increased growth and intensity of storms. Research by Gamache and Houze (1982) and Garstang et al. (1994) also found uppermost divergence values from 400 to 300 mb for powerful tropical systems in SA. In addition, they found 600 mb the level of non-divergence, which matches findings in this research.

Vertical velocities, however, showed no bias toward either 700 or 500 mb. Both levels proved equally as strong for vertical velocities. Vertical velocity values for 850 mb

and levels above 500 mb, not presented here, were actually lower than upward vertical velocity values for 700 and 500 mb. Gamache and Houze (1982) and Garstang et al. (1994) additionally found vertical velocities strongest from 700 to 500 mb.

While the levels of strongest convergence, divergence, and vertical velocity values matched those found in previous research, the magnitudes did not. Gamache and Houze (1982) and Garstang et al. (1994) discovered values more than double of those found in this study. The difference may be due to lack of spatial resolution in the reanalysis data fields. Gamache and Houze (1982) and Garstang et al. (1994) exploited insitu and remote sensor measurements with Amazon Basin MCSs such as tropical squall lines to measure various parameters to include divergence and vertical velocities. They were able to separate the leading convective elements of the MCS, which yielded values for divergence and vertical velocities that were at least double those found in this study, from the anvil sector of the MCS. The low resolution reanalyses, however, cannot distinguish between leading convective elements and trailing stratified anvils. Instead, the reanalyses interpolates divergence and vertical velocity values smoothed over a larger region; therefore, generating lower values of divergence and vertical velocity.

Figs. 27 through 34 demonstrate a classic tropical squall line event generating 10" of rain in 24 hours over Iauarete, Brazil (0.6º N 69.2º W). Vector analysis from Figs. 28 and 30 line up with the negative divergence values (convergence) corresponding to Figs. 27 and 29 respectively. Fig. 28 illustrates a distinct maximum of directional and speed convergence over Iauarete. Air from both sides of the Equator tends to merge close to the Equator. This convergence near the Equator is likely the NET. Both directional and speed divergence at

400 mb over Eastern Columbia and Northwest Brazil (Fig. 32) correspond to the same maximum areas of divergence presented in Fig. 31.

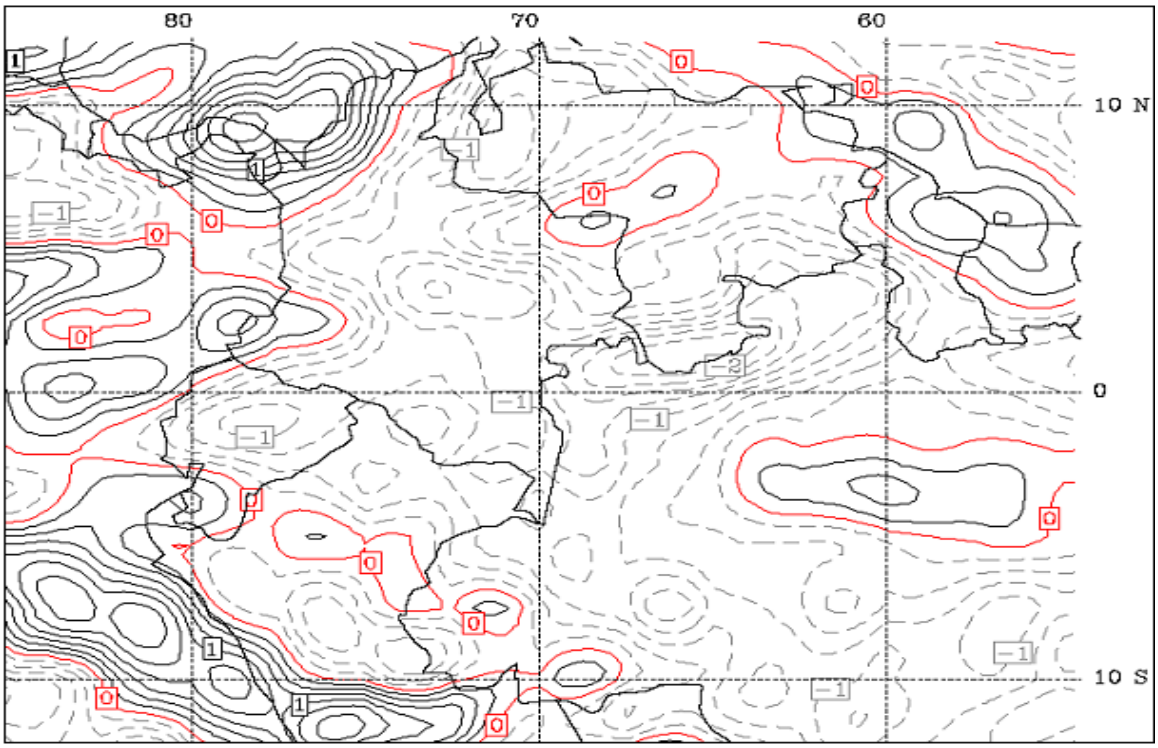

Fig. 27. 850 mb divergence (10^{-5} s^{-1}) for 00 UTC on 18 May 95. Negative values are dashed.

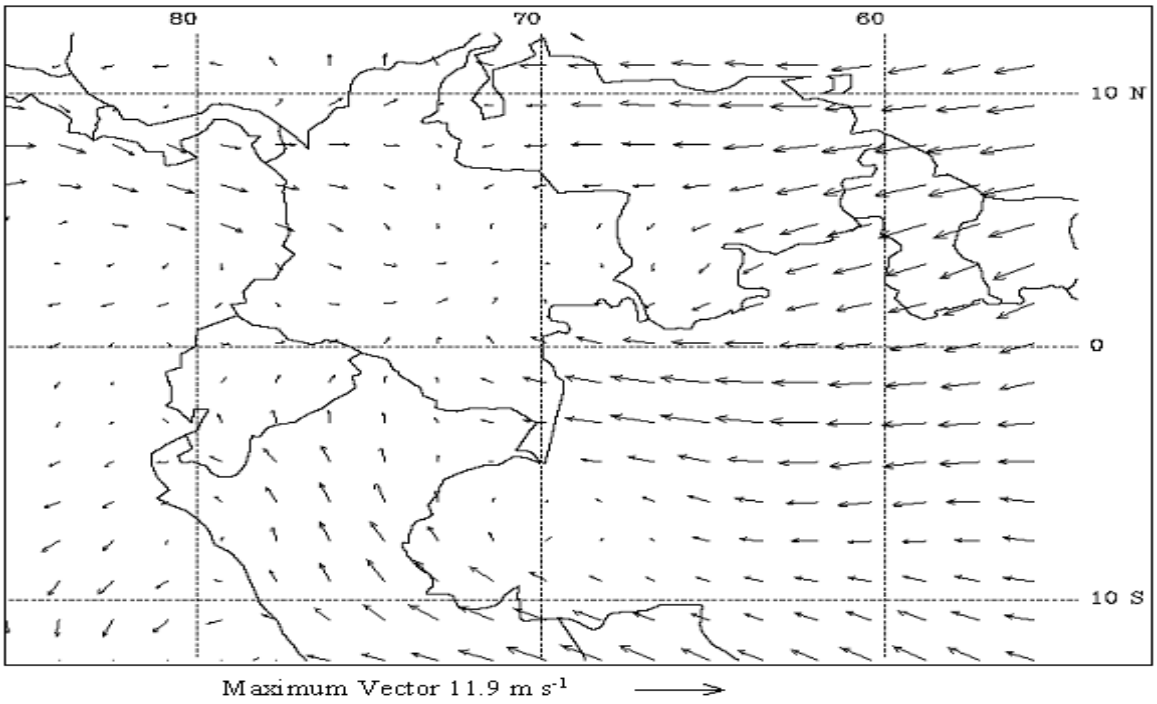

Fig. 28. 850 mb vector analysis for 00 UTC on 18 May 95.

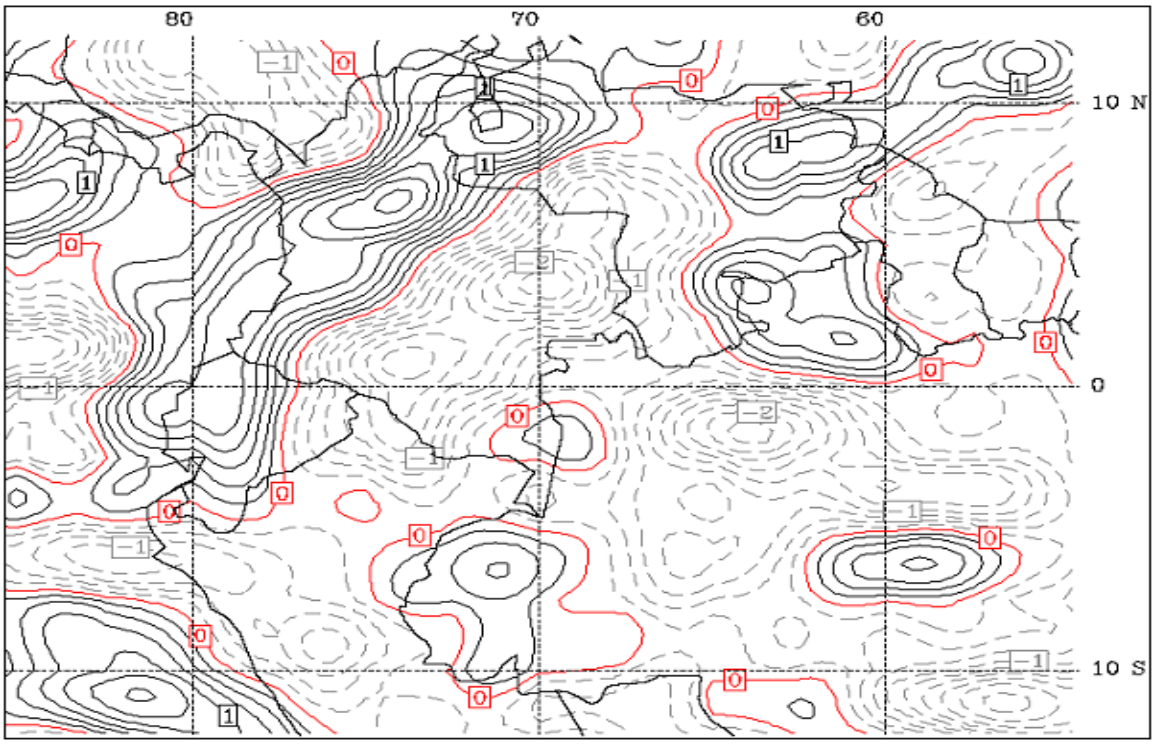

Fig. 29. 700 mb divergence (10^{-5} s^{-1}) for 00 UTC on 18 May 95. Negative values are dashed.

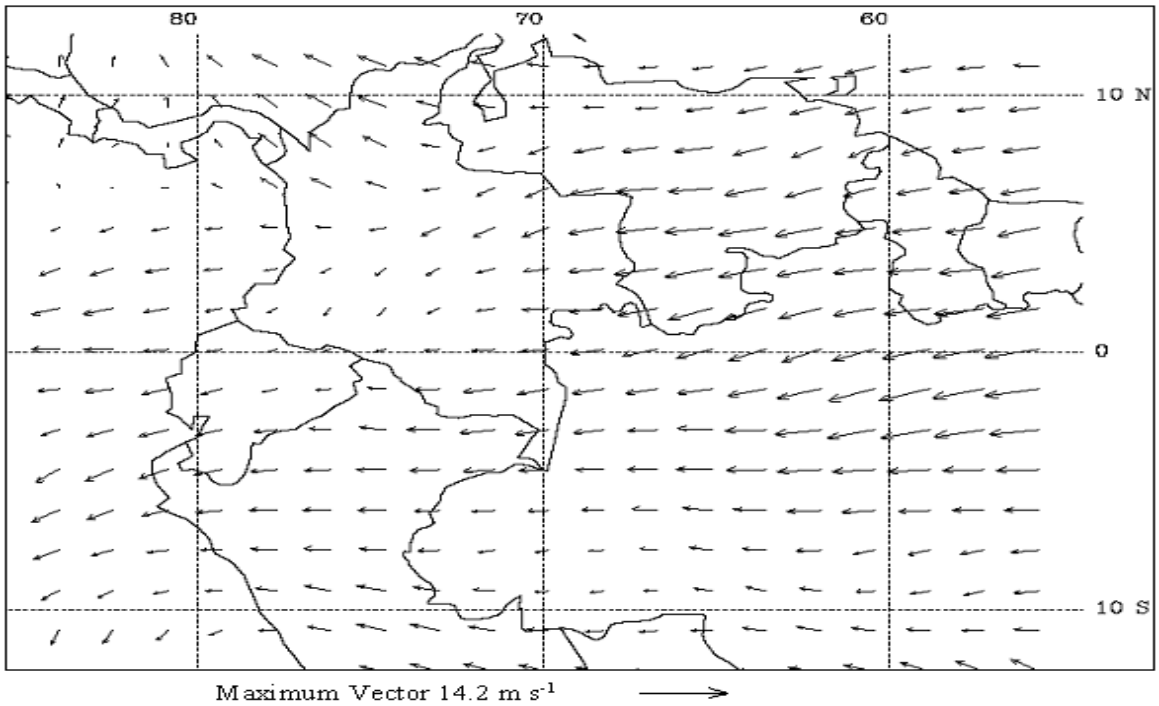

Fig. 30. 700 mb vector analysis for 00 UTC on 18 May 95.

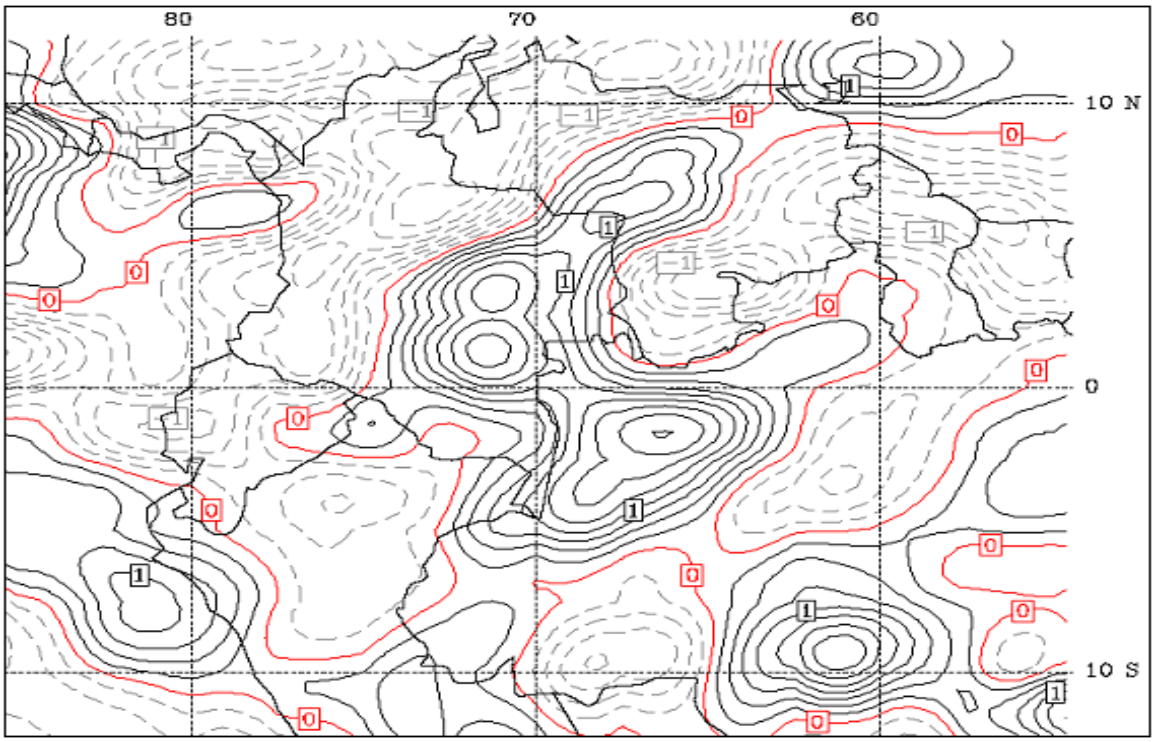

Fig. 31. 400 mb divergence (10^{-5} s^{-1}) for 00 UTC on 18 May 95. Negative values are dashed.

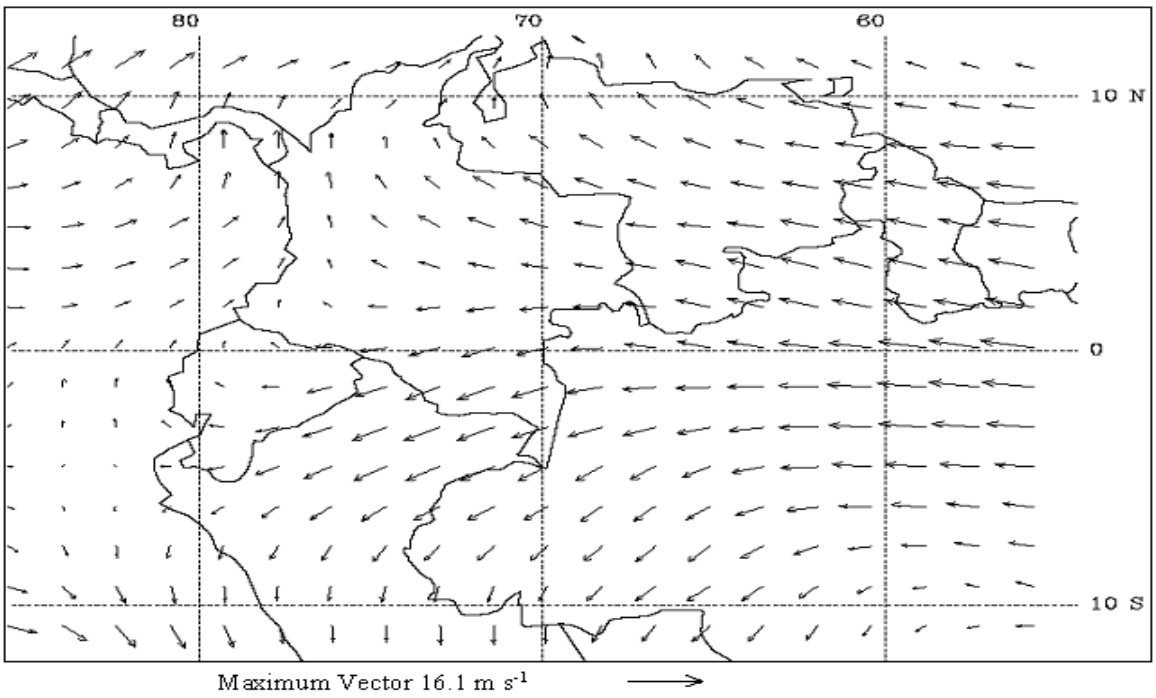

Fig. 32. 400 mb vector analysis for 00 UTC on 18 May 95.

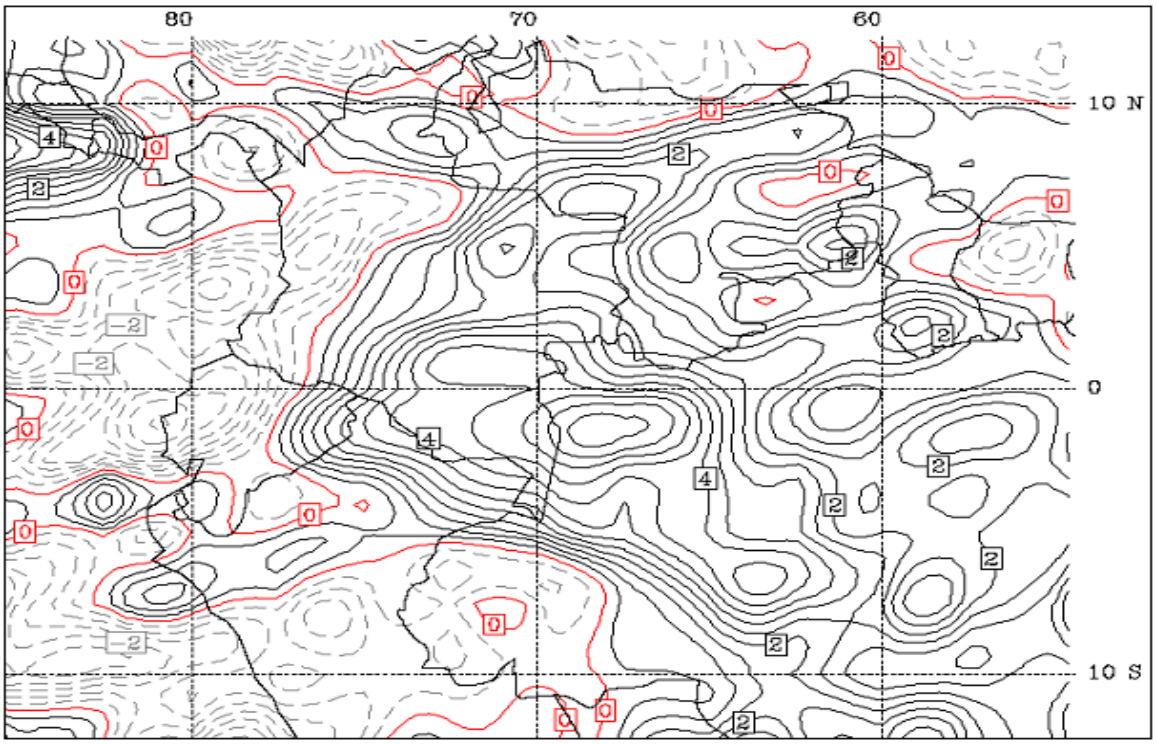

Fig. 33. 500 mb vertical velocity (cm s^{-1}) for 00 UTC on 18 May 95. Negative values are dashed.

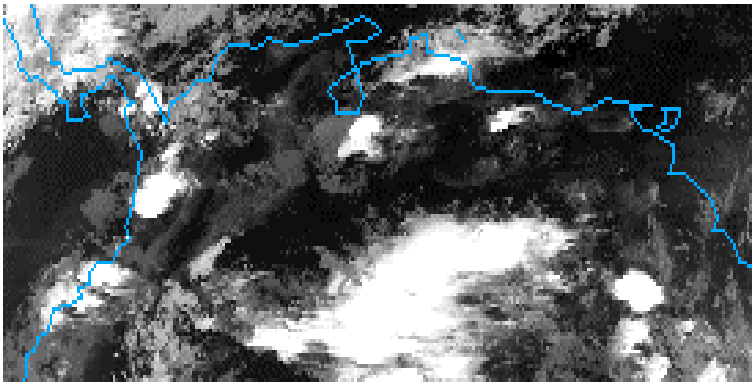

Fig. 34. DMSP IR satellite imagery for 02 UTC on 18 May 95.

A tilt eastward with height of the maximum areas of convergence from 850 to 700 mb is evident in Figs. 27 and 29. This tilt is common among tropical squall lines as the trailing stratified (anvil) sector intercepts the 700 mb easterly inflow (refer to Fig. 4 in section 2.1.1.). Areas of maximum convergence at 700 mb typically lie 100 to 200 nm east of those at 850 mb. Gamache and Houze (1982) and Garstang et al. (1994) also found this feature common to tropical squall lines with the associated level of maximum inflow at 700 mb. Cross section analyses in this research revealed a maximum of winds at 700 mb of 25 to 40 kts in all excessive rainfall events with lesser velocities in 1-2" events. In addition, divergence analyses revealed that over 90% of squall lines tilted with height. With the exception of a couple of events, all 6" and 1-2" precipitation events north of the Equator in this study were associated with tropical squall lines.

With a well-developed tropical squall line, areas of strongest low-level convergence, upper-level divergence, and upward vertical velocities are collocated with the strongest convection. Due to the tilt of convergence areas in the lower levels, concentrated convection usually occurs between the 850 mb maximum convergence area and 700 mb maximum convergence area. The maximum areas of 700 mb convergence (Fig. 29), 400 divergence

(Fig. 31), and 500 mb vertical velocities (Fig. 33) directly correspond to the same location as the immense convection on the satellite imagery (Fig. 34). In addition, notice a less intense but noticeable line of 700 mb convergence (Fig. 29), 400 divergence (Fig. 31), and 500 mb vertical velocities (Fig. 33) in Northwest Brazil. This banding of convergence areas is a common feature with squall lines that form in succession with one another. Incidentally, the convergence band in Northwest Brazil is associated with the smaller clusters of convection southeast of the main area in the satellite image (Fig. 34). Lines of strong convergence and divergence couplets associated with strong upward vertical velocities can align themselves almost parallel with one another as they discretely propagate westward across the continent.

As expected, diurnal differences are also present. Over 90% of the 6" and 1-2" events north of the Equator experienced stronger convection at 00 UTC versus 12 UTC. Although squall lines typically follow the diurnal cycle by weakening at night and rejuvenating during the day, storms from a few cases were able to overcome the loss of sensible heating due to radiational cooling. These select storms often formed in the presence of strong low-level convergence and upper-level divergence. In addition, other atmospheric factors not studied here, such as vorticity and instability for example, may have contributed to the nocturnal occurrences.

Tropical convective rainfall events south of the Equator exhibit some differences from those north of the Equator. While Iauarete and Villavicencio experience similar wet seasons and atmospheric characteristics associated with squall lines, the same is not always true for Benjamin Constant and other locations south of the Equator (i.e. Iquitos and Leticia). The NET is well south of the Equator when locations north of the Equator experience their dry season. In addition, this study found that almost half of all precipitation events were not

associated with squall lines, but rather with the Amazon Low and a convergence of the NET with the SACZ. Fig. 35 illustrates an example of the influence of the NET and SACZ with negative divergence values (convergence) at 700 mb. Vector convergence associated with these values and features are easily seen in Fig. 36. The NET is located just south of the Equator and the SACZ is diagonally located on a line stretching from Northeast Peru southeastward to about 10º S and 60º W.

Another difference between locations north and south of the Equator is diurnal heating. About 40% to 45% of the storms associated with the cases south of the Equator experienced their strongest convection during the early morning hours (12 UTC). Diurnal heating may not be a primary factor for time of convection probably due to smaller diurnal temperature differences in the moisture rich Amazon Basin. Very large evapo-transpiration rates in the basin likely limit the amount of surface sensible heating. As in the northern areas, triggering mechanisms strong enough over the region during the morning hours could spark convection regardless of diurnal heating. Localized factors could also favor night-time convection in the basin.

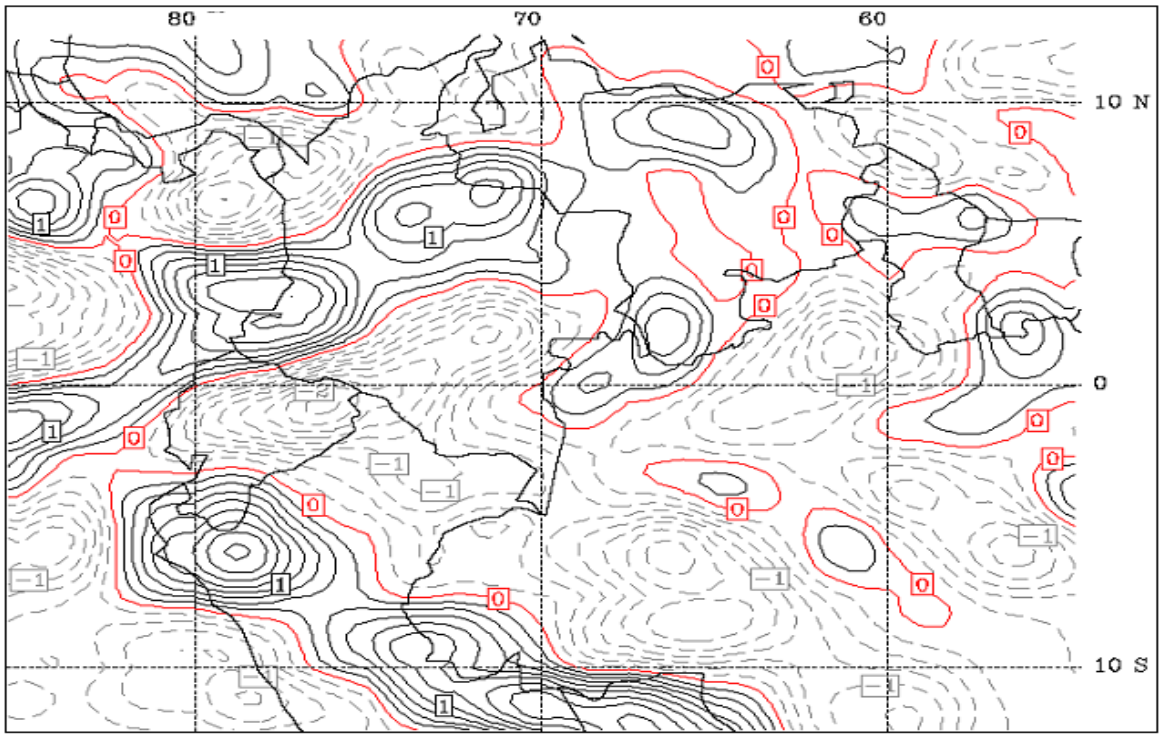

Fig. 35. 700 mb divergence (10^{-5} s^{-1}) for 00 UTC on 13 Nov 95. Negative values are dashed.

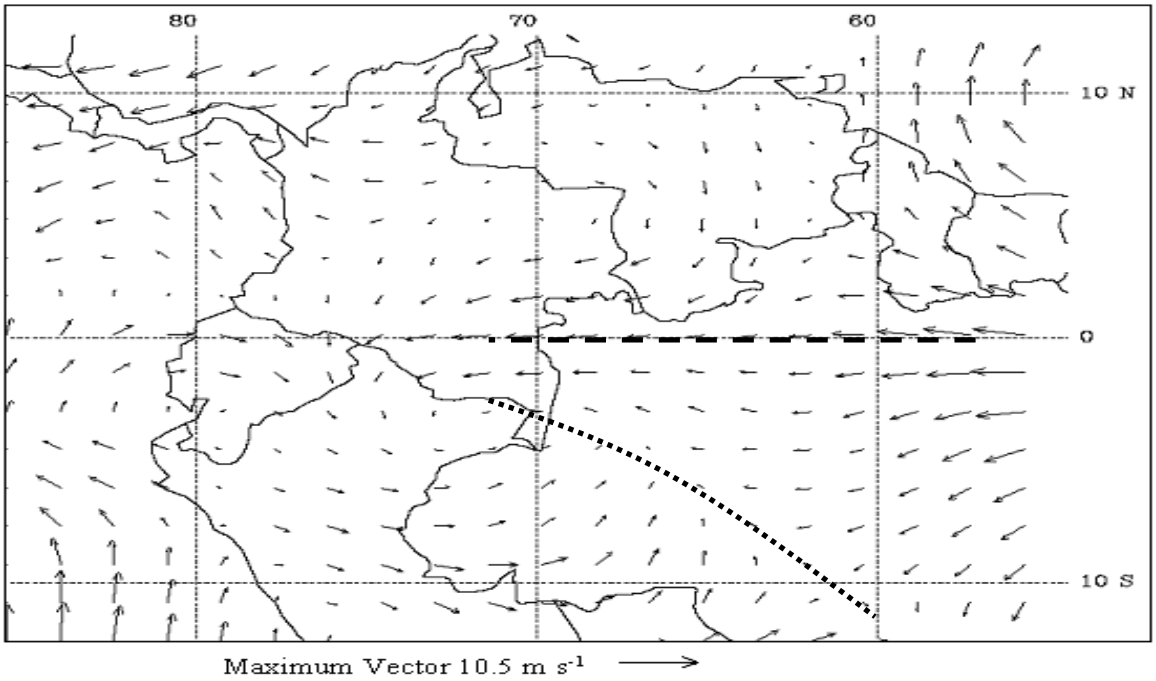

Fig. 36. 700 mb vector analysis for 00 UTC on 13 Nov 95. Dashed and dotted lines represent locations of the NET and SACZ respectively.

Although Appendix C provides forecasting guidance, forecasters must utilize all forecasting tools at their disposal. Wind vector analysis is very useful in determining features responsible for convection; however, only those charts that display divergence and vertical velocity values can truly distinguish the areas of potential convective growth. Additionally, Tables C1 and C2 and Figs. C1 through C4 in Appendix C exemplify very general features common to many events analyzed in this research. Not every feature listed and shown need be present for strong convection. The NET, SACZ, strong low-level pressure gradients with convergence, migrating high-pressure systems at all levels, and upper-level divergence are the main general triggers to convection.

This research did not, however, take into account thermodynamics and dry season events. Tremendous moisture, which is usually present in the tropics during the wet season, and thermal instability are both necessary ingredients for strong convection. Although excessive rainfall events primarily occur during the wet and transition seasons, they can occur during the dry seasons as well. However, the few dry season cases analyzed in this research were all on a scale too small for the model to accurately resolve.

As previously mentioned, GDAS model resolution was a big limiting factor. The lack of resolution from the GDAS model in 1995 and 1996 likely produced divergence and vertical velocity values much lower in comparison to previous research. In addition, the reanalyses from the model produced smoothed values over the entire domain. The smoothing of the data along with the low GDAS model resolution likely introduced errors into the computation of divergence and vertical velocity values. However, the extent of the errors is unknown. The guidelines in Table C4 are those only associated with a model with a T62 resolution. With present models producing resolutions three to four times higher, it's

possible that the values recorded in Appendix C may not necessarily produce excessive rainfall when applied to higher resolution model analyses. As a counteracting statement, however, model resolution is related to actual analysis resolution. The severe lack of a South American upper-air network would limit the efficiency of present-day higher resolution models over SA; therefore, further studies with current models are needed to validate results presented in this research.

4.2. Forecasting Mesoscale Convective Complex Movement in Northern Argentina, Southern Brazil, Paraguay, and Uruguay.

4.2.1. Methodology. Corfidi et al. (1996) proposed a solution to determine movement of MCCs in the U.S. by the simple principle that movement of MCCs is affected by both the propagation and cloud layer advection components. A very similar method can be applied to South American MCCs by utilizing the same principle. This research verified the Corfidi method for SA by applying a very similar process that Corfidi et al. (1996) used to predict MCC movement in the U.S.

For verification, Corfidi et al. (1996) tracked the meso-beta scale convective elements (MBE) of 99 MCCs and 4 MCSs using both radar and hourly satellite imagery. Corfidi et al. (1996) followed the centroid of heavy precipitation echoes on hourly radar imagery and then constructed a straight line of best fit from the beginning to the end of the imagery. Satellite imagery was used to verify MCC or MCS observation using the same definition of an MCC given in section 2.2.1. In addition, Corfidi et al. (1996) verified mean cloud layer speed and direction against individual cells off of radar imagery. This verification was necessary to prove that the mean 850-300 mb cloud layer flow affects the movement of MCCs and MCSs.

Corfidi et al. (1996) only studied those individual cells that would rapidly grow into MCCs or MCSs.

This research verified forecasted MCC and MCS movement and individual cell movement for SA, but by a slightly different process. Due to data limitations, no radar imagery is available. Moreover, only 20 km full-disk IR imagery from GOES-8 at three-hour intervals was available for this study (CIRA 2002; Davison 2002). However, the lack of radar and hourly satellite imagery did not undermine verification of Corfidi's method.

Satellite imagery was used to track 20 MCCs and 2 MCSs merely by tracking the centroid of the system. Maddox (1980) states that the coldest cloud tops relate to the areas of most intense precipitation. By zooming on individual satellite images, one can detect the area or pixels of coldest temperatures. The pixels would then, by Maddox's theory, correspond to the centroid of heavy precipitation echoes used by Corfidi et al. (1996). Only satellite images meeting MCC criteria and very large MCSs (MCSs almost obtaining the size of an MCC) were used in this study. The black dots in Figs. 37-40 illustrate an example of tracking the centroid of an MCC over a nine-hour period. The actual distance, direction, and speed of the MCC was determined by first interpolating the latitude and longitude of the black dot off of satellite imagery. The starting and ending latitude and longitude was then converted to distance and azimuthal angle using Snyder's (1987) spherical equations. The same process was used separately whenever two different MCCs occurred within the same time period. Fig. 41 shows an example of multiple MCCs.

Individual cells were also tracked using the same method as the MCCs and MCSs. With only three-hourly satellite imagery, however, it was very difficult to discern between individual cells and a cluster of cells coalesced together. Only 12 of the 22 cases produced

cells distinctly visible for two consecutive three-hourly images. The white arrows in Figs. 42 and 43 show an example of tracking individual cells over a three-hour period. These cells, forming prior to MCC genesis, eventually blossomed into the same MCC shown in Figs. 37-40. Cells not preceding MCC or MCS development were not included in this study. Distance, direction, and speed were computed using the exact method previously described for tracking MCCs and MCSs. Finally, the speeds and directions of the 12 cases were compared to the 850-300 mb mean flow (the method of finding the mean flow is described later) to verify that cells move downwind with respect to the velocity of the mean flow. If true, then the mean cloud layer velocity would not only govern movement of the individual cells but also of the MCCs and MCSs.

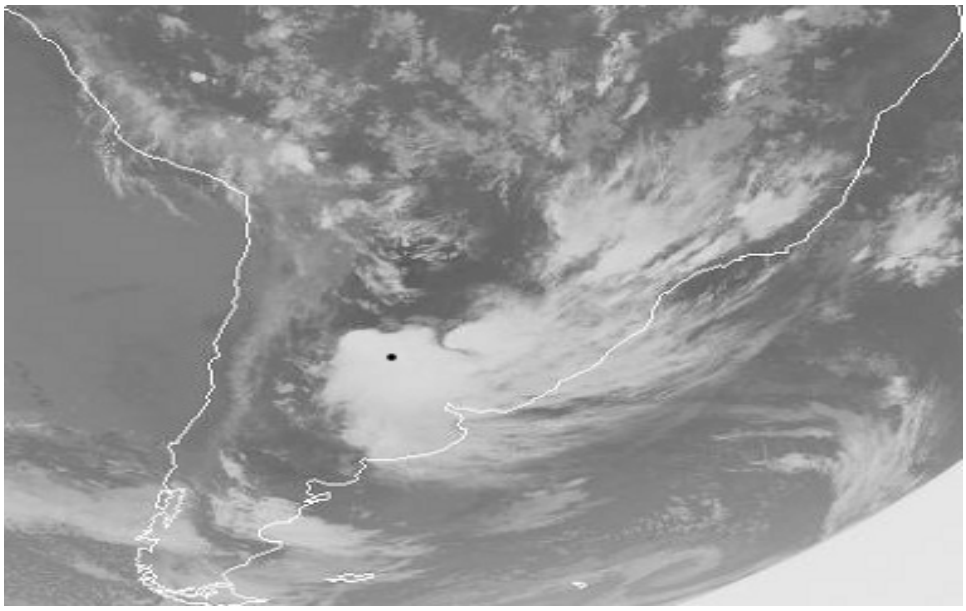

Fig. 37. MCC over SA at 0245 UTC on 25 Nov 02. Black dot represents the centroid of the system (coldest cloud tops).

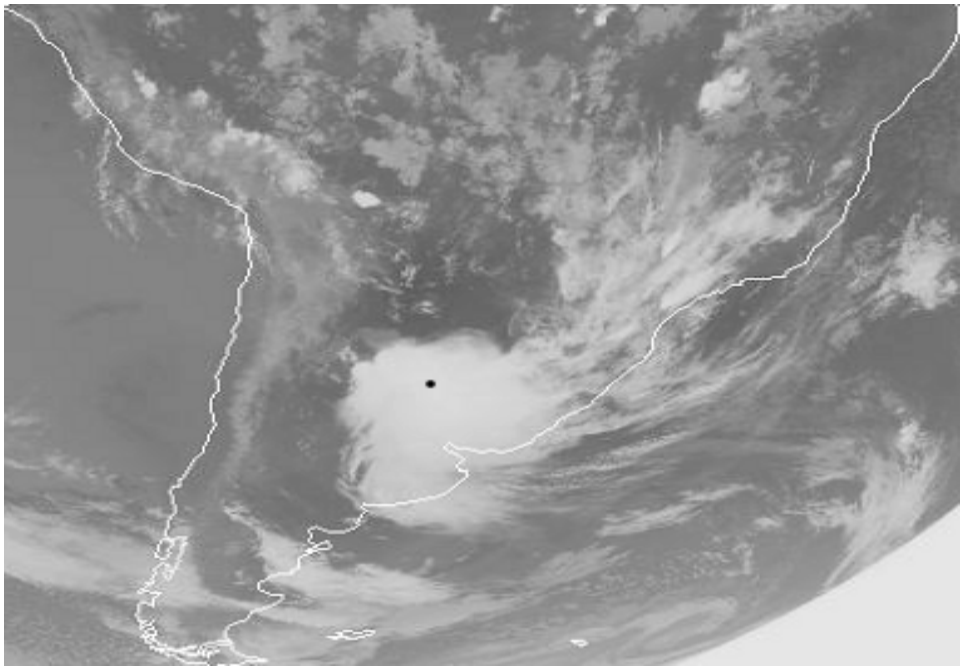

Fig. 38. MCC over SA at 0545 UTC on 25 Nov 02. Black dot represents the centroid of the system (coldest cloud tops).

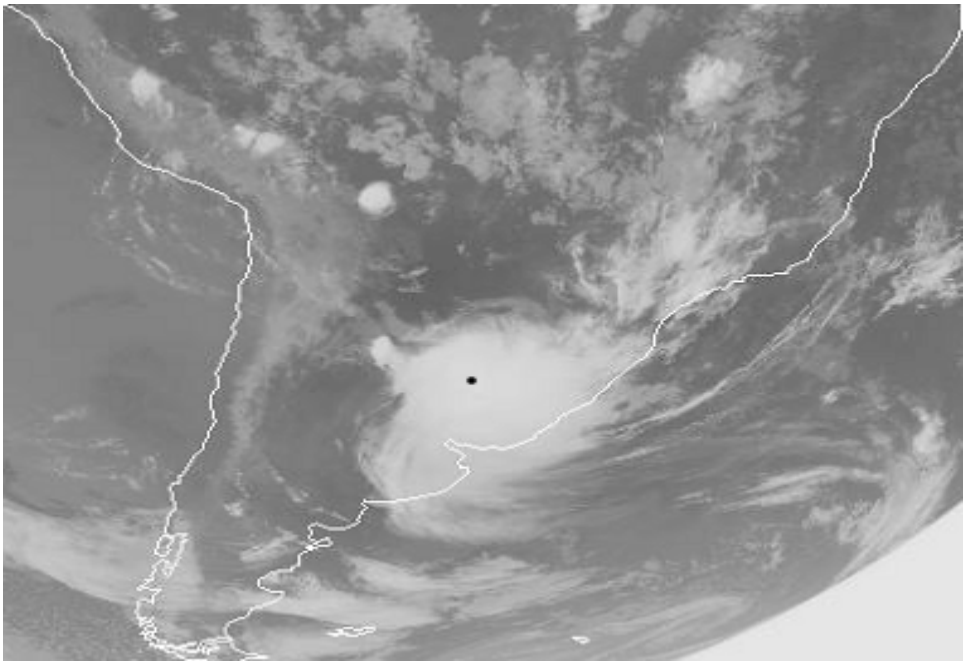

Fig. 39. MCC over SA at 0845 UTC on 25 Nov 02. Black dot represents the centroid of the system (coldest cloud tops).

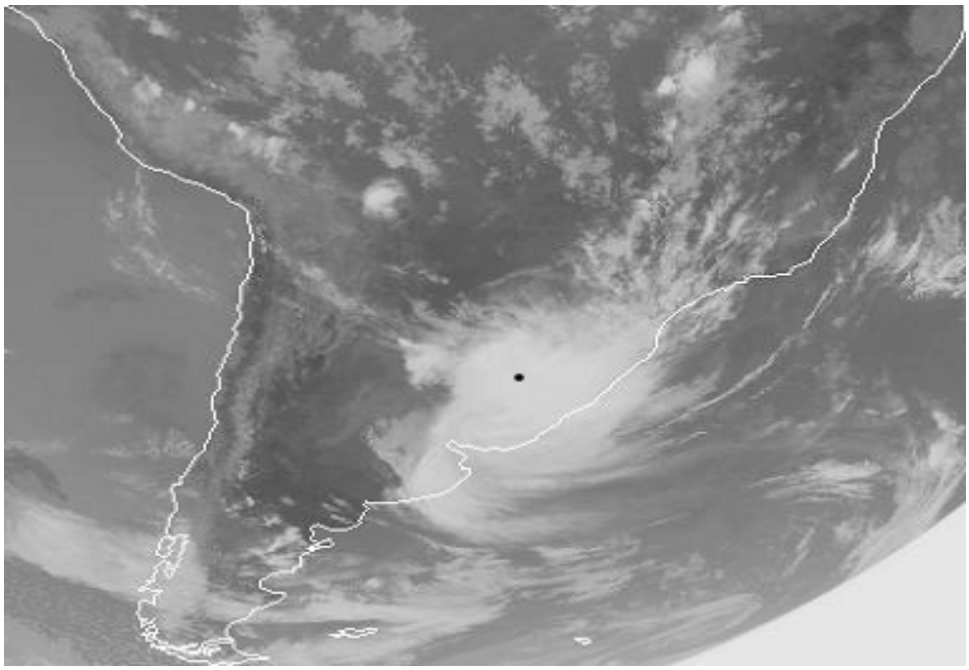

Fig. 40. MCC over SA at 1145 UTC on 25 Nov 02. Black dot represents the centroid of the system (coldest cloud tops).

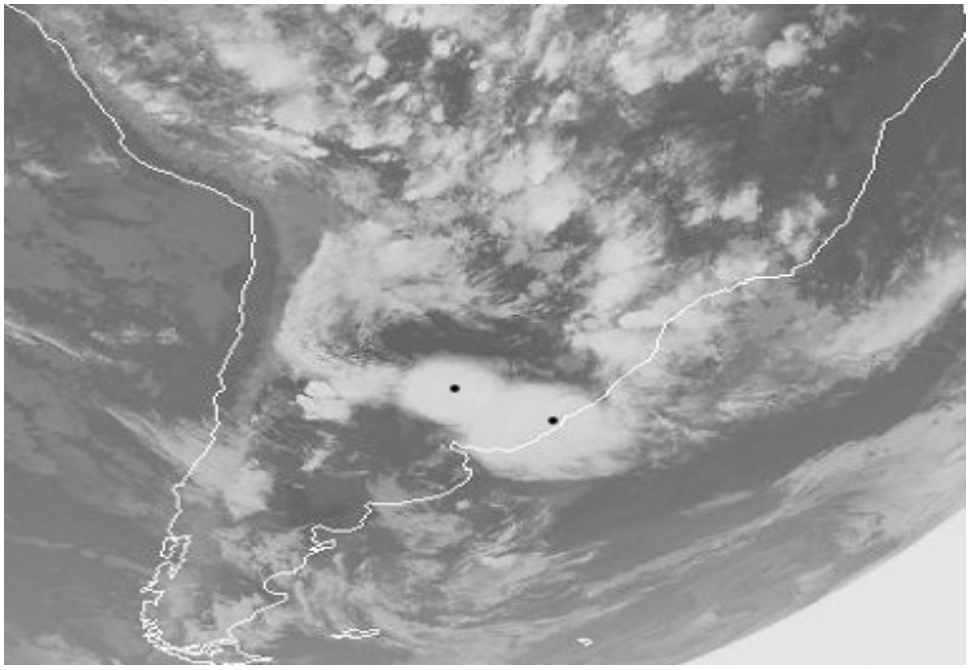

Fig. 41. Two separate MCCs over SA at 2345 UTC on 5 Dec 02. Black dots represent the centroids of the systems (coldest cloud tops).

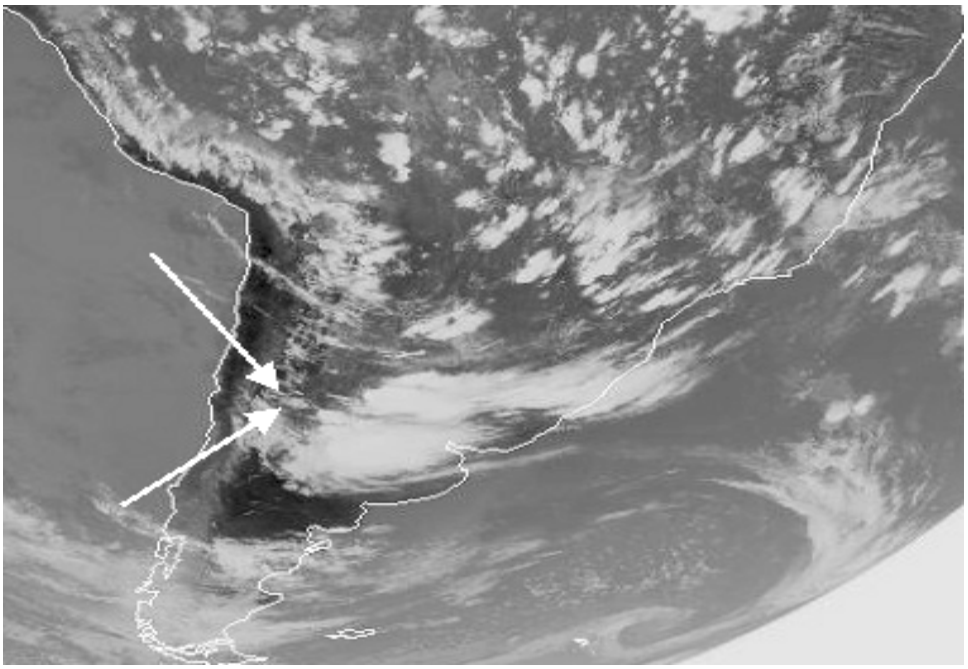

Fig. 42. Individual convective cell (white arrows point to cell) over SA at 1745 UTC on 24 Nov 02. Cell would eventually coagulate with other cells to form an MCC.

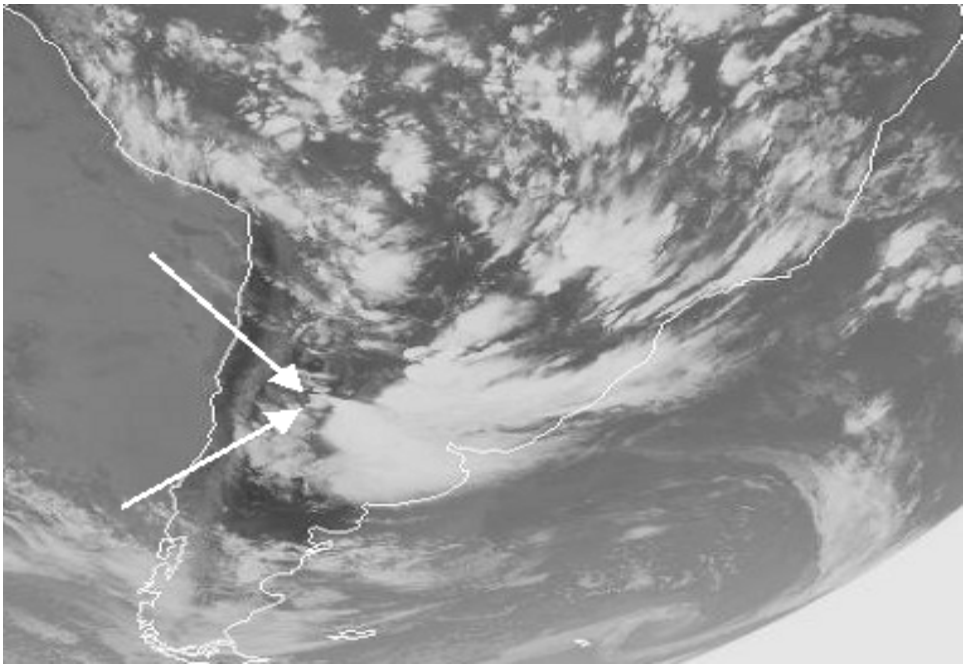

Fig. 43. Individual convective cell (white arrows point to cell) over SA at 2045 UTC on 24 Nov 02. Cell would eventually coagulate with other cells to form an MCC.

Winds associated with the MCC or MCS are necessary for implementation of Corfidi's method. Upper-level wind speed and direction at the location of MCC or MCS genesis were interpolated from 850, 700, 500, and 300 mb NOGAPS wind vector reanalysis charts (FNMOD 2001-2002). This differs from Corfidi et al.'s (1996) research of utilizing the nearest rawinsonde station. As in Corfidi's method, this study utilized the 00 UTC wind data since 00 UTC usually occurred within six hours of MCC or MCS genesis. Per Corfidi et al. (1996), the wind speeds and directions of each level are then inserted into equations 2 and 3 respectively to produce the mean advective, cloud layer component (speed and direction respectively) of the MCC or MCS. The component is simply the mean 850-300 mb wind speed and direction and acts as the component that advects the system downwind (Fig. 44). The advective component increases with increased cloud layer flow. To arrive at a representable mean direction, 360º was added to any 850 and 700 mb wind east of north or south (between 001º and 180º). The process of calculating the advective component was also the same process used in verifying cell movement against the mean 850-300 mb mean flow.

$$V_{CL} = \frac{(V_{850} + V_{700} + V_{500} + V_{300})}{4} \qquad (2)$$

$$DIR_{CL} = \frac{(DIR_{850} + DIR_{700} + DIR_{500} + DIR_{300})}{4} \qquad (3)$$

Corfidi et al. (1996) hypothesized that storms propagate further with stronger LLJs. Although factors such as orographic influences, thermodynamic instability, and outflow boundaries, to name a few, influence propagation, storms mainly form and regenerate in the exit region of the LLJ due to low-level mass and moisture flux convergence. Corfidi et al. (1996) found the propagation component equal in magnitude but opposite in direction of the low-level inflow or LLJ (Fig. 44). In this research, the maximum wind speed and direction

near the location of MCC or MCS genesis were interpolated from 850 mb NOGAPS vector reanalysis charts (FNMOD 2001-2002). Since MCC's typically propagate toward the level of inflow or into the LLJ, this study used the maximum wind speed at 850 mb within 100 nm upwind of the MCC or MCS genesis region.

While Corfidi et al. (1996) strictly followed Bonner's (1968) criteria for the LLJ, this study assumed a LLJ level of 850 mb for all events. This was a valid assumption since Saulo et al. (2000) found the average maximum wind speed associated with the SALLJ to occur approximately at 850 mb. Among LLJ occurrences, Saulo et al. (2000) found an average of 20 m s^{-1} at 850 mb compared against an average of 8 m s^{-1} at 700 mb. Since Saulo et al. based their findings by meticulously following Bonner's criteria; this research used 850 mb as a representable level of maximum inflow.

This research followed Corfidi et al.'s (1996) procedure in verifying the relationship between the direction of the LLJ and the direction of propagation. To verify that the LLJ and propagation components are 180º different in direction with each other, the propagation component must be calculated by inserting the observed mean advective component speed, V_{CL}, observed MCC or MCS speed, V_{MCC}, and α angle into equation 4. Fig. 45 illustrates how the angle, α, between the mean cloud layer and observed MCC velocities influences the magnitude of the propagation component. Equation 5 then uses the calculated propagation component to determine the angle between the actual MCC and propagation components. Fig. 45 depicts how this angle, γ, relates to the actual direction of propagation. If a strong correlation between the actual propagation and LLJ vectors exists, then this suggests that the LLJ is a very good indicator of the direction of propagation of MCC and MCS movement.

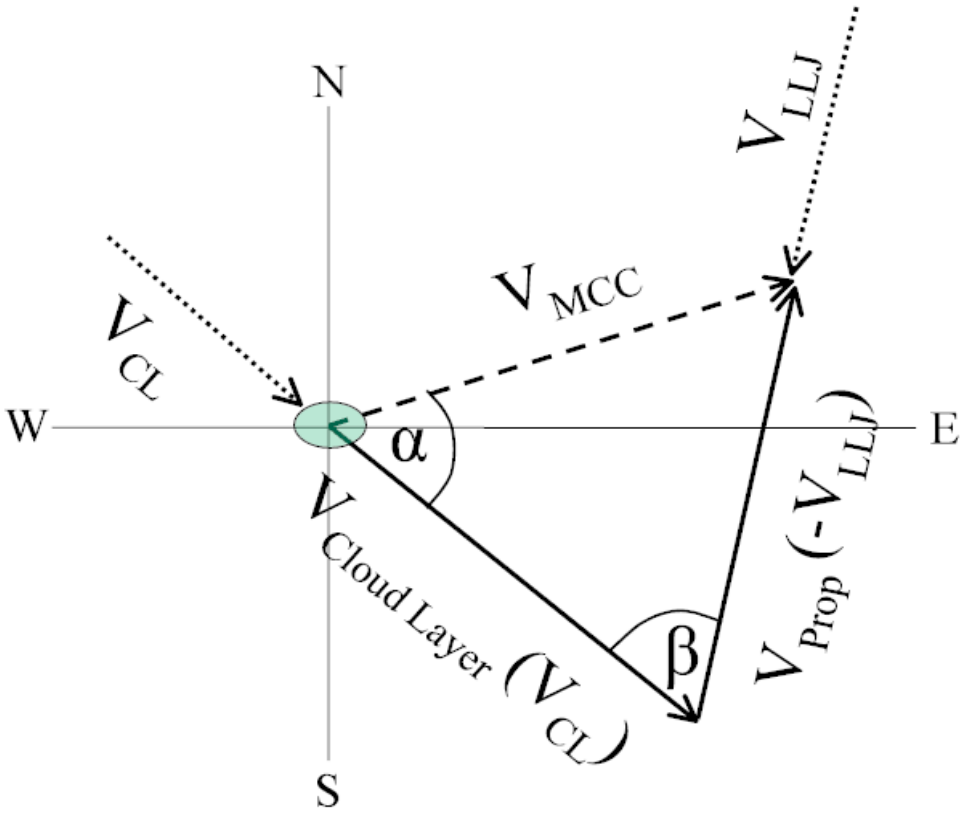

Fig. 44. Conceptual model of the vector components and angles used to predict MCC or MCS velocity, V_{MCC}. The magnitude and direction of the propagation component, V_{PROP} are equal and opposite to the low-level jet, V_{LLJ}. Angles α and β are related to the forecasted MCC or MCS direction and are calculated in equations 8 and 6 respectively. The V_{MCC} vector component is the forecasted component of the MCC or MCS motion. V_{MCC}, calculated in equation 7, is the vector sum of the V_{CL} and V_{PROP} components. The circle at the intersection of the E-W and N-S axes denotes the starting MCC or MCS location.

$$V_{PROP} = \sqrt{(V_{CL})^2 + (V_{MCC})^2 - 2(V_{CL})(V_{MCC})\cos(\alpha)} \qquad (4)$$

$$\gamma = \arccos\left[\frac{(V_{CL})^2 - (V_{MCC})^2 - (V_{PROP})^2}{-2(V_{MCC})(V_{PROP})}\right] \qquad (5)$$

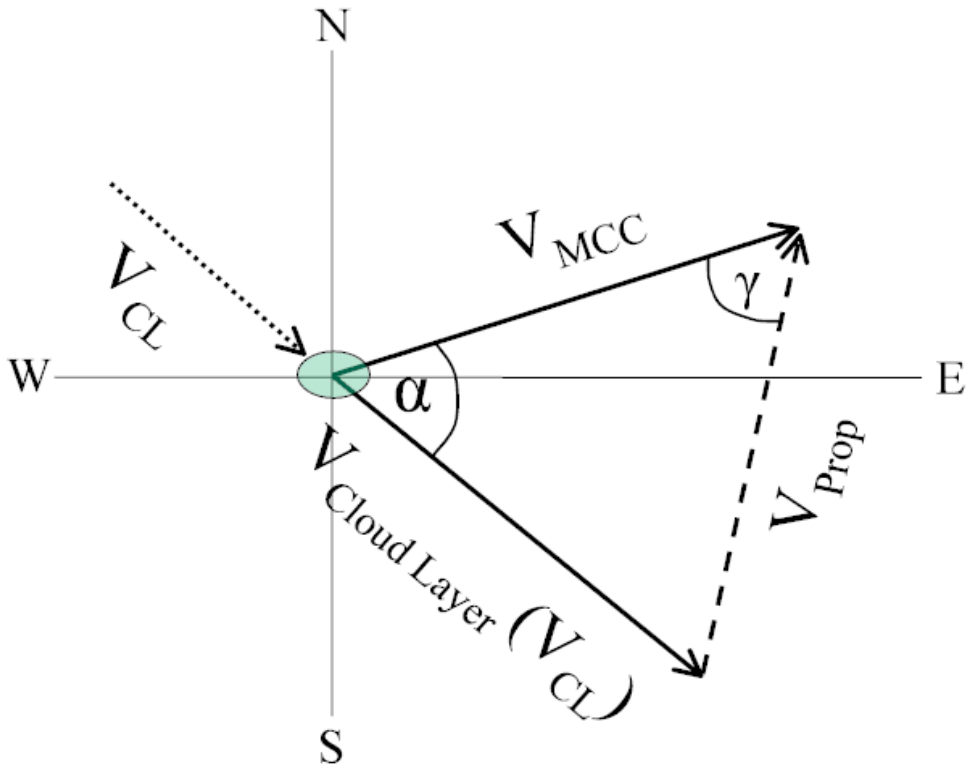

Fig. 45. Conceptual model of the vector components and angles used to predict propagation velocity, V_{PROP}. The V_{MCC} vector component is the observed MCC or MCS motion. V_{PROP}, computed in equation 4, is the vector sum of the V_{CL} and V_{MCC} components. Angle α represents the difference in direction between V_{CL} and V_{MCC}. Angle γ, calculated in equation 5, is related to the propagation direction. The circle at the intersection of the E-W and N-S axes denotes the starting MCC or MCS location.

After showing that both advective and propagation components relate to the mean flow and LLJ respectively, a relationship between forecasted and observed MCC or MCS speed and direction can be formulated. This relationship serves to prove that forecasted MCC and MCS velocities verify against the actual movement of MCCs and MCSs.

Solving equations 6 through 8 creates a forecast of MCC or MCS movement. To compute the magnitude of the system speed, the β angle must first be computed. The angle, illustrated in Fig. 44 and computed in equation 6, is simply the angle between the mean advective and propagation components. 360º was added to either the direction of the LLJ,

DIR_{LLJ}, or mean cloud layer flow, DIR_{CL}, for proper representation. Next, the β angle along with the propagation (or LLJ) and mean cloud layer magnitudes are inserted into equation 7 to arrive at the predicted speed of the MCC or MCS. Finally, the propagation, mean cloud layer, and predicted MCC or MCS magnitudes are inserted into equation 8 to determine the angle, α, between the cloud layer flow and predicted MCC movement. This angle directly relates to the actual direction in which the convective system is heading towards (Fig. 44).

$$\beta = (360 - DIR_{CL}) - (360 - DIR_{LLJ}) \tag{6}$$

$$V_{MCC} = \sqrt{(V_{CL})^2 + (V_{LLJ})^2 - 2(V_{CL})(V_{LLJ})\cos(\beta)} \tag{7}$$

$$\alpha = \arccos\left[\frac{(V_{LLJ})^2 - (V_{MCC})^2 - (V_{CL})^2}{-2(V_{MCC})(V_{CL})}\right] \tag{8}$$

The process for determining predicted MCC or MCS motion differs slightly from Corfidi's method. As illustrated in Figs. 44 and 45, simple right-angle trigonometry does not apply in determining magnitudes and directions. Corfidi et al. (1996) calculated all angles and magnitudes using the law of sines and cosines; however, Corfidi's method leads to errors. Because sine is positive in both the first and second quadrant, any angle over 90º produces erroneous answers. Corfidi et al. (1996) calculated the β angle using the law of sines. This is possible provided the angle between the advective and propagation components isn't obtuse. Although obtuse angles are infrequent, they did occur in one case in this research. To eliminate confusion, this research utilized the law of cosines in equation 8 since cosine exhibits opposite signs within the first two quadrants. To ensure uniformity and accuracy, the law of cosines is also utilized in equations 4, 5, and 7.

Once predicted MCC and MCS magnitudes and directions are calculated, correlations between actual and predicted values are found and compared to Corfidi's research. In

addition, mean speeds, directions, and absolute errors of both observed and forecasted values are computed to compare against Corfidi's results. Standard deviations of the speeds, directions, and average absolute errors are also calculated and compared. Finally, the average absolute directional error between the observed and predicted MCC or MCS directions was translated into distances by multiplying the average absolute directional error by the averaged observed MCC or MCS speed and average length of time of MCC occurrence (11.5 hours in SA). This result, yielding an absolute horizontal distance error, would warn forecasters of the margin of error this process exhibits.

4.2.2. Results. Verification of Corfidi's method was applied to SA. The first step in verifying Corfidi's method for SA was to separately describe the results for the two components that comprise MCC and MCS movement, the advective and propagation components. After component verification, observed MCC and MCS velocities are compared against forecasted velocities. Finally, results of all findings are compared to Corfidi's method. This research also includes an outline of the SA method for forecasting MCCs and MCSs in Appendix D. This appendix, written in lay terminology, also includes an example from which forecasters can apply to forecast MCCs and MCSs in Central and Southern SA (south of 15º S).

The advective component verified very well against the mean cloud layer (850-300 mb) speed and direction. Figs. 46 and 47 illustrate the correlations and scatter plots for 12 cases. The other ten cases lacked two consecutive satellite images with distinct cell visualizations; therefore, they weren't used. Both scatter plots represent a near linear relationship between the observed cell movement and 850-300 mb mean velocity. These strong correlations mean that the advective component plays a major role in determining MCC and MCS movement.

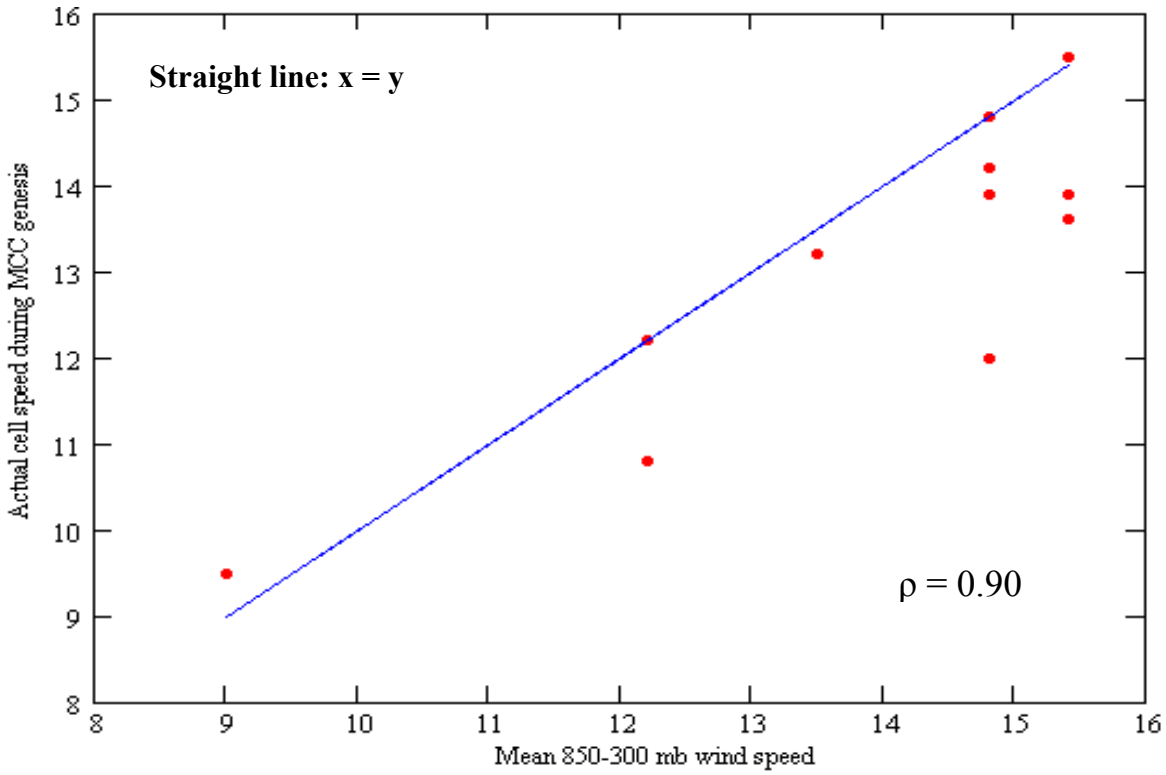

Fig. 46. Scatter plot of observed cell speed versus mean 850-300 mb wind speed for 12 cases during the MCC or MCS genesis stage. Included is the correlation coefficient (ρ-value). Straight line indicates a perfect one-to-one relationship.

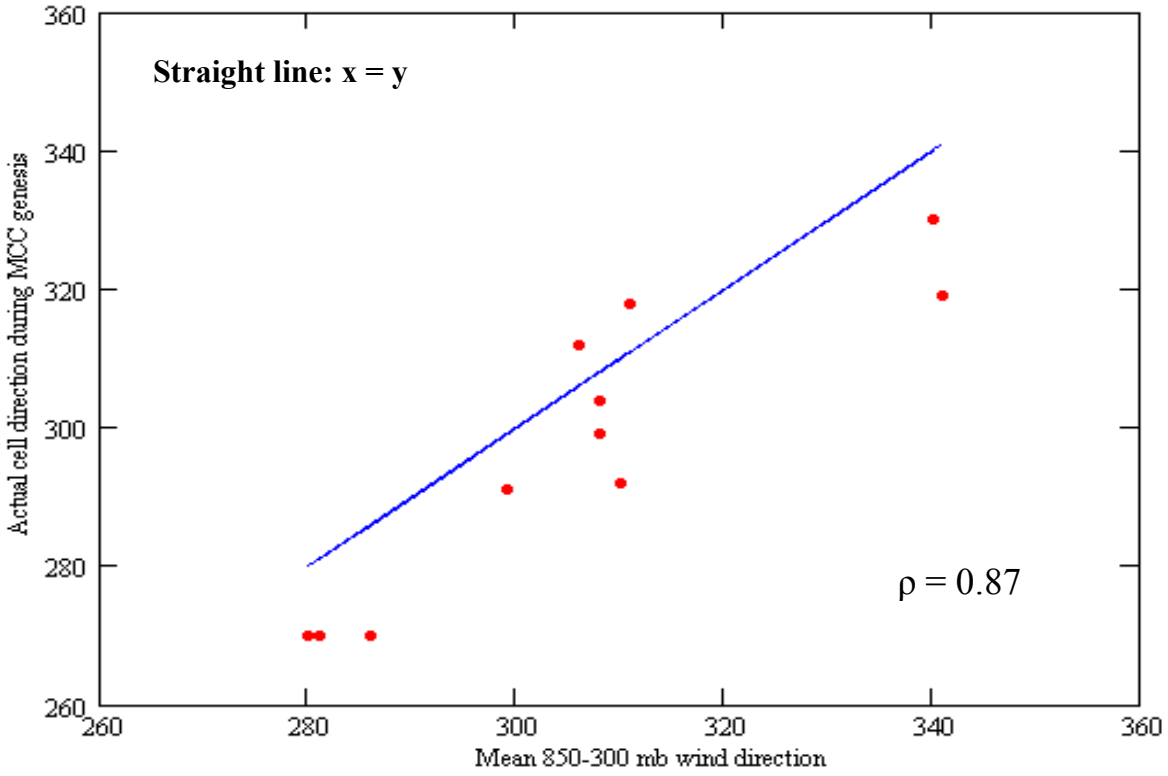

Fig. 47. Scatter plot of observed cell direction versus mean 850-300 mb wind direction for 12 cases during the MCC or MCS genesis stage. Included is the correlation coefficient (ρ-value). Straight line indicates a perfect one-to-one relationship.

The correlations for the advective component were much stronger than those presented in Corfidi et al.'s (1996) research. This research found correlation coefficients of 0.90 and 0.87 for the speeds and directions respectively versus 0.71 and 0.76 for Corfidi's NA method (Table 13). A couple of hypotheses could explain the stronger correlations for SA. Stronger westerlies in NA could account for larger variations in the mean flow, therefore, leading to more error in predicting cell movement. However, the more likely hypothesis concerns the difference in system height. In computing mean layer velocity, Corfidi et al. (1996) equally weighted all four levels presented in equations 2 and 3. Although the mid-levels of the troposphere drive the storm's movement, Corfidi et al. (1996) placed equal weight on the lowest levels, 850 and 700 mb, because most air entraining

thunderstorms enters at the lowest levels. Equal weight is also placed on the highest level, 300 mb. This level could be causing the differences in correlations between the Corfidi's method and the SA method. In SA, warm season tropopauses average around 100 mb, 50-100 mb higher than NA tropopauses. Higher tropopauses likely contribute to the larger MCC sizes in SA (Velasco and Fritsch 1987). The higher, larger convective storms in SA would place the 300 mb level nearly in the middle of the storm's vertical extent; therefore, making 300 mb a significant steering level. On the other hand, 300 mb would not play as large of a part in steering convective cells in NA since it would lay in the top quarter to third of the storm. To summarize, the equal weight of 300mb in equations 2 and 3 may be more accurate for SA than NA.

Fig. 46 shows all values either near or below the line of a perfect one-to-one relationship. The plots below the line represent mean layer speeds stronger than the speeds of the cells. This makes physical sense since cell propagation, though not as strong as MCC propagation, decreases cell speeds to less than the mean layer speed.

The propagation component also verified better than Corfidi et al's (1996) results. The scatter plot for observed propagation direction versus LLJ direction for SA is illustrated in Fig. 48 for 21 cases. One out of the 22 cases wasn't used due to an abnormally weak LLJ speed. This figure demonstrates that the LLJ direction is a clear indication of the propagation component. In addition to better correlation coefficients (0.75 for SA vs. 0.65 for NA (Table 13)), there is much less variance in the entire population of LLJ directions. The absolute variation, maximum value minus minimum value, is only 80º for SA cases but almost 180º for NA cases (Corfidi et al. 1996). Less variation in the ocean-dominated SH westerlies,

steeper terrain in SA, and smaller SA continent width likely cause the smaller variance among SALLJ directions.

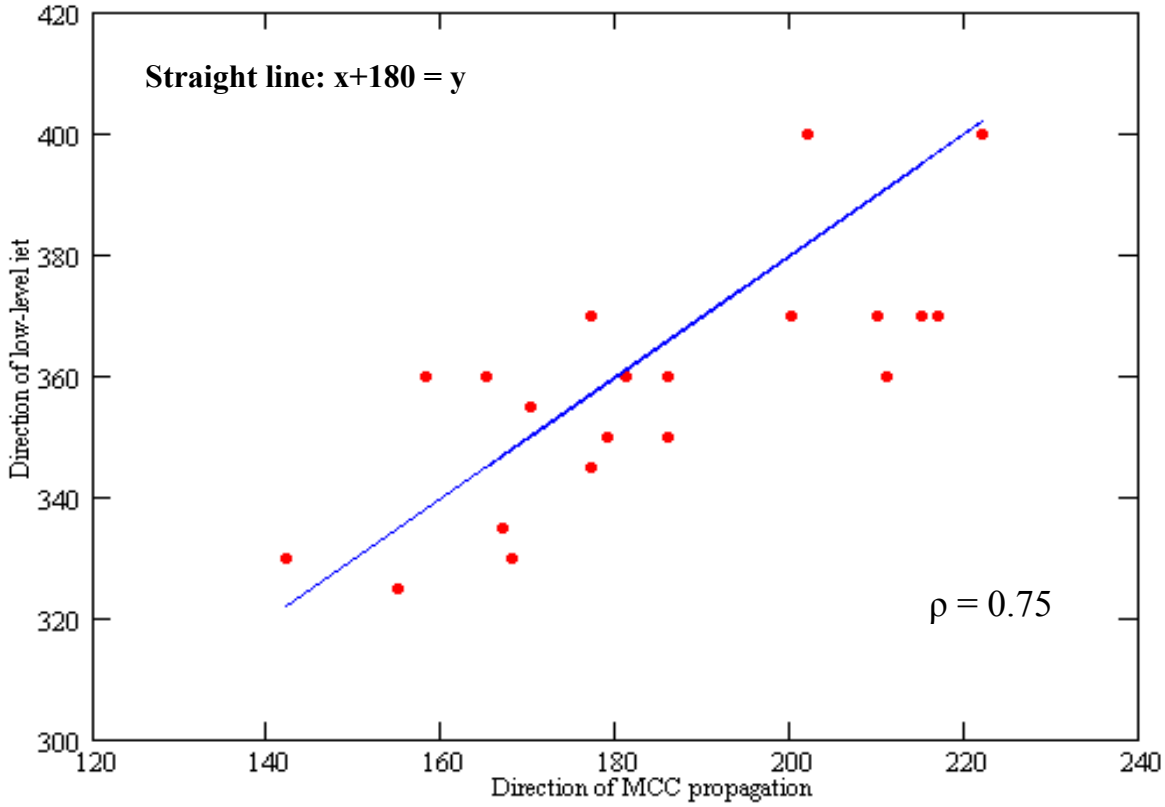

Fig. 48. Scatter plot of actual MCC and MCS propagation direction versus mean LLJ direction for 21 cases. Included is the correlation coefficient (ρ-value). Straight line indicates a perfect 180º relationship between the LLJ and propagation directions. LLJ directions between 000º and 040º are plotted between 360º and 400º.

The forecasted MCC and MCS speeds and directions compared well to the observed speeds and directions. Figs. 49 and 50 depict the scatter plots for the speeds and directions respectively for all 22 cases. Both graphs exhibit a semi-linear fit of observed versus forecasted magnitudes and directions. Correlation coefficients of 0.72 and 0.81 for the speeds and directions respectively for the SA method results are comparable to Corfidi's correlation coefficients of 0.80 and 0.78 for speeds and directions (Table 13). Although the

correlation is weaker in this study for SA MCC speed comparisons versus Corfidi's MCC speed comparisons, the coefficient increases from 0.72 to 0.84 upon omission of the three-point grouping in the upper-left part of Fig. 49. These points, however, were not outliers; therefore, this study included them.

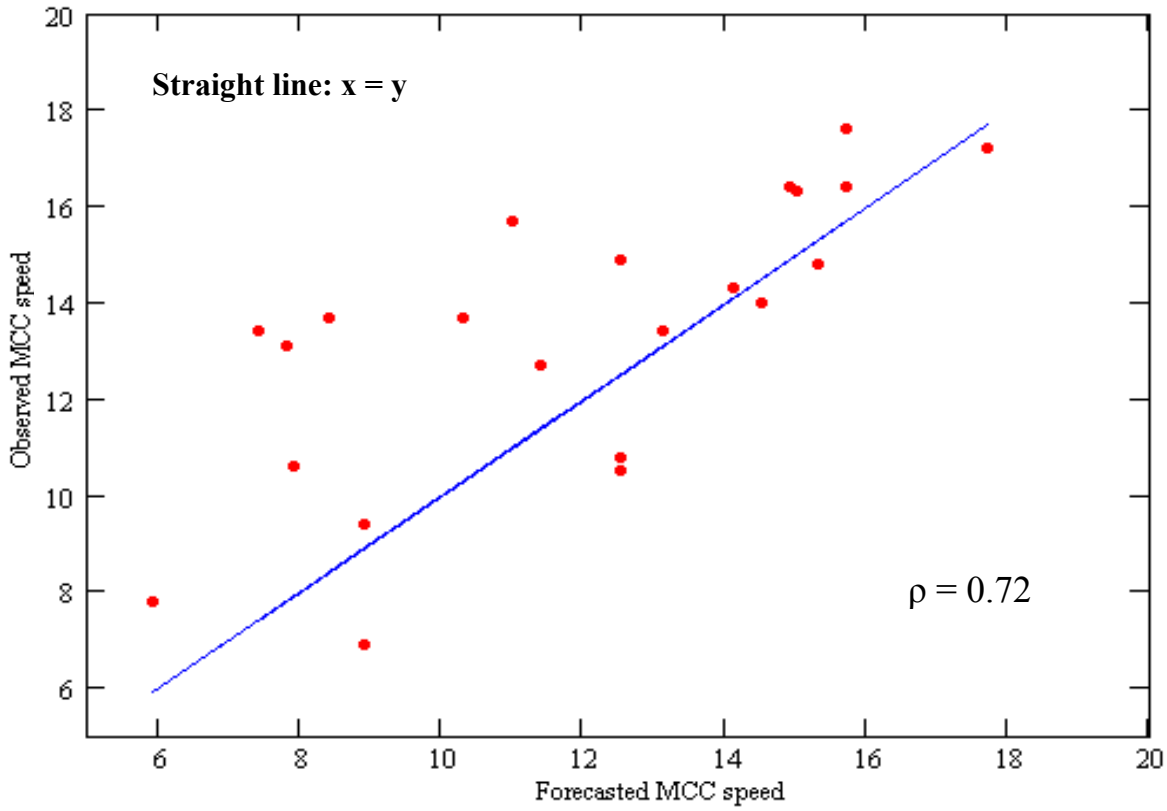

Fig. 49. Scatter plot of observed versus forecasted MCC and MCS speeds for 22 cases. Included is the correlation coefficient (ρ-value). Straight line indicates a perfect one-to-one relationship.

An interesting observation in Fig. 49 is that most of the plots favor the upper half of the scatter plot. Values above the line represent underforecasting of the MCC or MCS speed. Synoptic scale features could account for the disparity. Several MCCs and MCSs in this study were associated with transient squall lines or fronts. Others associated themselves with moderate to strong shortwaves. Although this study does not disclose the synoptic details of

each case, it is hypothesized that synoptic factors not accounted for in Corfidi's method for either NA or SA cause faster observed motion of MCCs and MCSs.

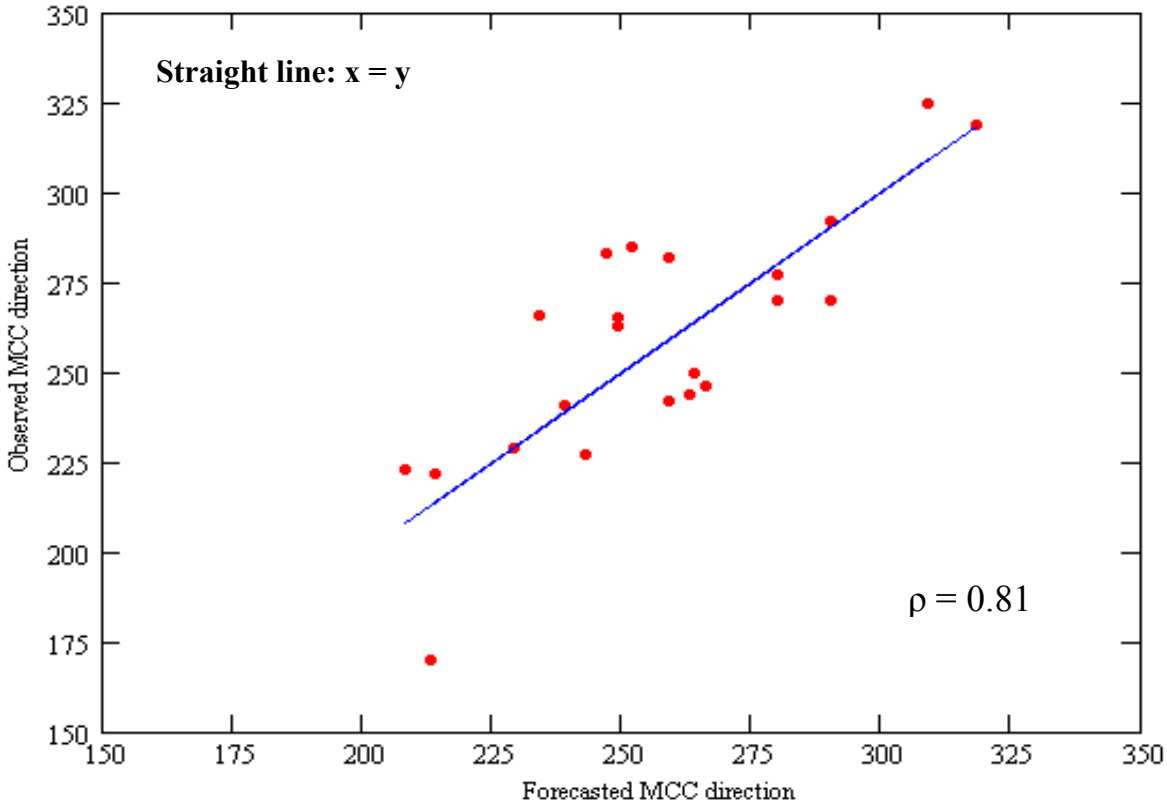

Fig. 50. Scatter plot of observed versus forecasted MCC and MCS directions for 22 cases. Included is the correlation coefficient (ρ-value). Straight line indicates a perfect one-to-one relationship.

Observed means, standard deviations, and average absolute errors for MCC and MCS speeds for both Corfidi's NA method and the SA method are presented in Table 14. Results compare well between both methods with a couple of exceptions. Both observed and forecasted mean MCC and MCS speeds were less in SA likely from the weaker SH westerlies inhibiting the advective component of motion. Also, the standard deviation of observed MCC and MCS speeds is much less in SA than NA. The smaller variance in SH westerlies probably accounts for the lesser standard deviation for observed SA MCC and

MCS speeds. In addition, MCCs and MCSs generally form from 25º to 35º S compared to NA MCCs forming between 30º and 50º N (Velasco and Fritsch 1987). The greater latitude variation in NA could also cause greater speed variances between NA MCC and MCS cases since mid-latitudes experience stronger effects from the polar jet than sub-tropical latitudes. Furthermore, SA MCCs and MCSs occur more frequently in lower latitudes where westerlies are climatologically lower. To summarize, less variation in latitude and upper-level westerly speed among SA MCC and MCS cases probably attributes to the lower speed standard deviation.

Table 13. Comparison of correlation coefficients between Corfidi's method for NA and the method developed for SA. Number of observations is represented by the n-values and correlation coefficients are represented by the ρ -values.

	Method for NA (Corfidi's method)		**Method for SA**	
	n-value	**ρ-value**	**n-value**	**ρ-value**
Cell speed vs. 850-300 mb mean wind speed	74	.71	12	.90
Cell direction vs. 850-300 mb mean wind direction	74	.76	12	.87
Propagation direction vs. LLJ direction	103	.65	21	.75
Observed vs. forecasted MCC or MCS speed	103	.80	22	.72
Observed vs. forecasted MCC or MCS direction	103	.78	22	.81

Comparisons between MCC and MCS directions computed from both methods also show some interesting results (Table 14). The observed and forecasted directions from Table 14 show that the MCCs and MCSs move equatorward in both hemispheres, which is more evidence that propagation indeed occurs. This is of no surprise given that the level of moist inflow originates equatorward from MCC and MCS formation. Furthermore, the Coriolis

parameter contributes to equatorward motion of the MCC or MCS over an extended period of time.

The average absolute error for directions (Table 14) differs from both continents. A smaller mean error and standard deviation occurs in SA MCC and MCS cases. Greater directional variation in the U.S. LLJ could explain the greater average absolute error in NA. The propagation direction, linked to the LLJ direction, alters the movement of the MCCs and MCSs. Although Corfidi et al.'s (1996) average absolute error is sufficiently small, less error in SA more than justifies use of Corfidi's technique to forecast SA MCC and MCS movement.

Average absolute errors in both speed and direction are acceptably small to use in forecasting MCCs and MCSs. The directional average absolute error would, however, yield the greater potential for incorrect forecasted MCC and MCS placement. An average absolute directional error for SA of 16.4º translates into an average absolute horizontal distance error of 134 km (Avg. observed mean speed x sin(16.4) x 11.5 hrs). 11.5 hours is the average lifespan of SA MCCs (Velasco and Fritsch 1987). This error indicates the MCC or MCS will be, on average, 134 km from the MCC or MCS forecasted position at 11.5 hours. Of course, re-application of the method throughout the MCC or MCS lifespan will significantly decrease the absolute horizontal error. This error compares very well to the absolute horizontal distance error of roughly 138 km for NA. Despite the seemingly large distance error, this still places the MCC within its 300 km diameter heavy rain band (Corfidi et al. 1996; Maddox et al. 1986).

Table 14. Comparison of observed and forecasted MCC and MCS speeds and directions for both Corfidi et al.'s (1996) method for NA and the method developed for SA. Comparison includes standard deviations (Std. dev.) and average absolute errors. Average absolute error is the sum of the absolute errors for all cases divided by the total number of events.

	Method for NA (Corfidi's method) (based on 103 cases)		**Method for SA (based on 22 cases)**	
MCC or MCS Speed (m s^{-1})				
	Mean	**Std. dev.**	**Mean**	**Std. dev.**
Observed	13.6	4.7	13.3	2.9
Forecasted	13.0	3.5	11.9	3.3
Avg. absolute error	2.0	1.8	2.1	1.8
MCC or MCS Direction (degrees)				
	Mean	**Std. dev.**	**Mean**	**Std. dev.**
Observed	295.3	32.8	258.7	34.6
Forecasted	294.8	30.7	257.0	29.4
Avg. absolute error	17.2	12.3	16.4	11.8

There are, as usual, shortcomings to every forecast technique. Corfidi's method is based only on quasi-stationary or backward propagating MCSs such as MCCs. This method doesn't apply to forward propagating MCSs such as derechoes, bow echoes or squall lines. Also, MCC and MCS propagation processes require further understanding. In addition to a LLJ, Corfidi (1998) states that high moisture content must be present through a deep layer for propagation to occur. Very high dewpoints, high equivalent potential temperatures, and greater precipitable water contents in the Gran Chaco and Parana Basin region leads to propagation of MCCs and MCSs in that very direction. Direction of propagation also depends on additional knowledge of the environment in which MCCs and MCSs form. For example, the advective component may dominate in a faster westerly flow with a strong shortwave or with a transient squall line or front. On the other hand, quasi-stationary fronts, meso-highs caused by outflow boundaries, and terrain-induced wind flows such as katabatic flow could enhance propagation. Additionally, the area of strongest low-level convergence

may not necessarily coincide with the area of convergence associated with the LLJ, but with the area of greatest system-relative low-level convergence (Corfidi 1998). Although Corfidi's method for both continents is highly effective, forecasters must always be vigilant for any mesoscale and synoptic scale changes that adversely affect the advective and propagation components.

V. Conclusions and Recommendations

5.1. Excessive Rainfall, Fog, and Low-Cloud Bases over Columbia, Ecuador, and Northern Peru east of the Andes.

5.1.1. Conclusions.

5.1.1.1. Relationship between Fog and Low-Cloud Bases to Precipitation Occurrences.

Appendix A outlines the frequency of occurrences of low ceilings and visibilities for the mid-morning (12 UTC) following a 24-hour precipitation event of 1" or greater which ends approximately at 06 UTC into three tables: Benjamin Constant, Brazil; Iquitos, Peru; and Leticia, Columbia. Results from all three locations show higher accumulated precipitable water content yielding a greater probability of reaching saturation following radiational cooling. These locations bear a greater probability than climatology of low ceilings and visibilities or fog occurring after a 1" or more precipitation event. This study excludes Villavicencio due to its questionable ceilings and Apiay AB due to its small sample size.

Appendix A provides forecasters at the SOUTHCOM weather forecast center an indication of the likelihood of dropping below a certain category given an inch or more of precipitation has occurred. The frequencies also apply to any event that yields close to an inch of rain in 24 hours. Although the probability tables are based on actual observations, forecasters can treat the probabilities as a perfect-prognostic forecast in forecasting ceilings and visibilities when they are also forecasting precipitation intensities. However, caution must apply with this approach since no verification of forecasted ceilings and visibilities based on forecasted precipitation intensities was presented in this research. Forecasters must be aware of other meteorological factors that could affect the probability of dropping below a

certain category since the frequencies listed in Appendix A do not favor any certain meteorological pattern. In addition, forecasters must pay attention to the time of day precipitation ends. A precipitation event ending around midnight local time has a much higher probability of producing ceilings and visibilities below a certain category than precipitation ending much earlier in the day since any significant amount of drying or diurnal heating following a heavy rainfall event could diminish the likelihood of observing fog and low-cloud bases the subsequent morning.

5.1.1.2. Determining Ceilings and Visibilities from Precipitation Events. Section 1 of Appendix B outlines the frequency of occurrences of low ceilings and visibilities, given a certain precipitation intensity has occurred, into three tables: Iquitos, Peru; Leticia, Columbia; and Apiay AB, Columbia. Results from all three locations show increased probabilities of low ceilings and visibilities as precipitation intensity increased. The probability results show lower ceilings and visibilities for West Amazon Basin locations versus Apiay AB. The difference in ground moisture availability and terrain (jungle and swamps in the basin to savanna in the highlands) likely cause the dissimilarity.

Section 2 of Appendix B summarizes ranges of probabilities of forecasting ceilings and visibilities, given a certain precipitation intensity has occurred, into 24 tables. Each table represents probabilities for either ceilings or visibilities associated with all four intensities for all three locations: Iquitos, Leticia, and Apiay AB. Ceilings and visibilities lowered with increased rainfall intensity. In addition, the probability of occurrence within a lower range of ceilings (less than 6000 ft) also increased with increased precipitation intensity. Apiay AB climatologically registers higher ceilings and visibilities than Iquitos and Leticia probably due to terrain and ground moisture differences.

Both sections of Appendix B provide SOUTHCOM forecasters guidance towards forecasting specific ceilings or visibilities or the likelihood of dropping below a certain category whenever forecasters predict or find observations of drizzle, light rain, moderate rain, or heavy rain for the same three specific locations. The additional forecaster guidance ("forecaster tidbit") located at the bottom of all tables in section 2 of Appendix B also serves as invaluable information about the likelihood of a certain ceiling or visibility occurring. However, forecasters must exercise vigilance of other meteorological factors that could affect the probability of dropping below a certain category or falling within a range, for the probabilities and ranges of ceilings and visibilities presented in Appendix B do not favor any certain meteorological pattern or time of year. Factors such as length of precipitation event, time of year, and localized variability of atmospheric conditions with respect to terrain and location with convective storms could alter the probabilities. Moreover, the probability and range tables are based on actual observations. Forecasters can treat the probabilities and range of ceilings and visibilities as a perfect-prognostic forecast in forecasting ceilings and visibilities when they are also forecasting precipitation intensities. However, caution must apply with the perfect-prognostic approach since no verification of forecasted ceilings and visibilities based on forecasted precipitation intensities was presented in this research. Although Apiay AB provides a guide to forecasting ceilings and visibilities, forecasters must exercise more caution with Apiay AB than the other two locations due to Apiay AB's much smaller data set size.

5.1.1.3. Forecasting Excessive Rainfall Events. Appendix C guides forecasters in predicting excessive rainfall events (events producing approximately 6" or greater in 24 hours) over NWSA during the wet and transition seasons using careful analysis of divergence

fields, vertical velocity fields, and wind vector analysis charts. Divergence and vertical velocity values for 6" or greater events were more than double those found in 1-2" events. These findings reveal a significant increase in the strength of atmospheric triggering mechanisms associated with rainfall events 6" or greater.

Wind vector analysis charts illustrate important meso-alpha and synoptic scale features with 6" precipitation events. Stronger trade winds with stronger low-level pressure gradients, migrating high pressure systems at all levels, placement of the NET and SACZ, upper-level shortwaves, thermal lows, and changing mesoscale flows work in concert with each other either directly or indirectly to produce strong low-level convergence, upper-level divergence, and upward vertical velocities. These features are outlined and illustrated in Appendix C.

Divergence values, vertical velocity values, and wind vector analyses provide guidance to forecasters in predicting heavy rainfall events. Areas of both speed and directional divergence, which are not always intuitive from wind vector analysis charts, contribute to the magnitudes of divergence and vertical velocities. Differences between convergence and divergence areas and between upward and downward vertical motion areas are more readily seen on charts graphically displaying these values. However, wind vector analysis charts illustrate features associated with the divergence and vertical velocities by graphically displaying the magnitude and direction of the ageostrophic flow.

Although Appendix C imparts invaluable knowledge for predicting excessive rainfall, forecasters must take into account additional factors that contribute to extreme convective events. Instability, moisture availability, system progression on radar and satellite imagery, local terrain, and time of year are all factors that forecasters must analyze in addition to the

atmospheric dynamics that greatly affect formation, intensity, progression, and decay of tropical MCSs.

5.1.2. Recommendations. Despite the findings, limited databases yield higher variances among the samples, which lead to uncertainty within the results. Since civilian reporting station observations transmit irregularly and with incomplete observations, all studies need to constantly incorporate more military observations from the 25th OWS to improve the capability of forecasting at the main forward deployed location east of the Andes, Apiay AB. In addition, forecasters at weather forecast centers and deployed locations need to constantly document significant features (local and synoptic) affecting each location's weather regime and incorporate them into case studies and future research. Finally, since this research only based probabilities from observed precipitation events, further research is needed for verification of probabilities of low ceilings and visibilities for forecasted precipitation events.

Further research is necessary to validate the excessive rainfall results presented in this study. Forecasters should consistently document distinctive features associated with excessive rainfall events for incorporation into case studies. Moreover, incorporating higher resolution models could improve the divergence and vertical velocity values, especially if the resolution of observed upper-air data increases. Also, precipitation observations from both surface observations and the Tropical Rainfall Measuring Mission satellite may be useful in verifying the results from improved resolution models.

5.2. Forecasting Mesoscale Convective Complex Movement in Northern Argentina, Southern Brazil, Paraguay, and Uruguay.

5.2.1. Conclusions. Corfidi et al.'s (1996) NA empirical method for predicting MCC and MCS movement also applies to forecasting SA MCC and MCS movements. MCC and MCS movement methods are based on the fact that both advective and propagation components sum to equal the movement of backward or quasi-stationary MCSs, such as MCCs (Corfidi et al. 1996; Corfidi 1998). The advective component, defined by the mean motion of individual convective cells, strongly relates to the mean 850-300 mb cloud layer flow. The propagation component, defined by the rate and location of new cell formation relative to existing cells, is related to the LLJ direction. Application of the procedure to 22 cases (20 of which were MCCs) revealed a correlation coefficient of 0.72 for the observed vs. forecasted MCC and MCS speeds and a correlation coefficient of 0.81 observed vs. forecasted MCC and MCS directions. Mean absolute errors were small enough for the forecasted MCC or MCS location to lie well within the convective system's heavy rain swath. All correlation coefficients, means, variances, and absolute errors for the SA method were comparable to those performed in producing Corfidi et al.'s (1996) NA method.

This forecast procedure is very beneficial to operational forecasters of SA. The procedure, outlined in Appendix D, will enhance prediction of the enormous convective MCCs of SA. The biggest problem in determining convective system movement is predicting new cell generation at the expense of existing cells. This procedure provides a tool to aid in predicting the often-elusive propagation component associated with MCSs. In addition, forecasters can apply this technique only knowing the speed and direction of the

mean layer wind and the LLJ. Finally, this technique will greatly aid in forecasting the location of heavy rain potential that exists with MCCs and large MCSs.

Despite the accuracy of Corfidi's method applied to both NA and SA, there are evident errors. Mesoscale and synoptic-scale systems can adversely affect the accuracy of MCC or MCS placement by altering the advective and propagation components. In addition, terrain-induced flow influences storm system movement. Moreover, this procedure requires further knowledge of the system relative convergence that may not necessarily correspond to the LLJ direction. Finally, as in Corfidi's method, this method does not apply to forward propagating systems such as bow echoes, derechoes, and squall lines (Corfidi 1998).

5.2.2. Recommendations. Although Corfidi's method greatly improves MCC and MCS movement forecasting, further research is necessary towards forecasting MCC and MCS movement for SA. This method requires application utilizing hourly radar imagery for more accurate depictions and verification of MCC and MCS movement. Also, additional knowledge of the factors that govern propagation needs investigating, as well as, terrain effects. Currently, there is a lack of knowledge of the extent that terrain features such as the Andes and Brazilian Highlands have on MCC intensity, formation, and movement. There is also a need to improve the lack of spatial resolution of the upper-air observing network over SA. Incorporating satellite-derived observations into the upper-air network and, eventually, into computer forecasting models, will greatly improve the forecasting of MCCs and MCSs. Finally, new research should discover if Corfidi's method also applies to other active MCC areas of the world, such as China.

Appendix A: Climatology of Ceilings and Visibilities following 1" of greater 24-Hour Precipitation Events

Climatology to predict ceilings and visibilities at and around 12 UTC is conditional on receiving a 24-hour accumulated rainfall ≥ 1" ending at 06 UTC. Given any rainfall amount approximately one inch or greater in a 24-hour period ending by 06 UTC (approximately midnight local time) at a specific location, the tables below aid the forecaster in determining the probability of receiving conditions below a certain ceiling and visibility category for the subsequent morning. Note that probability of occurrence does not necessarily mean that ***both*** ceiling ***and*** visibility will drop below a certain category threshold. In addition, if the rainfall event ends early in the day, enough drying and diurnal heating could take place to lower the probability of occurrence of falling into a certain ceiling and visibility category. Likewise, any rainfall event ending at night could increase the probabilities. The frequency of occurrences is an average of all sampled 1-2" rainfall events (1995-2001) encompassing all times and all seasons.

Table A1: Climatology of airfield minimum categories for 12 UTC following 1" or greater 24-hour accumulated precipitation for Benjamin Constant, Brazil (based on 141 occurrences).

Ceilings (ft) / Visibility (sm) Categories	Frequency of Occurrence (%)
Less than 3000 / 3	96.5
Less than 1500 / 3	95.7
Less than 1000 / 2	73.8
Less than 300 / 1	53.2
Less than 200 / 0.5	29.8

Table A2: Climatology of airfield minimum categories for 12 UTC following 1" or greater 24-hour accumulated precipitation for Iquitos, Peru (based on 168 occurrences).

Ceilings (ft) / Visibility (sm) Categories	Frequency of Occurrence (%)
Less than 3000 / 3	73.8
Less than 1500 / 3	72.0
Less than 1000 / 2	50.0
Less than 300 / 1	15.5
Less than 200 / 0.5	11.3

Table A3: Climatology of airfield minimum categories for 12 UTC following 1" or greater 24-hour accumulated precipitation for Leticia, Columbia (based on 204 occurrences).

Ceilings (ft) / Visibility (sm) Categories	Frequency of Occurrence (%)
Less than 3000 / 3	59.3
Less than 1500 / 3	57.4
Less than 1000 / 2	42.2
Less than 300 / 1	5.9
Less than 200 / 0.5	3.4

Appendix B: Climatology of Ceilings and Visibilities during Drizzle and Rain.

1. Climatology of Airfield Minimum Categories for Drizzle and Rain.

Climatology to predict ceilings and visibilities is conditional upon forecasting certain precipitation intensities. Given a certain precipitation intensity is forecasted at a specific location, the tables below aid the forecaster in determining the probability of receiving conditions below a certain ceiling and visibility category. Note that probability of occurrence does not necessarily mean that ***both*** ceiling ***and*** visibility will drop below a certain category threshold. Factors such as length of event occurrence or location with respect to a convective storm could alter the probabilities. Receiving rainfall in the stratus sector of a tropical system may not lower ceilings as much as receiving rainfall in the convective sector. The frequency of occurrences is an average of all sampled rainfall events (1995-2001) of a certain intensity encompassing all times and all seasons.

Table B1. Climatology of airfield minimum categories for precipitation intensity for Iquitos, Peru (based on 2417 occurrences).

Ceilings (ft) / Visibility (sm) Categories	Frequency of Occurrence for Drizzle (%)	Frequency of Occurrence for Light Rain (%)	Frequency of Occurrence for Moderate Rain (%)	Frequency of Occurrence for Heavy Rain (%)
≤ 3000 / 3	61.9	78.5	95.9	100
≤ 1500 / 3	54.9	69.5	92.4	100
≤ 1000 / 2	12.1	16.9	44.9	88.8
≤ 300 / 1	0.3	0.4	9.0	62.2
≤ 200 / 0.5	0.2	0.1	2.3	23.5

Table B2. Climatology of airfield minimum categories for precipitation intensity for Leticia, Columbia (based on 2630 occurrences).

Ceilings (ft) / Visibility (sm) Categories	Frequency of Occurrence for Drizzle (%)	Frequency of Occurrence for Light Rain (%)	Frequency of Occurrence for Moderate Rain (%)	Frequency of Occurrence for Heavy Rain (%)
≤ 3000 / 3	69.6	78.7	93.3	100
≤ 1500 / 3	66.3	76.2	91.0	98.3
≤ 1000 / 2	35.7	41.2	57.3	92.5
≤ 300 / 1	0.4	1.0	9.4	58.3
≤ 200 / 0.5	0.1	0.2	2.0	16.7

Table B3. Climatology of airfield minimum categories for precipitation intensity for Apiay AB, Columbia (based on 260 occurrences)*.

Ceilings (ft) / Visibility (sm) Categories	Frequency of Occurrence for Drizzle (%)	Frequency of Occurrence for Light Rain (%)	Frequency of Occurrence for Moderate Rain (%)	Frequency of Occurrence for Heavy Rain (%)
≤ 3000 / 3	3.8	24.6	85.3	100
≤ 1500 / 3	< 0.1	10.3	61.8	88.0
≤ 1000 / 2	< 0.1	3.4	32.4	88.0
≤ 300 / 1	< 0.1	< 0.1	< 0.1	52.0
≤ 200 / 0.5	< 0.1	< 0.1	< 0.1	< 0.1

*** CAUTION:** Use with caution due to limited observational database.

2. Climatology of Ceilings and Visibilities for Drizzle and Rain.

Climatology to predict ceilings and visibilities is conditional upon forecasting certain precipitation intensities. Given a certain precipitation intensity is forecasted at a specific location, the tables below aid the forecaster in determining the ceiling and visibility for a specific location. The tables don't yield specific ceilings and visibilities, only a range of ceilings and visibilities that would occur in concert with drizzle and rain. Ceilings ***only*** represent the lowest reportable ceiling. This guide does not aid the forecaster in predicting multiple ceilings. Due to a limited database, use Apiay AB results with caution. Results are an average of all sampled rainfall events (1995-2001) of a certain intensity encompassing all times and all seasons.

2.1. Explanation of terms.

Frequency Below Ceiling/Visibility: This is the frequency of receiving a ceiling or visibility equal to or below the value given in the following columns. The 0% and 100% thresholds are the minimum and maximum values recorded in that specific field. The range between the 10% and 90% thresholds approximately represent the middle 80% of occurrences for that specific precipitation intensity and location. In other words, this middle range represents approximately an 80% chance of a ceiling or visibility falling within the range. For ceilings, the 10% and 90% thresholds only apply for the lower range (0 - 5999 ft).

Lower Range: This is the lower range of ceilings (0 - 5999 ft).

Lower Range Frequency: This frequency represents how often the forecaster can expect to fall in the lower range of ceilings versus the upper range. This range applies most of the time, but specifically if forecasting steady precipitation or a convective storm over a station versus vicinity showers.

Upper Range: This is the upper range of ceilings (6000 - 20,000 ft).

Upper Range Frequency: This frequency represents how often the forecaster can expect to fall in the upper range of ceilings versus the lower range. This range applies if forecasting precipitation and the convective storm is not overhead, rather in the vicinity or approaching. This range also applies if forecasting precipitation in the trailing stratified sector of a tropical system. Finally, this range applies if forecasting very light rain, very light drizzle, intermittent drizzle or intermittent light rain versus steady light rain or steady drizzle.

CAUTION: Low ceilings can still occur, though not likely, with very light precipitation. Forecasters must consider all meteorological factors.

2.2. Iquitos, Peru.

Table B4. Climatological ceilings for drizzle for Iquitos, Peru. Lower and upper range frequencies are based on 594 and 356 occurrences respectively.

	Lower Range Frequency: 62.5 %	**Upper Range Frequency: 37.5%**
Frequency (%) at or below Ceiling	**Ceiling (ft)-Lower Range**	**Ceiling (ft)-Upper Range**
0%	0	7000
10%	760	-
90%	1560	-
100%	4000	15,000
Forecaster Tidbit: 96% probability ceilings 10,000 ft or lower in Upper Range		

Table B5. Climatological visibilities for drizzle for Iquitos, Peru (based on 950 occurrences).

Frequency (%) at or below Visibility	Visibility (sm)
0%	1/2
10%	3
90%	7
100%	7
Forecaster Tidbit: Only 5% probability visibility less than 3 miles	

Table B6. Climatological ceilings for light rain for Iquitos, Peru. Lower and upper range frequencies are based on 692 and 243 occurrences respectively.

	Lower Range Frequency: 74.0%	**Upper Range Frequency: 26.0%**
Frequency (%) at or below Ceiling	**Ceiling (ft)-Lower Range**	**Ceiling (ft)-Upper Range**
0%	0	7000
10%	700	-
90%	1500	-
100%	3100	15,000
Forecaster Tidbit: 98% probability ceilings 10,000 ft or lower in Upper Range		

Table B7. Climatological visibilities for light rain for Iquitos, Peru (based on 935 occurrences).

Frequency (%) at or below Visibility	Visibility (sm)
0%	5/8
10%	2 1/2
90%	5
100%	7
Forecaster Tidbit: 22% probability visibility less than 3 miles	

Table B8. Climatological ceilings for moderate rain for Iquitos, Peru. Lower and upper range frequencies are based on 370 and 64 occurrences respectively.

	Lower Range Frequency: 85.3%	**Upper Range Frequency: 14.7%**
Frequency (%) at or below Ceiling	**Ceiling (ft)-Lower Range**	**Ceiling (ft)-Upper Range**
0%	300	7000
10%	700	-
90%	1300	-
100%	2000	10,000
Forecaster Tidbit: 94% probability ceiling 7000 - 8000 ft in Upper Range		

Table B9. Climatological visibilities for moderate rain for Iquitos, Peru (based on 434 occurrences).

Frequency (%) at or below Visibility	Visibility (sm)
0%	1/16
10%	1 1/4
90%	4 1/2
100%	7
Forecaster Tidbit: 77% probability visibility 3 miles or less	

Table B10. Climatological ceilings for heavy rain for Iquitos, Peru. Lower and upper range frequencies are based on 87 and 11 occurrences respectively.

	Lower Range Frequency: 88.8%	**Upper Range Frequency: 11.2%**
Frequency (%) at or below Ceiling	**Ceiling (ft)-Lower Range**	**Ceiling (ft)-Upper Range**
0%	100	7000
10%	600	-
90%	1300	-
100%	1500	8000
Forecaster Tidbit: Near 100% probability ceilings 7000 - 8000 ft in Upper Range		

Table B11. Climatological visibilities for heavy rain for Iquitos, Peru (based on 98 occurrences).

Frequency (%) at or below Visibility	Visibility (sm)
0%	0
10%	1/4
90%	2
100%	7
Forecaster Tidbit: 86% probability visibility 1 1/4 miles or less	

2.3. Leticia, Columbia.

Table B12. Climatological ceilings for drizzle for Leticia, Columbia. Lower and upper range frequencies are based on 772 and 346 occurrences respectively.

	Lower Range Frequency: 69.0%	**Upper Range Frequency: 31.0%**
Frequency (%) at or below Ceiling	**Ceiling (ft)-Lower Range**	**Ceiling (ft)-Upper Range**
0%	500	6000
10%	670	-
90%	1330	-
100%	4000	20,000
Forecaster Tidbit: 99% probability ceilings 15,000 ft or less in Upper Range		
Forecaster Tidbit: 85% probability ceilings 6000 - 10,000 ft in Upper Range		

Table B13. Climatological visibilities for drizzle for Leticia, Columbia (based on 1118 occurrences).

Frequency (%) at or below Visibility	**Visibility (sm)**
0%	3/8
10%	2 1/2
90%	5
100%	7
Forecaster Tidbit: Only 13% probability visibility less than 3 miles	

Table B14. Climatological ceilings for light rain for Leticia, Columbia. Lower and upper range frequencies are based on 592 and 213 occurrences respectively.

	Lower Range Frequency: 73.4%	**Upper Range Frequency: 26.6%**
Frequency (%) at or below Ceiling	**Ceiling (ft)-Lower Range**	**Ceiling (ft)-Upper Range**
0%	400	7000
10%	700	-
90%	1300	-
100%	3100	15,000
Forecaster Tidbit: 85% probability ceilings 7000 - 9000 ft in Upper Range		

Table B15. Climatological visibilities for light rain for Leticia, Columbia (based on 805 occurrences).

Frequency (%) at or below Visibility	Visibility (sm)
0%	1/4
10%	2
90%	4 1/2
100%	7
Forecaster Tidbit: 33% probability visibility less than 3 miles	

Table B16. Climatological ceilings for moderate rain for Leticia, Columbia. Lower and upper range frequencies are based on 510 and 77 occurrences respectively.

	Lower Range Frequency: 86.9%	**Upper Range Frequency: 13.1%**
Frequency (%) at or below Ceiling	**Ceiling (ft)-Lower Range**	**Ceiling (ft)-Upper Range**
0%	100	6000
10%	560	-
90%	1370	-
100%	5000	15,000
Forecaster Tidbit: 88% probability ceilings 7000 - 8000 ft in Upper Range		

Table B17. Climatological visibilities for moderate rain for Leticia, Columbia (based on 587 occurrences).

Frequency (%) at or below Visibility	Visibility (sm)
0%	1/4
10%	1
90%	4
100%	7
Forecaster Tidbit: 83% probability visibility 3 miles or less	

Table B18. Climatological ceilings for heavy rain for Leticia, Columbia. Lower and upper range frequencies are based on 115 and 5 occurrences respectively.

	Lower Range Frequency: 95.8%	**Upper Range Frequency: 4.2%**
Frequency (%) at or below Ceiling	**Ceiling (ft)-Lower Range**	**Ceiling (ft)-Upper Range**
0%	400	8000
10%	600	-
90%	1500	-
100%	1700	8000
Forecaster Tidbit: Near 100% probability ceilings around 8000 ft in Upper Range		

Table B19. Climatological visibilities for heavy rain for Leticia, Columbia (based on 120 occurrences).

Frequency (%) at or below Visibility	Visibility (sm)
0%	1/16
10%	1/4
90%	2 1/2
100%	7
Forecaster Tidbit: 80% probability visibility 1 1/4 miles or less	

2.4. Apiay Air Base, Columbia.

Table B20. Climatological ceilings for drizzle for Apiay AB, Columbia. Lower and upper range frequencies are based on 10 and 16 occurrences respectively*.

	Lower Range Frequency: 38.5%	Upper Range Frequency: 61.5%
Frequency (%) at or below Ceiling	**Ceiling (ft)-Lower Range**	**Ceiling (ft)-Upper Range**
0%	2000	6500
10%	3000	-
90%	5500	-
100%	5500	13,000

*** CAUTION:** Use with caution due to limited observational database.

Table B21. Climatological visibilities for drizzle for Apiay AB, Columbia (based on 26 occurrences)*.

Frequency (%) at or below Visibility	Visibility (sm)
0%	3
10%	5
90%	7
100%	7
Forecaster Tidbit: Only 4% probability visibility of 3 miles	

*** CAUTION:** Use with caution due to limited observational database.

Table B22. Climatological ceilings for light rain for Apiay AB, Columbia. Lower and upper range frequencies are based on 123 and 52 occurrences respectively.

	Lower Range Frequency: 70.3%	**Upper Range Frequency: 29.7%**
Frequency (%) at or below Ceiling	**Ceiling (ft)-Lower Range**	**Ceiling (ft)-Upper Range**
0%	500	6000
10%	1300	-
90%	4800	-
100%	5500	14,000
Forecaster Tidbit: 34% probability ceilings less than 3000 ft in Lower Range		

Table B23. Climatological visibilities for light rain for Apiay AB, Columbia (based on 175 occurrences).

Frequency (%) at or below Visibility	**Visibility (sm)**
0%	1 1/2
10%	4
90%	7
100%	7
Forecaster Tidbit: Only 2% probability visibility less than 3 miles	

Table B24. Climatological ceilings for moderate rain for Apiay AB, Columbia**.** Lower and upper range frequencies are based on 34 and 0 occurrences respectively*.

	Lower Range Frequency: 100%	**Upper Range Frequency: 0%**
Frequency (%) at or below Ceiling	**Ceiling (ft)-Lower Range**	**Ceiling (ft)-Upper Range**
0%	400	-
10%	1000	-
90%	4300	-
100%	5500	-
Forecaster Tidbit: 71% probability ceilings 3000 ft or less in Lower Range		

*** CAUTION:** Use with caution due to limited observational database.

Table B25. Climatological visibilities for moderate rain for Apiay AB, Columbia (based on 34 occurrences)*.

Frequency (%) at or below Visibility	Visibility (sm)
0%	3/4
10%	1 1/2
90%	4
100%	7
Forecaster Tidbit: 77% probability visibility 3 miles or less	

*** CAUTION:** Use with caution due to limited observational database.

Table B26. Climatological ceilings for heavy rain for Apiay AB, Columbia**.** Lower and upper range frequencies are based on 25 and 0 occurrences respectively*.

	Lower Range Frequency: 100%	**Upper Range Frequency: 0%**
Frequency (%) at or below Ceiling	**Ceiling (ft)-Lower Range**	**Ceiling (ft)-Upper Range**
0%	200	-
10%	800	-
90%	3300	-
100%	4900	-
Forecaster Tidbit: 80% probability ceilings 2000 ft or less in Lower Range		

*** CAUTION:** Use with caution due to limited observational database.

Table B27. Climatological visibilities for heavy rain for Apiay AB, Columbia (based on 25 occurrences)*.

Frequency (%) at or below Visibility	Visibility (sm)
0%	1/2
10%	1/2
90%	1 1/2
100%	4
Forecaster Tidbit: 72% probability visibility 1 mile or less	

*** CAUTION:** Use with caution due to limited observational database.

Appendix C: Dynamical Guidelines to Forecasting Excessive Rainfall Events during the Wet Season

This appendix aids forecasters in predicting excessive rainfall (generally 6" or greater in 24 hours) for Columbia, Ecuador, Northern Peru, and Northwest Brazil east of the Andes. This forecasting tool is especially useful for large-scale events (length or width of cloud shield is 350 nm or greater) during the wet season. First, forecasters must closely monitor large-scale convective development east of Columbia and Northern Peru, in particular, development occurring along the Near Equatorial Trough (NET) and just inland of the northeastern coast of South America (developing squall lines). Forecasters then should carefully analyze current and available model wind vector analysis charts at all levels from the surface to 300 mb prior to making a forecast. Graphical workstations can display wind vector analysis charts from data ingested from model analysis (e.g. AVN or MM5). Tables C1 and C2 list common features seen on wind vector analyses charts that precursor heavy rainfall events. Figs. C1 through C4 help to illustrate the forecaster guidelines presented in Tables C1 and C2.

Precursor heavy rainfall features often yield strong convergence, divergence, and upward vertical velocities. Low-level convergence typically causes upward vertical motions while upper-level divergence aids the outflow from storms, which indirectly triggers upward vertical motions. Convergence and divergence are attributed either to directional convergence or divergence, speed convergence or divergence, or a combination of both direction and speed convergence or divergence; therefore, forecasters must carefully look for ***both*** speed and directional convergence and divergence on wind vector analysis charts. To most accurately view magnitudes of divergence and upward vertical velocities, forecasters

must analyze constant pressure charts from 850 to 300 mb. These charts are available from model analyses. As in wind vector analyses, graphical workstations can display divergence and vertical velocity values from data ingested into the workstation from model analyses (e.g. AVN or MM5). Forecasters should look for areas of maximum convergence at 850 and 700 mb and areas of maximum divergence occurring in the same locations at 500, 400, and 300 mb. In addition, forecasters should examine 700 and 500 mb charts for strong upward vertical velocities in the same locations as low-level convergence and upper-level divergence. If the areas of maximum convergence, maximum divergence, and maximum vertical velocities nearly line up with one another, then forecasters should consider these areas as a potential for an excessive rainfall occurrence. Finally, forecasters should pay attention to important precursory information listed in Table C3.

CAUTION: Not all features listed in Tables C1 and C2 need be present for excessive rainfall events. Due to model analysis spatial resolution constraints, the dynamics present for a heavy rainfall event may create such a storm near the desired location but missing the desired location; therefore, forecasters must closely monitor intensity changes and movement on satellite imagery. In addition, storms may not produce rainfall greater than 6", but rather an amount approximate to 6". Figures and Tables in this appendix do not take into account moisture availability or instability effects in the mid to upper-levels; therefore, forecasters ***must*** analyze all data available to include localized effects. This appendix only serves, as one of many guidance tools forecasters should examine in producing rainfall forecasts.

Table C1: Dynamical features leading to excessive rainfall (approximately 6" or greater) during the wet season (Mar-Nov) for locations north of the Equator. Refer to Figs. C1 and C2. Applicable levels are in parentheses**.**

- Strong convergence into the Near Equatorial Trough (1000 & 850 mb)
- North Atlantic High extending to the Southern Caribbean Sea or Venezuela which increases the pressure gradient between the North Atlantic High and the South Atlantic High (1000, 850, 700, 500, 400 & 300 mb)
- Increased gradient between South Atlantic and North Atlantic highs creating stronger speed convergence of the trade winds (850 & 700 mb)
- Easterly wind max from increased pressure gradient of 25 to 40 kts (700 mb)
- Venezuelan Highlands altering the low-level flow creating convergence over Western Venezuela and Eastern Columbia (1000 & 850 mb)
- Increased low-level easterly flow creating more uplift east of Andes (1000, 850 & 700 mb)
- Migrating Amazon lows (lows are weaker from May-Oct but still present) moving convergence boundaries and enhancing convection (1000 & 850 mb)
- Divergence in easterly flow southwest of North Atlantic High extension (500, 400 & 300 mb)
- Divergence on westward edge of troughs (waves) in easterly flow (500, 400 & 300 mb)
- Smaller meso-scale circulations creating convergence boundaries (1000, 850 & 700 mb)
- Smaller perturbation upper-level highs and lows creating localized divergence (500, 400 & 300 mb)

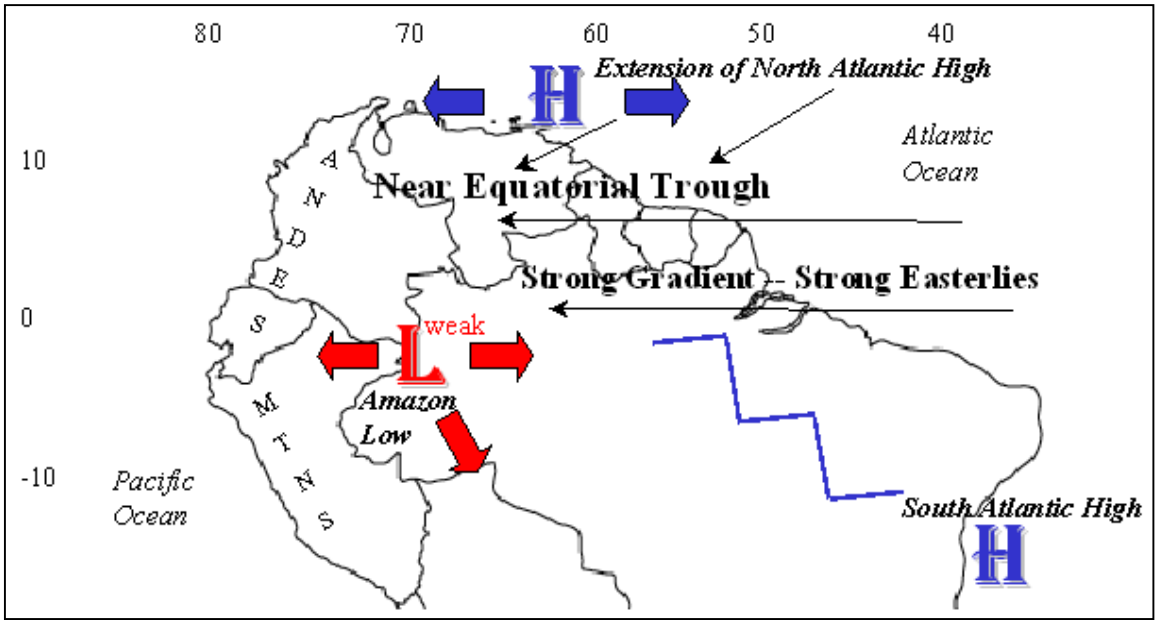

Fig. C1. Surface to 700 mb features during excessive rainfall events for locations north of the Equator during the wet season (Mar-Nov). Arrows approximately represent the extent of location variability during heavy rainfall events. This figure corresponds to the guidelines listed in Table C1.

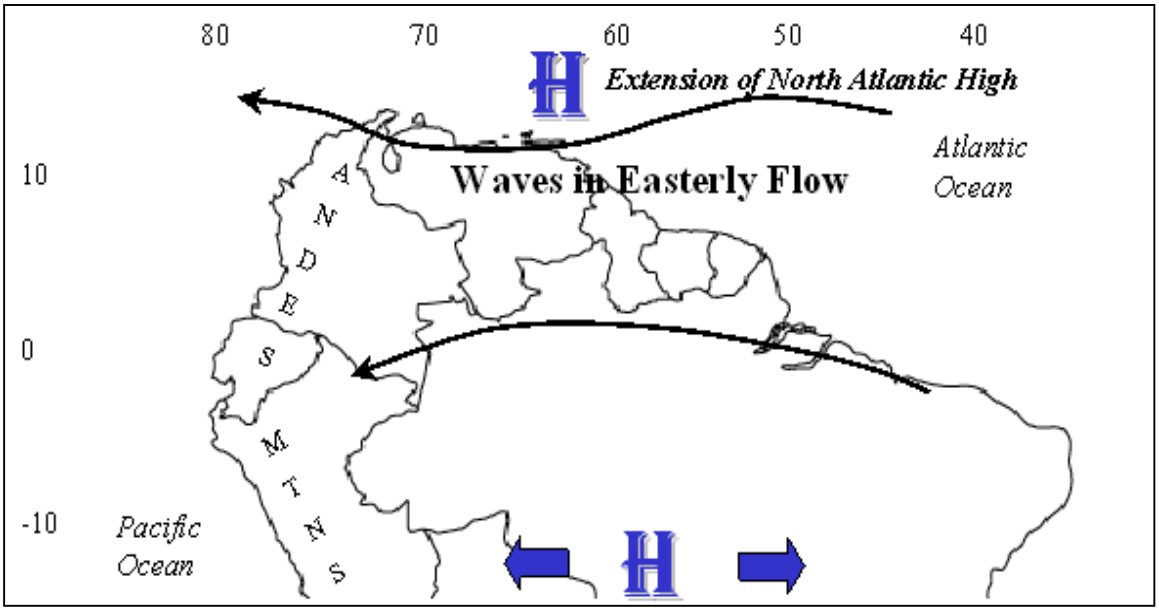

Fig. C2. 500 to 300 mb features during excessive rainfall events for locations north of the Equator during the wet season (Mar-Nov). Arrows approximately represent the extent of location variability during heavy rainfall events. This figure corresponds to the guidelines listed in Table C1.

Table C2: Dynamical features leading to excessive rainfall (approximately 6" or greater) during the wet season (Sep-Jun) for locations south of the Equator. Refer to Figs. C3 and C4. Applicable levels are in parentheses**.**

- Strong convergence into the Near Equatorial Trough (1000 & 850 mb)
- South Atlantic High strengthening and ridging to the west into Brazil (1000, 850, 700 & 500 mb)
- Increased convergence into the South Atlantic Convergence Zone (SACZ) (1000, 850 & 700 mb)
- Low-level flow following the terrain (Andes) helping to create the Amazon Low (1000 & 850 mb)
- Migrating Amazon Low moving convergence boundaries and enhancing convection (1000 & 850 mb)
- Increasing easterly wind max from increased pressure gradient (flow is weakest from Nov-Mar but still present) (700 mb)
- Divergence associated with troughs (waves) in westerly flow (500, 400 & 300 mb)
- Flow around Bolivian High and trough over Eastern Brazil enhancing divergence (500, 400 & 300 mb)
- Deformation zones over the Western Amazon Basin enhancing divergence (500, 400 & 300 mb)
- Smaller meso-scale circulations creating convergence boundaries (1000, 850 & 700 mb)
- Smaller perturbation upper-level highs and lows that may create localized divergence (500, 400 & 300 mb)

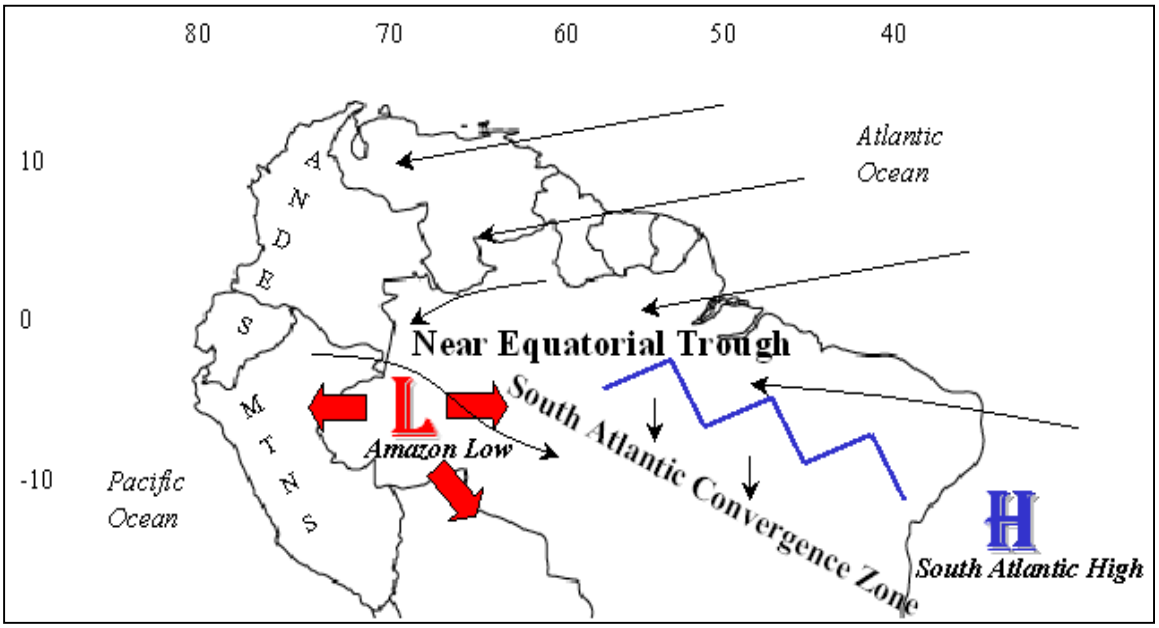

Fig. C3. Surface to 700 mb features during excessive rainfall events for locations south of the Equator during the wet season (Sep-Jun). Arrows approximately represent the extent of location variability during heavy rainfall events. This figure corresponds to the guidelines listed in Table C2.

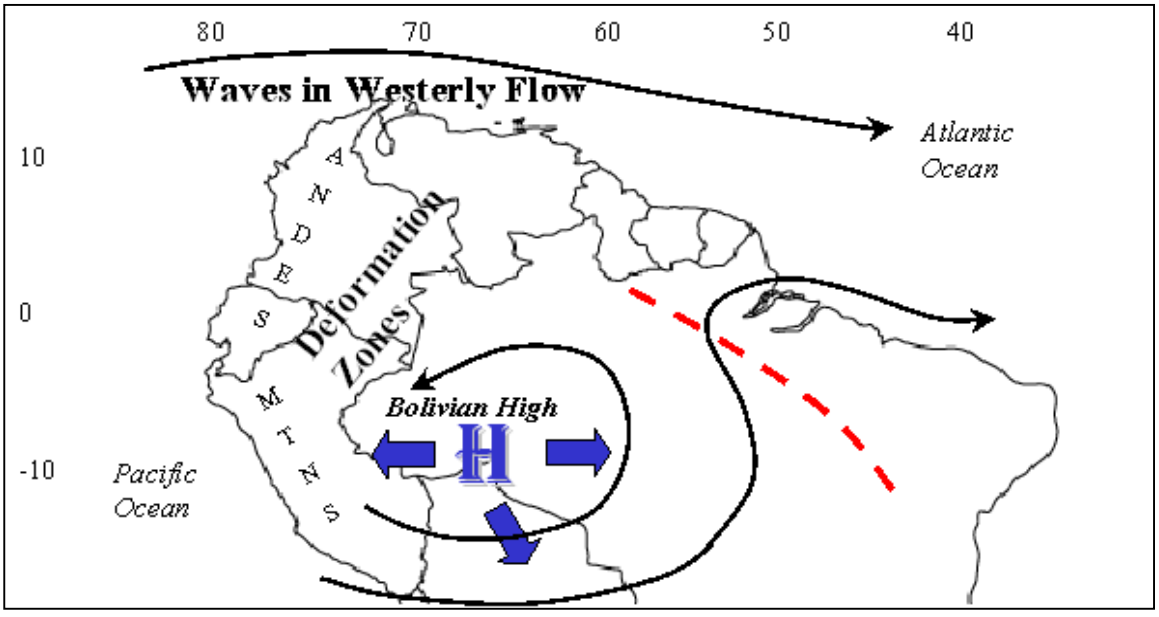

Fig. C4. 500 to 300 mb features during excessive rainfall events for locations south of the Equator during the wet season (Sep-Jun). Arrows approximately represent the extent of location variability during heavy rainfall events. This figure corresponds to the guidelines listed in Table C2.

Table C3. Predictors for excessive rainfall events (approximately 6" or greater) using divergence and vertical velocities.

- Search all levels for upper-level divergence. Although the level of strongest divergence typically occurs at 400 mb, it may occur at 300 mb for very strong storms or 500 mb for weaker storms or storms that are in a weakening stage

- Carefully analyze both 850 and 700 mb divergence fields north of the equator for an eastward tilt of maximum convergence with height. The horizontal difference in the two fields is normally 100 – 200 nm. 700 mb acts as the level of rear inflow into the storm

- Look for the strongest convection with squall lines north of the equator to occur between the 850 and 700 mb convergence areas

- Look for the maximum upper-level divergence to lie nearly above the maximum 700 mb convergence for all locations

- Keep in mind diurnal differences. There is over a 90% chance of excessive rainfall events north of the equator occurring around 00Z versus 12Z. Time of day is not as significant south of the equator in the Western Amazon Basin

- Approximately 90% of excessive rainfall events north of the Equator are associated with squall lines while most excessive rainfall events south of the equator are not associated with squall lines

CAUTION: Table C4 displays results from data gathered in this research (explained in more detail in Section 4.1.3.2.). Due to severe model resolution constraints, the divergence and vertical velocity values presented in table C4 are not realistic; therefore ***Table C4 should not be used in producing rainfall forecasts***. The actual divergence and vertical velocity values may be two to four or more times higher than those shown in Table C4.

Table C4. Divergence and upward vertical velocity values for excessive rainfall events (approximately 6" or greater). All values mentioned must be associated with storms equal or greater than 350 nm in length or width. Values may be much greater for individual elements within a mesoscale convective system. Negative divergence values represent convergence.

Geographical Area	Locations north of the Equator	Locations south of the Equator
850 mb divergence	-2×10^{-5} s^{-1} or less	-1.5×10^{-5} s^{-1} or less
700 mb divergence	-1.75×10^{-5} s^{-1} or less	-2.25×10^{-5} s^{-1} or less
Strongest upper-level divergence (usually 400 mb)	2×10^{-5} s^{-1} or greater	2×10^{-5} s^{-1} or greater
Difference of strongest low-level and upper-level divergence	4×10^{-5} s^{-1} or greater	4×10^{-5} s^{-1} or greater
700 mb and 500 mb upward vertical velocities	3.5 cm s^{-1} or greater	3.5 cm s^{-1} or greater

Appendix D: Forecasting Movement of Mesoscale Convective Complexes in South America

Corfidi et al. (1996) proposed a solution to determine movement of MCCs in the U.S. by the simple principle that movement of mesoscale convective complexes (MCCs) is affected by both the cloud layer advection and propagation components. A very similar method can be applied to South American MCCs by utilizing the same principle. This appendix outlines the procedures in forecasting movement of MCCs along with an example. All that are required are wind vector analysis or model vector analysis charts of 850, 700, 500, and 300 mb, infrared (IR) satellite imagery, a basic scientific calculator, and a protractor (optional).

Although this procedure is accurate in predicting the movement of the MCC and its associated heavy rain shield out to about 12 hours, errors can occur. To minimize errors, this procedure should be applied at least every three hours to account for changing cloud layer wind and propagation components. These changes could alter the results of the linear, empirical technique throughout the MCCs lifespan. Moreover, this procedure applies only to MCCs and large elliptical mesoscale convective systems (MCSs) that occur south of 15º S. This procedure will not predict movement of forward propagating MCSs such as bow-echoes, derechoes, and squall lines. This procedure will not aid in forecasting the actual location of initial convection that may grow into an MCC or large MCS and the intensity of these systems nor will this aid in determining when the MCC or MCS decays. Additionally, forecasters should be aware of fronts, squall lines, and upper-level shortwaves that may add speed to the system. Moreover, forecasters should be aware of mesoscale features such as meso-highs, outflow boundaries, quasi-stationary fronts, and local terrain-induced wind

flows (e.g. katabatic flow) that could alter propagation. Forecasters should also examine the amount of moisture in the atmosphere. MCCs and large MCSs tend to propagate toward the region of higher dewpoints and precipitable water. Finally, an MCS that exhibits potential to blossom into an MCC must first be present to forecast movement.

Procedure.

1) Locate the MCC or MCS on satellite imagery. Locate the area of coldest cloud tops within the system using IR imagery. Note the latitude, longitude, and time of the system.
2) Find the same location on 850, 700, 500, and 300 mb wind vector analysis charts. The charts should be within six hours of MCC or MCS observation (step 1). If the 00 UTC charts aren't available, then proceed with the 12 UTC analysis charts or 00 UTC wind vector model charts. The process ***must*** be updated once the 00 UTC wind vector analysis charts are available. Rawinsonde soundings may substitute wind vector analysis charts if the sounding is located within 50 nm of the MCC or MCS location. A workstation and graphical display system can generate the wind vector analysis or model charts. Note the speed (knots) and direction (degrees) of the wind at each level. NOTE: North is 360º, not 000º.

3) Locate the maximum wind speed of the low-level jet on the 850 mb wind vector analysis chart. The maximum wind speed should be within 100 nm upwind of the MCC or MCS location (step 1). Note the speed (knots), V_{LLJ}, and direction (degrees), DIR_{LLJ}, of this jet (may differ slightly from the speed and direction found in step 2).

4) Calculate the magnitude of the advective component (or cloud layer mean wind speed) of the system from equation D1. Substitute the wind speeds found in step 2 into equation D1 to find the mean wind speed in the 850-300 mb layer, V_{CL}, associated with the MCC or MCS. V_{850}, V_{700}, V_{500}, and V_{300} represents the wind speeds at 850, 700, 500, and 300 mb respectively. Round the result to the nearest tenth of knot.

$$V_{CL} = \frac{(V_{850} + V_{700} + V_{500} + V_{300})}{4} \qquad \text{(D1)}$$

5) Compute the direction of the advective component (or cloud layer mean wind direction) of the system from equation D2. Substitute the wind directions found in step 2 into equation D2 to find the mean wind direction in the 850-300 mb layer, DIR_{CL}, associated with the MCC or MCS. DIR_{850}, DIR_{700}, DIR_{500}, and DIR_{300} represents the wind directions at 850, 700, 500, and 300 mb respectively. Round the result to the nearest full degree. NOTE: If the DIR_{850} or DIR_{700} is between 001º and 180º, then it is necessary to add 360º to the either term or both terms before inserting them into equation D2. Again, north is 360º, not 000º.

$$DIR_{CL} = \frac{(DIR_{850} + DIR_{700} + DIR_{500} + DIR_{300})}{4} \qquad \text{(D2)}$$

6) Determine the angle, β (Beta), between the mean cloud layer and propagation components (Fig. D1) from equation D3. The propagation is simply the inverse of the low-level jet (Fig. D1). The two are 180º different from each other and exhibit the same magnitude. Simply insert the mean cloud layer direction, DIR_{CL}, found in step 5 and the direction of the low-level jet, DIR_{LLJ}, found in step 3 into equation D3. NOTE: If the DIR_{LLJ} or DIR_{CL} is between 001º and 180º, then it is necessary to add 360º to either term or both terms before inserting them into equation D3.

$$\beta = (360 - DIR_{CL}) - (360 - DIR_{LLJ}) \qquad \text{(D3)}$$

7) Calculate the speed of the MCC or MCS from equation D4. Insert the speed of the mean cloud layer, V_{CL}, found in step 4, the speed of the low-level jet, V_{LLJ}, found in step 3, and the β (Beta) angle found in step 6 into equation D4. The result, V_{MCC}, yields the predicted speed (knots) of the MCC or MCS. Fig. D1 graphically illustrates the forecasted MCC vector component.

$$V_{MCC} = \sqrt{(V_{CL})^2 + (V_{LLJ})^2 - 2(V_{CL})(V_{LLJ})\cos(\beta)} \qquad \text{(D4)}$$

8) Determine the angle, α (alpha), between the mean cloud layer and the projected MCC components (Fig. D1) from equation D5. Insert the speed of the mean cloud layer, V_{CL}, the speed of the low-level jet, V_{LLJ}, and the predicted speed of the MCC or MCS, V_{MCC}, found in the previous step into equation D5. After subtracting, multiplying, and dividing the terms in brackets, calculate the inverse cosine, arccos, of the term in brackets.

$$\alpha = \arccos\left[\frac{(V_{LLJ})^2 - (V_{MCC})^2 - (V_{CL})^2}{-2(V_{MCC})(V_{CL})}\right] \qquad \text{(D5)}$$

9) Compute the actual direction that the MCC or MCS is heading towards by performing equation D6. Insert the direction of the cloud layer, DIR_{CL}, found in step 5 and the α (alpha) angle found in the previous step into equation D6. NOTE: If the DIR_{CL} is between 001º and 180º, then it is necessary to add 360º to the DIR_{CL} before inserting it into equation D6. The final result is the predicted direction (degrees) in which the MCC or MCS is heading towards.

$$DIR_{MCC} = DIR_{CL} - 180 - \alpha \qquad \text{(D6)}$$

10) Steps 7 and 9 yield the projected speed and direction of the MCC or MCS respectively. When converting knots to distance on a map, remember that 60 nm equals one degree latitude. Multiply the predicted speed by the number of hours into the future you wish to forecast for. For example a speed of 30 knots for 6 hours will produce a 180 nm distance, which is equivalent to 3 degrees latitude. On a chart of South America (typically Lambert Conformal or Mercator projections), measure 3 degrees latitude with a ruler. Then, put the beginning of the ruler on the location of observation of MCC or MCS (same location found in step 1). The ending distance measured for 3 degrees corresponds to the projected location of the MCC or MCS in six hours. Remember, that the ruler must lay in the same direction calculated in step 9. Display the exact heading onto the map with a protractor, or estimate the heading onto the map.

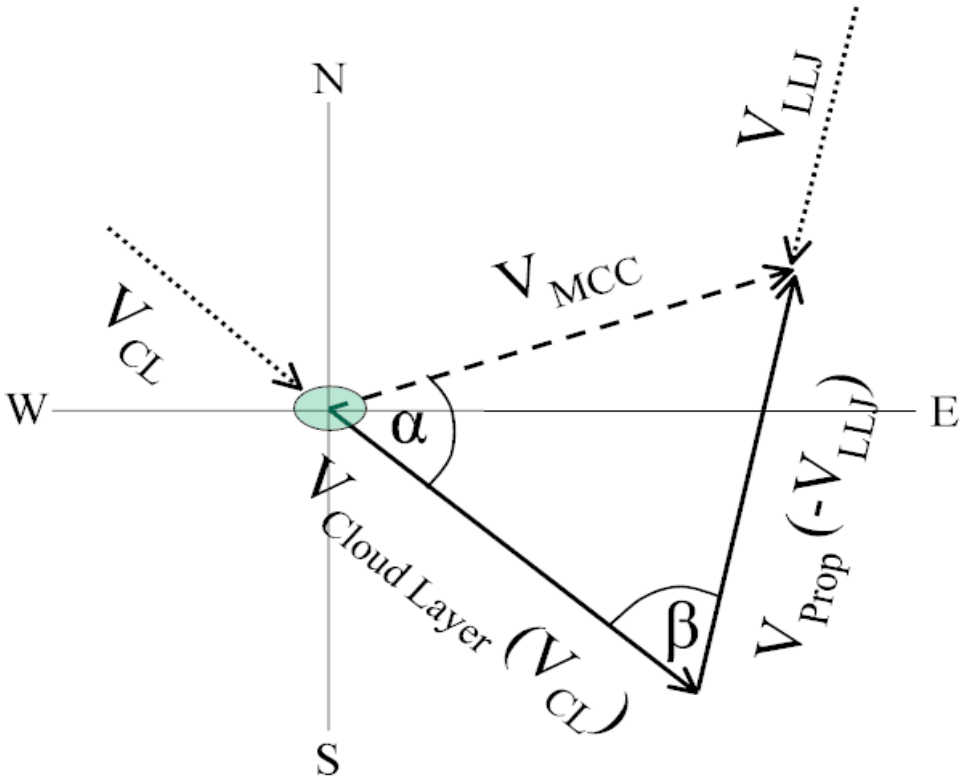

Fig. D1. Conceptual model of the vector components and angles used to predict MCC or MCS velocity, V_{MCC}. The magnitude and direction of the propagation component, V_{PROP} are equal and opposite to the low-level jet, V_{LLJ}. Angles α and β are related to the forecasted MCC or MCS direction and are calculated in equations D5 and D3 respectively. The V_{MCC} vector component is the forecasted component of the MCC or MCS motion. V_{MCC}, calculated in equation D4, is the vector sum of the V_{CL} and V_{PROP} components. The circle at the intersection of the E-W and N-S axes denotes the starting MCC or MCS location.

Example.

1) Coordinates of circular-looking cells on satellite imagery that have coagulated into a larger MCS are 30º S and 60º W. Formation of MCS occurred at 0000 UTC.

2) Speeds and directions of winds from vector analysis charts are as follows: V_{850}=25, V_{700}=20, V_{500}=15, V_{300}=60; DIR_{850}=005º (or 365º), DIR_{700}=325º, DIR_{500}=280º, DIR_{300}=280º. Speeds are in knots.

3) Low-level jet maximum at 850 mb is 30 knots from 010º (or 370º).

4) Mean cloud layer speed computed from equation D1 is 30.0 knots.

5) Mean cloud layer direction computed from equation D2 is from 312º.

6) β angle calculated from equation D3 is 58º (Fig. D2). The V_{LLJ} term is actually 370º since the angle is between 001º and 180º.

7) Predicted MCC speed calculated from equation D4 is 29.0 knots. Fig. D2 graphically illustrates the forecasted vector component.

8) α angle calculated from equation D5 is 61º (Fig. D2).

9) Predicted MCC direction computed from equation D6 is 071º.

10) The MCC is forecast to head towards 071º (or east northeastward) at 29 knots (Fig. D2). In six hours, the MCC is forecasted to travel 174 nm (29 knots x 6 hours). 174 nm is equal to 2.9 degrees latitude (174 nm / 60 nm) or approximately 3 degrees latitude. After measuring the distance and angle onto a South American map, this corresponds to a forecasted position at 0600 UTC of 29.0º S and 56.5º W.

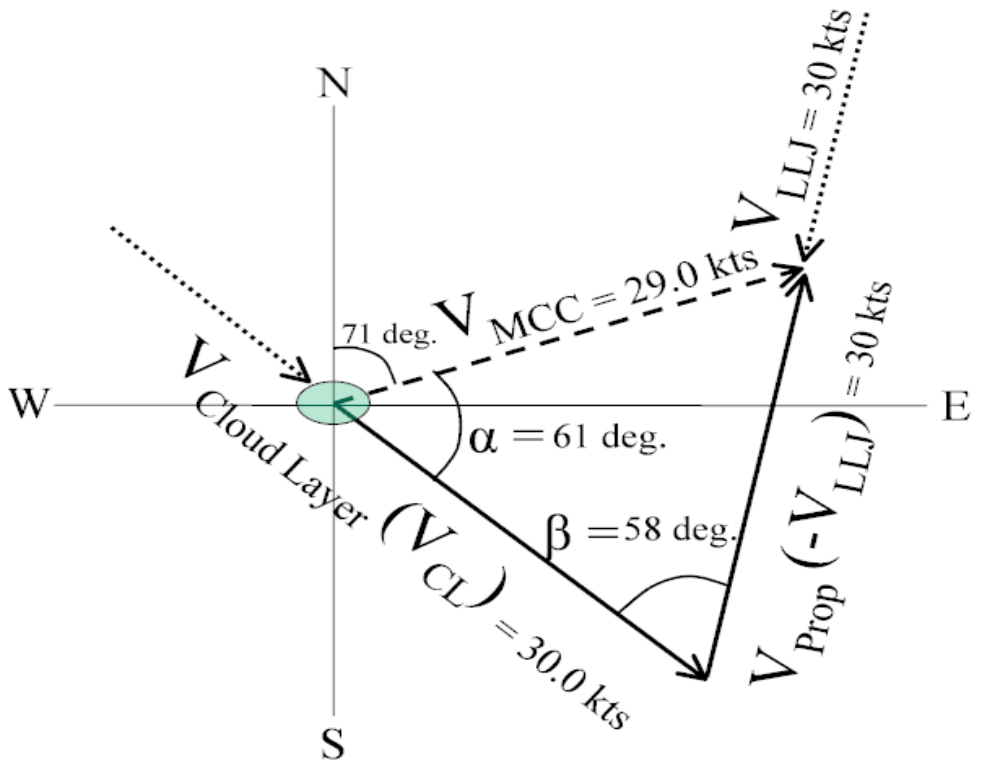

Fig. D2. Example of a conceptual model of the vector components and angles used to predict MCC or MCS velocity, V_{MCC}. The magnitude and direction of the propagation component, V_{PROP} are equal and opposite to the low-level jet, V_{LLJ}. Angles α (61º) and β (58º) are calculated in equations D5 and D3 respectively. The V_{MCC} vector component (29.0 knots), the forecasted component of the MCC or MCS motion, is calculated in equation D4. The angle (71º), computed in equation D6, is the direction in which the MCC is heading towards. The circle at the intersection of the E-W and N-S axes denotes the starting MCC or MCS location.

Bibliography

Air Force Combat Climatology Center (AFCCC), 1995-2001. Observation Data. [Available from AFCCC/DOC4, 151 Patton Avenue, Asheville, NC 28801-5002]

_____, cited 2002: Operational Climatic Data Summary. [Available online at http://www.afccc.af.mil]

Baetghen, W, V. Barros, E. H. Berbery, R. Clarke, H. Cullen, C. Ereno, B. Grassi, D. Lettenmaier, C. R. Mechoso, and P. Silva-Dias, cited 2002: Climatology and Hydrology of the Plata Basin: A Document of VAMOS Scientific Study Group on the Plata Basin. [Available online at http://www.atmos.ucla.edu/~mechoso/laplata3.html]

Bonner, W. L., 1968. Climatology of the Low-Level Jet. *Mon. Wea. Rev.,* **96**, 833-850.

Cohen, J. C. P., M. A. F. Silva-Dias and C. A. Nobre, 1995. Environmental Conditions Associated with Amazonian Squall Lines: A Case Study. *Mon. Wea. Rev.,* **123**, 3163-3174.

Cooperative Institute for Research in the Atmosphere (CIRA), Colorado State University, cited 2002. [Available from CIRA, Colorado State University, Foothills Campus, Fort Collins, CO 80523]

Corfidi, S. F., J. M. Fritsch, and J. H. Merritt, 1996: Predicting the Movement of Mesoscale Convective Complexes. *Wea. Forecasting.,* **11**, 41-46.

_____, 1998: Forecasting MCS Mode and Motion. [Available online at http://www.spc.noaa.gov/publications/corfidi/mcs_mode.htm]

Davison, M., 1999a: Climate Control Features - South America. [Available from International Desks, National Centers for Environmental Prediction, Hydrometeorological Prediction Center/Development and Training Branch, 5200 Auth Rd., Camp Springs, MD 20746.]

_____, 1999b: Mesoscale Systems over South America. [Available from International Desks, National Centers for Environmental Prediction, Hydrometeorological Prediction Center/Development and Training Branch, 5200 Auth Rd., Camp Springs, MD 20746.]

_____, 2002: Mesoscale Convective Case Studies. [Available from International Desks, National Centers for Environmental Prediction, Hydrometeorological Prediction Center/Development and Training Branch, 5200 Auth Rd., Camp Springs, MD 20746.]

Department of the Air Force (DAF). *Surface Weather Observations.* AFMAN 15-111. Washington: HQ USAF, 1 Nov 1998.

Devore, J. L., 2000: *Probability and Statistics for Engineering and the Sciences*, 5th Ed. Duxbury Thomas Learning, 775 pp.

Douglas, M., M. Nicolini, and C. Saulo, cited 2002: The Low-Level Jet at Santa Cruz, Bolivia during January-March 1998 Pilot Balloon Observations and Model Comparisons, 10 pp. [Available online at http://www.nssl.noaa.gov/projects/pacs/preprints/LLJBolivia.html]

Ebeling, C. E., 1997: *An Introduction to Reliability and Maintainability Engineering.* McGraw Hill, 486 pp.

Edson, R. T., and P. M. Condray, 1989: *The Caribbean Basin – An Electrooptical Climatology for the 8-12 Micron Band.* Vol 3, USAFETAC/TN-89/006, USAF Environmental Technical Applications Center.

Fleet Numerical Meteorological and Oceanography Detachment (FNMOD), 2001-2002: Fleet Historical Fields Display System. [Available online at http://navy.ncdc.noaa.gov/products/online.html]

Gamache, J. F. and R. A. Houze, Jr., 1982: Mesoscale Air Motions Associated with a Tropical Squall Line. *Mon. Wea. Rev.,* **110**, 118-135.

Garreaud, R. D. and J. M. Wallace., 1998: Summertime Incursions of Midlatitude Air into Subtropical and Tropical South America. *Mon. Wea. Rev.,* **126**, 2713-2733.

Garstang, M., H. L. Massie Jr., J. Halverson, S. Greco and J. Scala, 1994. Amazon Coastal Squall Lines. Part I: Structure and Dynamics. *Mon. Wea. Rev.,* **122**, 608-622.

Gilford, M. T., R. C. Bonam, D. L. Martens, G. Myles, and M. J. Vojtesak, 1992: *South America South of the Amazon River – A Climatological Study*, USAFETAC/TN-92/004, USAF Environmental Technical Applications Center.

Glossary of Meteorology, 2000: T. S. Glickman, Ed., American Meteorological Society, 855 pp.

Houze, J. R., Jr., 1977: Structure and Dynamics of a Tropical Squall-Line System. *Mon. Wea. Rev.,* **105**, 1540-1567.

Kendrew, W. G., 1942: *The Climates of the Continents*. Oxford University, 473 pp.

Lenters, J. D., and K. H. Cook, 1999: Summertime Precipitation Variability over South America: Role of the Large-Scale Circulation. *Mon. Wea. Rev.,* **127**, 409-431.

Maddox, R. A., 1980: Mesoscale Convective Complexes. *Bull. Amer. Meteor. Soc.,* **61**, 1374-1387.

_____, D. L. Bartels, K. W. Howard and D. M. Rodgers, 1986: Mesoscale Convective Complexes in the Middle Latitudes. *Mesoscale Meteorology and Forecasting*, P. S. Ray, Ed., American Meteorological Society, 390-413.

Maps.com, cited 2002: Political Map of South America. [Available online at www.maps.com]

National Aeronautical and Space Administration (NASA), Goddard Space Flight Center, cited 2002: Data from NOAA GOES. [Available online at http://rsd.gsfc.nasa.gov/goes]

National Center for Atmospheric Research (NCAR), 1995-1996. NCEP Global Tropospheric Analyses. [Available from NCAR-UCAR, Data Support Section, 1850 Table Mesa Drive, Boulder, CO 80305]

National Climatic Data Center (NCDC), cited 2002: Historical GOES Browser Server. [Available online at http://lwf.ncdc.noaa.gov/servlets/GoesBrowser]

National Geophysical Data Center (NGDC), cited 2002: Space Physics Interactive Data Resource (SPIDR). [Available online at http://www.ngdc.noaa.gov/stp]

Nogues-Paegle, J, E. H. Berbery, W. C. Chao, T-C, Chen, K. Cook, A. F. Diaz, D. Enfield, R. Ferreira, R. Fu, A. M. Grimm, V. Kousky, B. Liebmann, J. Marengo, C. R. Mechoso, K. Mo, J. D. Neelin, J. Paegle, A. W. Robertson, A. Seth, C. S. Vera, and J. Zhou, cited 2002: Progress in the Pan American CLIVAR research: Understanding the South American Monsoon, 52 pp. [Available online at http://www.met.utah.edu/jnpaegle/bams/sams_meteorologica.html]

Ramage, C. S., 1995: *Forecasters Guide to Tropical Meteorology AWS TR 240 Updated*, AWS/TR-95/001, Air Weather Service.

Saulo, A. C., S. C. Chou, and M. Nicolini, 2000: Model Characterization of the South American Low-Level Flow during the 1997-1998 Spring-Summer Season. *Climate Dynamics,* **16**, 867-881.

Schwerdtfeger, Werner, Ed., 1976: *Climates of Central and South America*. Vol. 12, *World Survey Of Climatology,* Elsevier Scientific.

Shih, C. F.: National Center for Atmospheric Research, Data Support Section, Boulder, CO. Personal Correspondence. 8 Nov 2002.

Snyder, J. P., 1987: *Map Projections – A Working Manual,* US Geological Survey Professional Paper 1395, 383 pp.

25th Operational Weather Squadron (OWS), US Southern Command (SOUTHCOM), 2001-2002. Observation Data. [Available from 25 OWS/WXO, 3880 S. Phoenix St., Davis-Monthan AFB, AZ 85707]

Velasco, I., and J. M. Fritsch, 1987: Mesoscale Convective Complexes in the Americas. *J. Geophys. Res.,* **92**, 9591-9613.

Virgi, H., 1981: A Preliminary Study of Summertime Tropospheric Circulation Patterns over South America Estimated from Cloud Winds. *Mon. Wea. Rev.,* **109**, 599-610.

Walters, K. R., A. G. Korik, and M. J. Vojtesak, 1989: *The Caribbean Basin – A Climatological Study*, USAFETAC/TN-89/003, USAF Environmental Technical Applications Center.

Zipprich, T. E.: NCOIC Weather Systems Support, 25th OWS/WXX, Davis-Monthan AFB, AZ. Personal Correspondence. 9 Sep 2002.

Vita

Captain Marc R. Gasbarro hails from Medford, Massachusetts. After graduating from Arlington Catholic High School in 1991, he attended Lyndon State College, Vermont where he graduated with a B.S. in Meteorology in 1995. After working for Hewlett-Packard for several years, he received an appointment to the U.S. Air Force Officer Training School, where he was commissioned in September 1998.

Capt Gasbarro's first duty assignment was to the 75th Operational Support Squadron at Hill AFB, Utah. There he performed Wing Weather Officer and shift forecaster duties. During the spring of 2001, he deployed to Prince Sultan AB, Kingdom of Saudi Arabia, where he served as the 363rd Expeditionary Wing's Weather Officer. Capt Gasbarro entered the Graduate School of Engineering and Management, Air Force Institute of Technology, in August 2001. Upon graduation, he will be assigned to either the Western CONUS or SOUTHCOM weather cells both located at Davis-Monthan AFB, Arizona.

REPORT DOCUMENTATION PAGE

Form Approved
OMB No. 074-0188

1. REPORT DATE *(DD-MM-YYYY)*	2. REPORT TYPE	3. DATES COVERED *(From – To)*
18-02-2003	Master's Thesis	Jun 2002 – Mar 2003

4. TITLE AND SUBTITLE

FORECASTING EXCESSIVE RAINFALL AND LOW-CLOUD BASES EAST OF THE NORTHERN ANDES AND MESOSCALE CONVECTIVE COMPLEX MOVEMENT IN CENTRAL SOUTH AMERICA

5a. CONTRACT NUMBER

5b. GRANT NUMBER

5c. PROGRAM ELEMENT NUMBER

6. AUTHOR(S)

Gasbarro, Marc R., Captain, USAF

5d. PROJECT NUMBER

5e. TASK NUMBER

5f. WORK UNIT NUMBER

7. PERFORMING ORGANIZATION NAMES(S) AND ADDRESS(S)
Air Force Institute of Technology
Graduate School of Engineering and Management (AFIT/ENP)
2950 P Street, Building 640
WPAFB OH 45433-7765

8. PERFORMING ORGANIZATION REPORT NUMBER

AFIT/GM/ENP/03-03

9. SPONSORING/MONITORING AGENCY NAME(S) AND ADDRESS(ES)
25 OWS/WXO
Maj Jonathan Kelly
3880 S. Phoenix St.
Davis-Monthan AFB, AZ 85707

10. SPONSOR/MONITOR'S ACRONYM(S)

11. SPONSOR/MONITOR'S REPORT NUMBER(S)

12. DISTRIBUTION/AVAILABILITY STATEMENT

APPROVED FOR PUBLIC RELEASE; DISTRIBUTION UNLIMITED

13. SUPPLEMENTARY NOTES

14. ABSTRACT

This research produced better forecast tools for SOUTHCOM's 25th Operational Weather Squadron (OWS) over multiple areas of operation in South America. Heavy rainfall and low-cloud base events along the northeastern Andes foothills were examined, as well as, mesoscale convective complexes (MCCs) in Central South America (CSA). Low clouds, fog, and flooding rains hamper daily Department of Defense (DoD) counter-drug operations in Northwestern South America (NWSA). In addition, fierce MCCs interfere with joint-military exercises in CSA.

Climatological relationships of heavy rain with low clouds and fog in NWSA, relationships of excessive rainfall with upper-level divergence, low-level convergence, and vertical velocity in NWSA, and verification of Corfidi's method (Corfidi et al. 1996) of MCC movement for CSA were investigated. Ceilings and visibilities associated with low clouds and fog lower much more frequently following heavy rainfall in NWSA. In addition, findings proved that specific ceiling heights and visibilities relate to certain precipitation intensities. Findings indicated certain synoptic and meso-alpha scale features and specific minimum thresholds of upper-level divergence, low-level convergence, and vertical velocities are shown necessary to produce excessive rainfall events. Finally, Corfidi's method of forecasting MCC movement for North America was verified for applicability over CSA. Both propagation and advective cloud component vectors were examined for forecast use.

15. SUBJECT TERMS
Analysis and Forecasting, Climatology, Operations, Prediction, Severe Weather

16. SECURITY CLASSIFICATION OF:			17. LIMITATION OF ABSTRACT	18. NUMBER OF PAGES	19a. NAME OF RESPONSIBLE PERSON
a. REPORT	b. ABSTRACT	c. THIS PAGE			Ronald P. Lowther, Lt. Col, USAF
U	U	U	UU	163	19b. TELEPHONE NUMBER *(Include area code)* (937) 255-3636, ext 4546